Modeling Dust and Starlight in Galaxies Observed by *Spitzer* and *Herschel*: The KINGFISH Sample

G. Aniano[1,2] , B. T. Draine[1] , L. K. Hunt[3] , K. Sandstrom[4] , D. Calzetti[5] , R. C. Kennicutt[6,7] , D. A. Dale[8] ,
M. Galametz[9] , K. D. Gordon[10] , A. K. Leroy[11] , J.-D. T. Smith[12] , H. Roussel[13] , M. Sauvage[9] , F. Walter[14] ,
L. Armus[15] , A. D. Bolatto[16] , M. Boquien[17] , A. Crocker[18] , I. De Looze[19,20] , J. Donovan Meyer[21] , G. Helou[15] ,
J. Hinz[6] , B. D. Johnson[22] , J. Koda[23] , A. Miller[8,24] , E. Montiel[25,26] , E. J. Murphy[27] , M. Relaño[28,29] , H.-W. Rix[14] ,
E. Schinnerer[14] , R. Skibba[4,30] , M. G. Wolfire[16] , and C. W. Engelbracht[6,31]

[1] Dept. of Astrophysical Sciences, Peyton Hall, Princeton University, Princeton, NJ 08544, USA; draine@astro.princeton.edu
[2] LinkedIn Corporation, 700 E Middlefield Road, Mountain View, CA 94043, USA
[3] INAF—Osservatorio Astrofisico di Arcetri, Largo E. Fermi 5, I-50125 Firenze, Italy
[4] Center for Astrophysics and Space Sciences, University of California, 9500 Gilman Drive, San Diego, CA 92093, USA
[5] Dept. of Astronomy, University of Massachusetts, Amherst, MA 01003, USA
[6] Steward Observatory, University of Arizona, Tucson, AZ 85721-0065, USA
[7] Dept. of Physics & Astronomy, Texas A&M University, College Station, TX 77843-4242, USA
[8] Physics & Astronomy Dept., University of Wyoming, Laramie, WY 82071, USA
[9] AIM, CEA, CNRS, Université Paris-Saclay, Université Paris Diderot, Université Paris Cité, F-91191 Gif-sur-Yvette, France
[10] Space Telescope Science Institute, 3700 San Martin Drive, Baltimore, MD 21218, USA
[11] Ohio State University, Columbus, OH 43210, USA
[12] Dept. of Physics & Astronomy, University of Toledo, Toledo, OH 43606, USA
[13] Institut d'Astrophysique de Paris, Université Pierre et Marie Curie (UPMC), Sorbonne Université, CNRS, 75014 Paris, France
[14] Max-Planck-Institut fur Astronomie, Konigstuhl 17, D-69117 Heidelberg, Germany
[15] Spitzer Science Center, California Institute of Technology, MC 314-6, Pasadena, CA 91125, USA
[16] Dept. of Astronomy, University of Maryland, College Park, MD 20742, USA
[17] Centro de Astronomía (CITEVA), Universidad de Antofagasta, Avenida Angamos 601, Antofagasta, Chile
[18] Dept. of Physics, Reed College, Portland, OR 97202, USA
[19] Sterrenkundig Observatorium, Ghent University, Krijgslaan 281 S9, B-9000 Gent, Belgium
[20] Department of Physics & Astronomy, University College London, Gower Street, London WC1E6BT, UK
[21] National Radio Astronomy Observatory, Charlottesville, VA 22903, USA
[22] Harvard-Smithsonian Center for Astrophysics, Cambridge, MA 02138, USA
[23] Department of Physics and Astronomy, SUNY Stony Brook, Stony Brook, NY 11794-3800, USA
[24] Dept. of Physics, Montana State University, Bozeman, MT 59717, USA
[25] University of California, Davis, Davis CA 95616, USA
[26] SOFIA Science Center, NASA Ames Research Center, Moffett Field, CA 94036, USA
[27] National Radio Astronomy Observatory, Charlottesville, VA 22903, USA
[28] Dept. Física Teórica y del Cosmos, Universidad de Granada, Granada, Spain
[29] Instituto Universitario Carlos I de Física Teórica y Computacional, Universidad de Granada, E-18071, Granada, Spain
[30] Freelance science journalist, San Diego CA, USA

Abstract

Interstellar dust and starlight are modeled for the galaxies of the project "Key Insights on Nearby Galaxies: A Far-Infrared Survey with *Herschel*." The galaxies were observed by the Infrared Array Camera and the Multiband Imaging Photometer for *Spitzer* on *Spitzer Space Telescope*, and the Photodetector Array Camera and Spectrometer and the Spectral and Photometric Imaging Receiver on *Herschel Space Observatory*. With data from 3.6 to 500 μm, dust models are strongly constrained. Using a physical dust model, for each pixel in each galaxy we estimate (1) dust surface density, (2) dust mass fraction in polycyclic aromatic hydrocarbons (PAHs), (3) distribution of starlight intensities heating the dust, (4) total infrared (IR) luminosity emitted by the dust, and (5) IR luminosity originating in subregions with high starlight intensity. The dust models successfully reproduce the observed global and resolved spectral energy distributions. With the angular resolution of *Herschel*, we obtain well-resolved maps (available online) for the dust properties. As in previous studies, we find the PAH fraction q_{PAH} to be an increasing function of metallicity, with a threshold oxygen abundance $Z/Z_\odot \approx 0.1$, but we find the data to be fitted best with q_{PAH} increasing linearly with $\log(O/H)$ above a threshold value of $0.15(O/H)_\odot$. We obtain total dust masses for each galaxy by summing the dust mass over the individual map pixels; these "resolved" dust masses are consistent with the masses inferred from a model fit to the global photometry. The global dust-to-gas ratios obtained from this study are found to correlate with galaxy metallicities. Systems with $Z/Z_\odot \gtrsim 0.5$ have most of their refractory elements locked up in dust, whereas in systems with $Z/Z_\odot \lesssim 0.3$ most of these elements tend to remain in the gas phase. Within galaxies, we find that q_{PAH} is suppressed in regions with unusually warm dust with $\nu L_\nu(70\ \mu m) \gtrsim 0.4 L_{dust}$. With knowledge of one long-wavelength flux density ratio (e.g., f_{160}/f_{500}), the minimum starlight intensity heating the dust (U_{min}) can be estimated to within ∼50%, despite a variation in U_{min} of more than two orders of magnitude. For the adopted dust model, dust masses can be estimated to within ∼0.2 dex accuracy using the f_{160}/f_{500} flux ratio and the integrated dust luminosity, and to ∼0.07 dex accuracy using the 500 μm luminosity $\nu L_\nu(500\ \mu m)$ alone. There are additional systematic errors arising from the choice of dust

---
[31] Deceased.

1

model, but these are hard to estimate. These calibrated prescriptions for estimating starlight heating intensity and dust mass may be useful for studies of high-redshift galaxies.

Unified Astronomy Thesaurus concepts: Astrophysical dust processes (99); Polycyclic aromatic hydrocarbons (1280); Interstellar medium (847); Infrared galaxies (790)

Supporting material: figure sets

1. Introduction

Interstellar dust affects the appearance of galaxies by attenuating short-wavelength radiation from stars and ionized gas and contributing infrared (IR), submillimeter, millimeter, and microwave emission. Dust is also an important agent in the fluid dynamics, chemistry, heating, cooling, and even ionization balance in some interstellar regions, with a major role in the process of star formation. Despite the importance of dust, determination of the physical properties of interstellar dust grains has been a challenging task (for a review, see Draine 2003). Even the overall amount of dust present in other galaxies has often been very uncertain.

The "Key Insights on Nearby Galaxies: A Far-Infrared Survey with *Herschel*" (KINGFISH; Kennicutt et al. 2011) project is an imaging and spectroscopic survey of 61 nearby (distance $D < 30$ Mpc) galaxies with the *Herschel Space Observatory*. The KINGFISH galaxy sample was chosen to cover a wide range of integrated properties and local interstellar medium (ISM) environments found in the nearby universe. KINGFISH is a direct descendant of the "*Spitzer* Infrared Nearby Galaxies Survey" (SINGS; Kennicutt et al. 2003), which produced complete *Spitzer* imaging with the Infrared Array Camera (IRAC; Fazio et al. 2004) and the Multiband Imaging Photometer for *Spitzer* (MIPS; Rieke et al. 2004) instruments on *Spitzer Space Telescope* (Werner et al. 2004). The new *Herschel* observations include a complete mapping of the galaxies with the Photodetector Array Camera and Spectrometer (PACS; Poglitsch et al. 2010) and the Spectral and Photometric Imaging Receiver (SPIRE; Griffin et al. 2010) instruments. The merged KINGFISH and SINGS data set provides panchromatic mapping of the galaxies, across a wide range of local extragalactic ISM environments. In addition, we have KINGFISH and SINGS data for nine additional galaxies that fell within the 61 KINGFISH target fields. The photometric maps cover wavelengths from 3.6 to 500 μm, allowing us to produce well-resolved maps of the dust in nearby galaxies.

Skibba et al. (2011) modeled the dust in the KINGFISH galaxy sample using "modified blackbody" models. In the present work, we employ a physically motivated dust model based on a mixture of amorphous silicate grains and carbonaceous grains, each with a distribution of grain sizes (Draine & Li 2007, hereafter DL07). The dust grains are heated by starlight, and the model allows for a distribution of intensities for the starlight heating the dust. With a small number of adjustable parameters, the DL07 model reproduces the observed spectral energy distribution (SED) of the dust emission for a variety of astrophysical systems, giving some confidence in the reliability of dust masses estimated using the model. The DL07 model has been found to be consistent with the 3.6–500 μm emission from dust in the star-forming galaxies NGC 628 and NGC 6946 (Aniano et al. 2012), dust across M31 (Draine et al. 2014), emission from annular rings in the KINGFISH galaxy sample (Hunt et al. 2015), and overall dust SEDs from KINGFISH galaxies (Dale et al. 2017).

The present work is a sequel to the KINGFISH study of NGC 628 and NGC 6946 (Aniano et al. 2012, hereafter AD12). AD12 developed the image processing and dust modeling techniques employed here, using the spiral galaxies NGC 628 and NGC 6946 as examples. The present work takes into account a recent "recalibration" of the DL07 model made possible by *Planck* observations of diffuse Galactic emission (Planck Collaboration et al. 2016). We expand the spatially resolved dust modeling to the full KINGFISH galaxy sample, producing maps of dust mass surface density, polycyclic aromatic hydrocarbon (PAH) fraction, and intensities of the starlight heating the dust. Dependences of dust/gas ratio and PAH abundance on galaxy metallicity are examined, and resolved trends within galaxies are studied. While the present results are undoubtedly model-dependent, comparison of different dust models is beyond the scope of the present work.

The paper is organized as follows. A brief overview of the KINGFISH sample is given in Section 2, and in Section 3 we discuss the data sources. Background subtraction and data processing are described in Section 4, and the dust model is summarized in Section 5, including the *Planck*-based dust mass "recalibration" (Section 5.2). Results are reported in Section 6 with a comparison of dust parameter estimates based on different dust modeling strategies given in Section 6.4; global trends with metallicity are described in Sections 6.5 and 6.6; and resolved trends of DL07 fitted parameters are discussed in Section 6.7. We summarize the main results in Section 7. Appendix A (online version) displays maps of selected dust parameters for each of the 62 galaxies where we have reliable dust detections, at both MIPS160 and SPIRE250 resolution. Appendix B describes the method used to obtain upper limits for the dust mass for the eight galaxies (five dwarfs, three ellipticals) where we were unable to measure the dust mass reliably. The online data set with the KINGFISH data and dust models is described in Appendix C. In Appendix D we examine the robustness of the results as the point-spread function (PSF) is reduced, precluding use of the lower-resolution cameras (e.g., MIPS160 and SPIRE500).

2. Galaxy Sample

The observational program was designed to cover the 61 galaxies in the KINGFISH galaxy sample. Because we will also be discussing the nine extra galaxies and the statistical properties of various subsamples, we list these for clarity in Table 1. For each galaxy, we list in Table 2 the type, adopted distance, and major and minor optical radii (corresponding to $\sim$25th mag arcsec^{-2} isophotes), all taken from Kennicutt et al. (2011, Table 1).

The galaxies IC 3583, NGC 586, NGC 1317, NGC 1481, NGC 1510, NGC 3187, NGC 4533, NGC 7335, and NGC 7337 were not part of the KINGFISH sample, but were observed because each happened to be in the field of view of a

Table 1
Subsamples

Sample	Name	KF Galaxies	Extra Galaxies	Total
Full sample	KF70	61	9	70
Dust detected	KF62	53	9	62
H I detected	KF57	57	0	57
CO detected	⋯	35	0	35
CO upper limits	⋯	5	0	5

KINGFISH galaxy. For these galaxies, we have our standard imaging with PACS and SPIRE, as well as prior observations with IRAC and MIPS, so we are able to measure and model their SEDs with the same techniques as the KINGFISH galaxies. Information for these nine "extra" galaxies is appended to many of the tables below.

2.1. Metallicities

Table 2 also lists the oxygen abundance $12 + \log_{10}(O/H)$ for the galaxies in our sample. These are "characteristic" abundances, which Moustakas et al. (2010) take to be the values at galactocentric radius $R = 0.4R_{25}$. For six of the KINGFISH galaxies (DDO 154, IC 342, NGC 628, NGC 2146, NGC 3077, and NGC 5457), we use metallicities based on observations of weak lines (specifically, [N II]5726 and [O III]4364) that allow "direct" determination of the electron temperature in the H II regions responsible for the line emission (Storchi-Bergmann et al. 1994; van Zee et al. 1997; Pilyugin et al. 2007; Engelbracht et al. 2008; Li et al. 2013; Croxall et al. 2016). For these galaxies, we list the preferred weak-line metallicities in the PP04N2 column.

For the remaining 55 KINGFISH galaxies, we consider two popular "strong line" estimators: the "PT" or Pilyugin & Thuan (2005) method, taken from Moustakas et al. (2010), and the "PP04N2" method, based on [NII]/Hα (Pettini & Pagel 2004). Abundance measurements by Moustakas et al. (2010, "characteristic" values from their Table 8) with the "KK04" (Kobulnicky & Kewley 2004) calibration were converted to PP04N2 values, according to the parameters recommended by Kewley & Ellison (2008). This procedure is described in detail by Hunt et al. (2016), who use the same metallicities in their analysis; they preferred the PP04N2 calibration because it shows tighter scaling relations overall than other calibrations, and because its behavior in the mass–metallicity relation is quite similar to weak-line electron temperature determinations (e.g., Andrews & Martini 2013).

For NGC 1316, NGC 2841, and NGC 5055, the original KK04 O/H values ($\sim$9.4) from Moustakas et al. (2010) exceeded the range of applicability for the transformations formulated by Kewley & Ellison (2008). Thus we have (somewhat arbitrarily) given these three galaxies a maximum metallicity of $12 + \log_{10}(O/H) = 9.0$, consistent with what is advocated by Pilyugin et al. (2007). Ultimately, the metallicities for these three galaxies are uncertain, but toward the high end of the observed range.

Figure 1 compares the PT and PP04N2 metallicity estimates for the 55 KINGFISH galaxies where "direct" method estimates are unavailable. Note that the PT and PP04N2 metallicities differ by as much as 0.5 dex (e.g., DDO 154, type IBm) or even 0.63 dex (e.g., NGC 1482, type SA0). It is evident that the metallicity estimates have significant uncertainties, and that there are systematic differences between the

two methods (see also Kewley & Ellison 2008). Below we will argue, by comparing PAH abundances estimated from infrared observations with these two metallicity estimates, that the PP04N2 estimate appears to be more reliable, at least for the galaxies in the KINGFISH sample.

3. Observations and Data Reduction

3.1. Infrared, Far-infrared, and Submillimeter

Most of the galaxies in the KINGFISH sample are part of the SINGS galaxy sample and were imaged by *Spitzer Space Telescope* as part of the SINGS observing program (Kennicutt et al. 2003). IRAC and MIPS imaging obtained by other *Spitzer Space Telescope* observing programs was available for the remaining KINGFISH galaxies.

The KINGFISH project imaged the galaxies with the *Herschel Space Observatory* (Pilbratt et al. 2010), following the observing strategy described by Kennicutt et al. (2011), using the 70, 100, and 160 μm PACS filters and the 250, 350, and 500 μm SPIRE filters. The maps were designed to cover a region out to $\gtrsim$1.5 times the optical radius R_{25}, with good signal-to-noise ratio (S/N) and redundancy.

Following AD12, we will use "camera" to identify each optical configuration of the observing instruments; that is, each different channel or filter arrangement of the instruments will be referred to as a different "camera." With this nomenclature, each "camera" has a characteristic spectral response and PSF. We will refer to the IRAC, MIPS, PACS, and SPIRE cameras using their nominal wavelengths in microns: IRAC3.6, IRAC4.5, IRAC5.8, IRAC8.0, MIPS24, MIPS70, MIPS160, PACS70, PACS100, PACS160, SPIRE250, SPIRE350, and SPIRE500.

IRAC imaged the galaxies in four bands, centered at 3.6, 4.5, 5.8, and 8.0 μm, as described by Kennicutt et al. (2003). The images were processed by the SINGS Fifth Data Delivery pipeline.[32] The IRAC images are calibrated for point sources. Photometry of extended sources requires so-called "aperture corrections." We multiply the intensities in each pixel by the asymptotic (infinite radii) value of the aperture correction (i.e., the aperture correction corresponding to an infinite radius aperture). We use the factors 0.91, 0.94, 0.66, and 0.74 for the 3.6 μm, 4.5 μm, 5.8 μm, and 8.0 μm bands, respectively, as described in the IRAC Instrument Handbook (V2.0.1).[33]

Imaging with MIPS at 24, 70, and 160 μm was carried out following the observing strategy described in Kennicutt et al. (2003). The data were reduced using the Local Volume Legacy (LVL) project pipeline.[34] A correction for nonlinearities in the MIPS70 camera was applied, as described by Dale et al. (2009) and Gordon et al. (2011).

The galaxies were observed with the PACS and SPIRE instruments on *Herschel*, using the "Scan Map" observing mode. Both PACS and SPIRE images were first reduced to "level 1" (flux-calibrated brightness time series, with attached sky coordinates) using HIPE v11.1.0 (Ott 2010), and maps ("level 2") were created using the Scanamorphos data reduction pipeline (Roussel 2013), v24.0. This reduction strategy used

---

[32] Details can be found in the data release documentation: https://irsa.ipac.caltech.edu/data/SPITZER/SINGS/doc/sings_fifth_delivery_v2.pdf.
[33] http://irsa.ipac.caltech.edu/data/SPITZER/docs/irac/iracinstrumenthandbook/IRAC_Instrument_Handbook.pdf
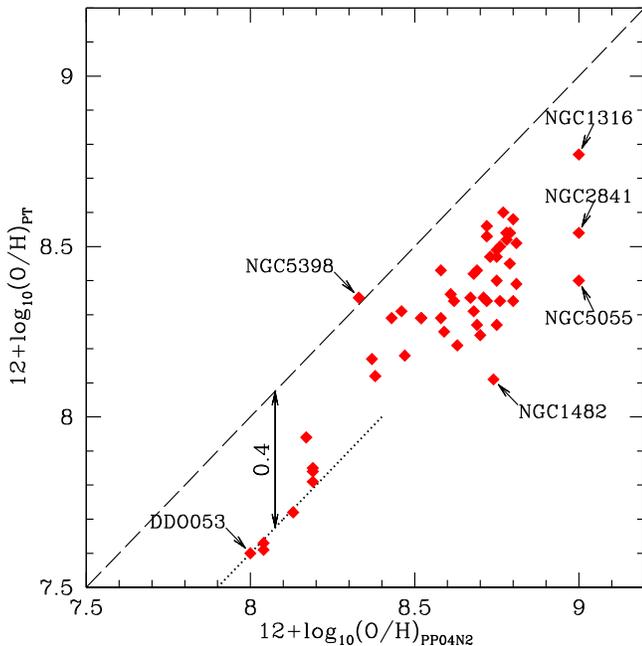[34] Details can be found in the data release documentation: https://irsa.ipac.caltech.edu/data/SPITZER/LVL/LVL_DR5_v5.pdf.

Table 2
Sixty-one KINGFISH Galaxies and Nine Extra Galaxies

Galaxy	Type	$12 + \log_{10}(O/H)$ PT[a]	$12 + \log_{10}(O/H)$ PP04N2[b]	D (Mpc)	Optical R_{maj} (kpc)	Optical R_{min} (kpc)	Optical Ω (arcmin²)	M160 Mask $\Sigma_{Ld,min}$ ($L_\odot$ pc⁻²)	M160 Mask Ω (arcmin²)	S250 Mask Ω (arcmin²)
DDO 053	Im	7.60 ± 0.11	8.00[c]	3.61	0.81	0.70	1.61	...	...	...
DDO 154	IBm	7.54 ± 0.09	7.67[c]	4.30	1.89	1.36	5.15	...	...	...
DDO 165	Im	7.63 ± 0.08	8.04[c]	4.57	2.30	1.22	4.98	...	...	...
Hol1	IABm	7.61 ± 0.11	8.04[c]	3.90	2.06	2.06	10.4	...	...	...
Hol2	Im	7.72 ± 0.14	8.13	3.05	3.52	2.78	39.0	0.72	25.2	23.0
IC 342	SABcd	8.70 ± 0.20[d]	8.85[e]	3.28	10.5	9.18	332.	3.47	417.	398.
IC 2574	SABm	7.85 ± 0.14	8.19	3.79	7.27	2.72	51.1	0.66	54.5	52.7
M81dwB	Im	7.84 ± 0.13	8.19[c]	3.60	0.46	0.30	0.40	...	...	...
NGC 0337	SBd	8.18 ± 0.07	8.47	19.30	8.08	4.98	4.01	3.55	11.1	6.77
NGC 0584	E4	8.43 ± 0.20	8.69[c]	20.80	12.6	6.67	7.20	...	...	...
NGC 0628	SAc	8.35 ± 0.01	8.64[f]	7.20	11.0	10.0	78.8	1.70	76.1	70.3
NGC 0855	E	8.29 ± 0.10	8.43[c]	9.73	2.83	2.79	3.09	...	...	...
NGC 0925	SABd	8.25 ± 0.01	8.59	9.12	13.9	7.57	47.0	1.48	46.3	44.8
NGC 1097	SBb	8.47 ± 0.02	8.75	14.20	19.3	12.9	45.8	2.19	66.3	55.7
NGC 1266	SB0	8.29 ± 0.20	8.52	30.60	6.85	6.75	1.83	2.63	9.09	8.37
NGC 1291	SB0/a	8.52 ± 0.20	8.78	10.40	14.8	14.8	75.1	0.65	123.	119.
NGC 1316	SAB0	8.77 ± 0.20	9.00[g]	21.00	12.2	8.49	8.73	1.02	17.5	14.2
NGC 1377	S0	8.29 ± 0.20	8.52	24.60	6.37	6.37	2.49	2.57	7.20	8.46
NGC 1404	E1	8.54 ± 0.20	8.78[c]	20.20	9.75	8.69	7.71	...	...	...
NGC 1482	SA0	8.11 ± 0.13	8.74	22.60	8.09	4.40	2.59	2.19	24.4	13.0
NGC 1512	SBab	8.56 ± 0.12	8.72	11.60	15.0	9.27	38.5	0.89	34.4	15.4
NGC 2146	Sbab	8.68 ± 0.10[e]	8.68[e]	17.20	16.8	7.35	15.5	4.8	39.2	18.5
NGC 2798	SBa	8.34 ± 0.08	8.72	25.80	9.61	9.61	5.15	2.63	13.0	10.2
NGC 2841	SAb	8.54 ± 0.03	9.00[g]	14.10	16.7	6.77	21.1	0.66	60.9	55.1
NGC 2915	I0	7.94 ± 0.13	8.17	3.78	1.04	0.51	1.37	0.58	5.58	5.51
NGC 2976	SAc	8.36 ± 0.06	8.61	3.55	3.04	1.28	11.5	2.57	25.6	21.3
NGC 3049	SBab	8.53 ± 0.01	8.72	19.20	6.09	3.99	2.45	1.48	7.92	7.99
NGC 3077	I0pec	...	8.64[h]	3.83	3.34	3.29	27.8	2.14	39.2	32.6
NGC 3184	SABcd	8.51 ± 0.01	8.81	11.70	12.6	11.8	40.4	0.85	64.0	60.5
NGC 3190	SAap	8.49 ± 0.20	8.75	19.30	12.2	3.78	4.61	1.17	12.3	11.2
NGC 3198	SBc	8.34 ± 0.02	8.76	14.10	17.5	5.98	19.5	1.23	36.9	30.0
NGC 3265	E	8.27 ± 0.14	8.69	19.60	3.65	2.80	0.99	2.04	6.39	6.10
NGC 3351	SBb	8.60 ± 0.01	8.77	9.33	10.1	6.74	28.9	1.35	49.1	43.3
NGC 3521	SABbc	8.39 ± 0.02	8.81	11.20	17.9	7.83	41.4	2.19	91.4	76.6
NGC 3621	SAd	8.27 ± 0.02	8.75	6.55	11.7	6.55	66.4	1.07	103.	85.7
NGC 3627	SABb	8.34 ± 0.24	8.62	9.38	12.4	5.26	27.6	2.00	87.2	54.9
NGC 3773	SA0	8.43 ± 0.03	8.58	12.40	2.13	1.80	0.93	1.86	5.85	5.81
NGC 3938	SAc	8.42 ± 0.20	8.68	17.90	14.0	12.8	20.8	1.15	39.4	34.5
NGC 4236	SBdm	8.17 ± 0.20	8.37	4.45	10.4	2.85	55.4	0.71	64.7	63.2
NGC 4254	SAc	8.45 ± 0.01	8.79	14.40	11.3	9.76	19.7	2.40	45.9	33.2
NGC 4321	SABbc	8.50 ± 0.03	8.76	14.30	15.4	13.1	36.7	1.66	60.6	40.4
NGC 4536	SABbc	8.21 ± 0.08	8.63	14.50	16.0	6.25	17.6	2.09	37.0	25.2
NGC 4559	SABcd	8.29 ± 0.01	8.58	6.98	10.9	4.08	33.8	1.17	43.2	40.3
NGC 4569	SABab	8.58 ± 0.20	8.80	9.86	11.5	4.85	21.2	1.95	18.3	17.2
NGC 4579	SABb	8.54 ± 0.20	8.79	16.40	14.0	11.1	21.4	2.24	22.4	18.0
NGC 4594	SAa	8.54 ± 0.20	8.79	9.08	11.5	2.98	15.5	1.55	31.1	27.8
NGC 4625	SABmp	8.35 ± 0.17	8.67	9.30	2.95	2.55	3.23	1.58	7.47	6.47
NGC 4631	SBd	8.12 ± 0.11	8.38	7.62	17.2	0.30	3.28	3.16	83.4	43.3
NGC 4725	SABab	8.35 ± 0.13	8.71	11.90	18.6	12.9	62.7	1.15	64.1	55.0
NGC 4736	SAab	8.31 ± 0.03	8.68	4.66	7.60	6.15	80.0	1.38	124.	120.
NGC 4826	SAab	8.54 ± 0.10	8.78	5.27	6.13	4.70	38.5	2.88	37.3	17.3
NGC 5055	SAbc	8.40 ± 0.03	9.00[g]	7.94	14.6	8.14	69.7	2.75	87.6	67.6
NGC 5398	SBdm	8.35 ± 0.05	8.33	7.66	3.14	1.85	3.67	1.62	7.29	5.72
NGC 5408	IBm	7.81 ± 0.09	8.19	4.80	1.13	0.53	0.97	2.95	6.66	5.42
NGC 5457	SABcd	8.46 ± 0.10[h]	8.38[i]	6.70	17.1	16.9	238.	0.74	398.	385.
NGC 5474	SAcd	8.31 ± 0.22	8.46	6.80	4.73	4.21	16.0	1.10	21.1	17.9
NGC 5713	SABbc	8.24 ± 0.06	8.70	21.40	8.59	7.65	5.33	1.51	35.6	14.3
NGC 5866	S0	8.47 ± 0.20	8.73	15.30	10.4	3.90	6.44	1.91	8.64	8.77
NGC 6946	SABcd	8.400 ± 0.030	8.75	6.80	11.4	9.63	87.8	7.08	102.	100.
NGC 7331	SAb	8.340 ± 0.020	8.80	14.50	22.1	6.83	26.7	3.02	47.1	32.3
NGC 7793	SAd	8.310 ± 0.020	8.64	3.91	5.31	3.55	45.8	1.35	76.2	58.9

Table 2
(Continued)

| Galaxy | Type | 12 + $\log_{10}$(O/H) | | D | Optical | | | M160 Mask | | S250 Mask |
		PT[a]	PP04N2[b]	(Mpc)	R_{maj} (kpc)	R_{min} (kpc)	Ω (arcmin^2)	$\Sigma_{Ld,min}$ ($L_\odot$ pc^{-2})	Ω (arcmin^2)	Ω (arcmin^2)
IC 3583	IBm	⋯	⋯	14.20	5.16	2.96	2.82	1.32	6.57	5.96
NGC 0586	SAa	⋯	⋯	20.80	5.63	1.92	0.93	0.78	5.31	4.93
NGC 1317	SABa	⋯	⋯	21.00	11.9	11.6	11.6	1.05	10.8	10.7
NGC 1481	SA0	⋯	⋯	22.60	3.68	2.90	0.78	0.98	5.40	2.00
NGC 1510	SA0	⋯	8.38[j]	11.60	2.80	2.15	1.66	0.95	7.74	1.76
NGC 3187	SBc	⋯	⋯	19.30	7.19	2.69	1.93	1.74	7.92	5.53
NGC 4533	SAd	⋯	⋯	14.50	5.48	0.38	0.37	1.12	6.12	3.83
NGC 7335	SAO	⋯	⋯	83.40	27.9	26.9	4.01	3.16	2.61	2.60
NGC 7337	SBb	⋯	⋯	87.20	25.1	21.7	2.67	2.00	2.16	1.98

Notes.
[a] From Moustakas et al. (2010) except as noted.
[b] Derived from KK metallicities from Moustakas et al. (2010) except as noted.
[c] van Zee et al. (1997).
[d] Pilyugin et al. (2006).
[e] Engelbracht et al. (2008).
[f] Berg et al. (2015).
[g] See text.
[h] Storchi-Bergmann et al. (1994).
[i] Li et al. (2013).
[j] Marble et al. (2010).

Figure 1. 12 + $\log_{10}$(O/H) for 55 KINGFISH galaxies using two different estimators (see text). The long-dashed line corresponds to the identity between the two quantities. The PT estimate for O/H is systematically below the PP04N2 estimate (by ∼0.4 dex at low O/H: dotted line), and there is considerable additional scatter between the two estimates.

the latest available PACS and SPIRE calibrations (as of 2014 July) and was designed to preserve the low-surface-brightness diffuse emission.

The assumed beam sizes are 465.4, 822.6, and 1769 arcsec^2 for SPIRE250, SPIRE350, and SPIRE500, respectively. Additionally, we excluded discrepant bolometers from the map and adjusted the pointing to match the MIPS24 map.

3.2. H I Observations

To measure the H I gas mass, we use H I 21 cm line observations made with the NSF's NRAO[35] Karl G. Jansky Very Large Array (VLA).

For 23 of our galaxies, we have data from The H I Nearby Galaxies Survey (THINGS; Walter et al. 2008), and for four galaxies we use data from the LittleTHINGS survey (Hunter et al. 2012). For 10 galaxies without THINGS or Little-THINGS observations, we obtained VLA 21 cm maps in programs AL731 and AL735, in some cases also incorporating archival VLA observations. For eight targets, we reduced and incorporated VLA archival observations of the 21 cm line. For one galaxy, NGC 4559, we use archival Westerbork Synthesis Radio Telescope observations. These observations are described in Leroy et al. (2013). For each galaxy, the source of the H I map is listed in Table 3. The dominant uncertainty on the measured H I masses comes from the calibration uncertainties of ∼10%.

For NGC 1266, Alatalo et al. (2011) estimated M(H I) = $9.5 \times 10^6 M_\odot$ based on 21 cm absorption of the radio continuum from the nucleus (for an assumed $T_{spin} = 100$ K). However, we estimate that H I 21 cm line emission from as much as $\sim 2 \times 10^9 M_\odot$ of H I could have gone undetected because of the strong continuum (0.1 Jy at 1.4 GHz), so the H I mass must be considered highly uncertain.

Thus we have H I data for 57 of the 61 KINGFISH galaxies. H I 21 cm observations were not available for NGC 1316 (SAB0), NGC 1377 (S0), NGC 1404 (E1), or NGC 5866 (S0), nor for the nine extra galaxies.

---

[35] The National Radio Astronomy Observatory is a facility of the National Science Foundation operated under cooperative agreement by Associated Universities, Inc.

Table 3
H I and CO Observation Summary

Galaxy	H I Source	CO Source
DDO 053	LittleTHINGS	...
DDO 154	THINGS	HERACLES
DDO 165	LittleTHINGS	...
Holmberg I	THINGS	HERACLES
Holmberg II	THINGS	HERACLES
IC 342	Hyperleda	...
IC 2574	THINGS	HERACLES
M81dwB	THINGS	HERACLES
NGC 0337	Archival	HERACLES
NGC 0584	Hyperleda	...
NGC 0628	THINGS	HERACLES
NGC 0855	Hyperleda	...
NGC 0925	THINGS	HERACLES
NGC 1097	Hyperleda	...
NGC 1266	ABY11	ABY11
NGC 1291	Hyperleda	...
NGC 1482	Hyperleda	...
NGC 1512	Hyperleda	...
NGC 2146	AL735	HERACLES
NGC 2798	AL735	HERACLES
NGC 2841	THINGS	HERACLES
NGC 2915	Hyperleda	...
NGC 2976	THINGS	HERACLES
NGC 3049	AL735	HERACLES
NGC 3077	THINGS	HERACLES
NGC 3184	THINGS	HERACLES
NGC 3190	AL735	MBLE12
NGC 3198	THINGS	HERACLES
NGC 3265	Hyperleda	...
NGC 3351	THINGS	HERACLES
NGC 3521	THINGS	HERACLES
NGC 3621	THINGS	...
NGC 3627	THINGS	HERACLES
NGC 3773	Hyperleda	...
NGC 3938	Archival, AL731	HERACLES
NGC 4236	AL731, AL735	HERACLES
NGC 4254	Archival, AL731	HERACLES
NGC 4321	Archival	HERACLES
NGC 4536	Archival, AL731, AL735	HERACLES
NGC 4559	Archival(WSRT)	HERACLES
NGC 4569	Archival	HERACLES
NGC 4579	Archival	HERACLES
NGC 4594	Archival, AL735	HERACLES
NGC 4625	Archival	HERACLES
NGC 4631	Archival	HERACLES
NGC 4725	AL735	HERACLES
NGC 4736	THINGS	HERACLES
NGC 4826	THINGS	CANON
NGC 5055	THINGS	HERACLES
NGC 5398	Hyperleda	...
NGC 5408	Hyperleda	...
NGC 5457	THINGS	HERACLES
NGC 5474	Archival	HERACLES
NGC 5713	Archival	HERACLES
NGC 6946	THINGS	HERACLES
NGC 7331	THINGS	HERACLES
NGC 7793	THINGS	...

Note. THINGS = Walter et al. ([2008](#)). HERACLES = Leroy et al. ([2009](#), [2013](#)). ABY11 = Alatalo et al. ([2011](#)). LittleTHINGS = Hunter et al. ([2012](#)). MBLE12 = Martinez-Badenes et al. ([2012](#)). Hyperleda = Makarov et al. ([2014](#)). CANON = Donovan Meyer et al. ([2013](#)).

3.3. CO Observations

To estimate H_2 masses, we use observations of CO line emission together with an assumed ratio of H_2 mass to CO luminosity. The adopted CO-to-H_2 "conversion factors" are discussed in Section [4.5](#).

For 38 KINGFISH galaxies, we use $^{12}CO\ J = 2–1$ maps from the the HERA CO Line Emission Survey (HERACLES; Leroy et al. [2009](#), [2013](#)).

For NGC 4826, we use $^{12}CO\ J = 1–0$ mapping from the Nobeyama Radio Observatory (J. Koda et al. 2019, in preparation). We propagate uncertainties on the CO integrated intensities from the spectra through the gridding and masking of the cube as described in Leroy et al. ([2013](#)).

For NGC 1266, we use $M(H_2) = 1.6 \times 10^9 M_\odot$ from Alatalo et al. ([2011](#)). We arbitrarily adopt a $\pm 50\%$ uncertainty. For NGC 3190, we use CO line fluxes from Martinez-Badenes et al. ([2012](#)).

Thus we have CO data for 41 of the 61 galaxies in the KINGFISH sample. CO observations are not available for any of the nine extra galaxies.

4. Image Analysis

4.1. Background Subtraction

All camera images are first rotated to RA/Dec coordinates and then trimmed to a common sky region. For each image, we estimate the best-fit "tilted plane" background (consisting of instrumental background, Galactic foreground emission, and cosmic infrared background emission) using an iterative procedure described in AD12. The procedure uses multiple cameras to identify regions in the image where only background emission is present. Regions where excess emission is detected at more than one wavelength are not used for background estimation.

4.2. Convolution to Common Resolution

After background subtraction, the images are convolved to a common PSF and resampled on a common final-map grid, with pixel sizes for each final-map PSF as given in Table [4](#). Finally, the dispersion in intensities of the background pixels (which includes noise coming from unresolved, undetected background sources) is used to estimate the pixel flux uncertainties. By comparing the MIPS and PACS images, we can also estimate a calibration uncertainty. The procedures used are fully described in AD12.

As discussed in AD12, multiwavelength observations must be degraded to a common PSF before dust models are fit to the observed intensities. The convolution to a common PSF is carried out using the methods described by Aniano et al. ([2011](#)). In the present work, we present, for each galaxy, resolved results at two final-map PSFs: SPIRE250 and MIPS160, henceforth abbreviated as S250 and M160. S250 is the PSF with the smallest FWHM that allows use of enough cameras to adequately constrain the dust SED (IRAC, MIPS24, PACS70, 100, 160, and SPIRE250). The M160 PSF allows inclusion of *all* the cameras (IRAC, MIPS, PACS, SPIRE), therefore producing the most reliable maps; this will be our "gold standard." Table [4](#) lists the resolutions of the cameras, the pixel size in the final-map grids used, and the other cameras

Table 4
Image Resolutions

Camera	FWHM[a] ($''$)	50% Power[a] Diameter ($''$)	Final Grid pixel[b] ($''$)	Compatible Cameras[c]
IRAC3.6	1.90	2.38	⋯	not used as a final-map PSF
IRAC4.5	1.81	2.48	⋯	not used as a final-map PSF
IRAC6	2.11	3.94	⋯	not used as a final-map PSF
IRAC8	2.82	4.42	⋯	not used as a final-map PSF
PACS70	5.67	8.46	⋯	not used as a final-map PSF
MIPS24	6.43	9.86	⋯	not used as a final-map PSF
PACS100	7.04	9.74	⋯	not used as a final-map PSF
PACS160	11.2	15.3	5.0	IRAC; MIPS24; PACS
SPIRE250 (S250)	18.2	20.4	6.0	IRAC; MIPS24; PACS; SPIRE250
MIPS70	18.7	28.8	10.0	IRAC; MIPS24,70; PACS; SPIRE250
SPIRE350	24.9	26.8	10.0	IRAC; MIPS24,70; PACS; SPIRE250,350
SPIRE500	36.1	39.0	15.0	IRAC; MIPS24,70; PACS; SPIRE
MIPS160 (M160)	38.8	58.0	18.0	IRAC; MIPS; PACS; SPIRE

Notes.
[a] Values from Aniano et al. (2011) for the circularized PSFs.
[b] The pixel size in the final-map grids is chosen to Nyquist-sample the PSFs.
[c] Other cameras that can be convolved into the camera PSF (see text for details).

that can be used at this resolution. In Appendix D we compare dust mass estimates obtained with different final-map PSFs.

4.3. Image Segmentation

After convolution to a common "final-map" PSF and background subtraction, we next fit a dust model to the observed SED of each pixel in the field. In order for dust mass estimation to be reliable, the pixel's SED must be measured in a number of bands with a reasonable S/N. However, estimates of the total dust infrared luminosity per unit area from a single pixel, Σ_{Ld}, are reliable so long as there is a significant detection of far-infrared emission after background subtraction.

The procedure used for automatically identifying "galaxy" pixels is described in Appendices A and B of AD12. For purposes of dust mass estimation, we need to limit the modeling to a "galaxy mask" consisting of pixels where the emission from the galaxy of interest has sufficiently high surface brightness for dust mass estimation (via SED fitting) to be reasonably reliable.

A simple criterion for "sufficiently high surface brightness" is that the total dust luminosity/projected area Σ_{Ld} exceed a specified threshold value, $\Sigma_{Ld,min}$. The value chosen for $\Sigma_{Ld,min}$ will depend on the noisiness of the data (which may depend on the brightness of the (subtracted) Galactic foreground emission, as well as on the presence of other extragalactic objects in the field, stars, or even small-scale structure in the Galactic foreground, which may compromise background estimation and subtraction). The choice of $\Sigma_{Ld,min}$ will also depend on the choice of final-map PSF: use of a larger PSF improves the S/N in each pixel by smoothing and also enables use of more cameras to constrain the dust modeling, and thus may allow use of a lower threshold $\Sigma_{Ld,min}$. In the present study, $\Sigma_{Ld,min}$ was chosen subjectively for each galaxy.

In this paper, we report results for two final-map PSFs, S250 and M160, with the PSF FWHM corresponding to linear scales FWHM = 0.88 kpc for S250 and 1.88 kpc for M160 at the median distance $D = 10$ Mpc of the KINGFISH galaxy sample. Table 2 lists $\Sigma_{Ld,min}$ used to define the galaxy masks for the M160 resolution studies, for the 62 galaxies where we detect dust emission. Our adopted values of $\Sigma_{Ld,min}$ vary from

galaxy to galaxy, ranging from values as low as 0.58 $L_\odot$ pc^{-2} (NGC 2915) to values as high as 7 $L_\odot$ pc^{-2} (NGC 6946). The median $\Sigma_{Ld,min}$ = 1.6 $L_\odot$ pc^{-2} (e.g., NGC 4625). For each galaxy where dust is reliably detected at M160 resolution, we also generate a S250-resolution mask, intended to comprise the region where the S250-resolution data permit reliable estimation of the dust surface density. Our S250 masks are often similar in size to the M160 mask, but for some galaxies the S250 mask is considerably smaller than the M160 mask; the most extreme example is NGC 1481, where the S250 mask area is only 37% of the M160 mask area. The M160 and S250 masks are shown in Figures 17.1–17.62. The solid angle of each mask is listed in Table 2. Because of the improved S/N in each pixel, most of the analysis in this paper will be done with the M160-resolution images and masks.

For five dwarf galaxies where dust detection is uncertain (DDO 053, DDO 154, DDO 165, Hol1, and M81dwB), we choose instead to use masks defined by H I observations. For three elliptical galaxies where dust detection is uncertain (NGC 0584, NGC 0855, and NGC 1404), we use $\Sigma_{Ld,min}$-based masks. We do not detect dust in any of these eight galaxies. See Appendix B for further details.

4.4. Integrated Fluxes

The *Spitzer* and *Herschel* band surface brightnesses are integrated over the M160- and S250-resolution galaxy masks to obtain integrated flux densities. The IRAC and MIPS flux densities are given in Table 5, and the PACS and SPIRE flux densities are given in Table 6. Note that MIPS70, MIPS160, SPIRE350, and SPIRE500 are not used at S250 resolution.

The uncertainties given in Tables 5 and 6 include uncertainties associated with background subtraction, as well as calibration uncertainties. As discussed in Section 5.3, the fluxes measured by PACS and MIPS sometimes differ by considerably more than the estimated uncertainties: we know that some of the uncertainties have been underestimated, although it is not clear how to improve on our estimates.

Dale et al. (2012, 2017) carried out careful foreground star and background galaxy removal tailored for globally integrated photometry. For 44 of the 53 KINGFISH galaxies where we

Table 5
Spitzer Photometry of KINGFISH Galaxies with Dust Detections

| Galaxy | Mask | IRAC F_ν (Jy) | | | | MIPS F_ν (Jy) | | |
		3.6 μm	4.5 μm	5.8 μm	8.0 μm	24 μm	70 μm	160 μm
Hol2	S250	0.090 ± 0.018	0.065 ± 0.014	0.041 ± 0.015	0.047 ± 0.013	0.187 ± 0.033	⋯	⋯
"	M160	0.097 ± 0.024	0.070 ± 0.019	0.042 ± 0.015	0.047 ± 0.014	0.178 ± 0.027	3.1 ± 1.4	3.3 ± 1.9
IC 342	S250	14.3 ± 2.3	8.6 ± 1.6	12.0 ± 3.6	30. ± 6.	36.2 ± 4.3	⋯	⋯
"	M160	14.3 ± 2.5	8.6 ± 1.5	12.0 ± 3.4	30. ± 6.	36.3 ± 4.1	338. ± 161.	913. ± 302.
IC 2574	S250	0.136 ± 0.028	0.101 ± 0.021	0.058 ± 0.023	0.061 ± 0.035	0.27 ± 0.06	⋯	⋯
"	M160	0.135 ± 0.035	0.100 ± 0.027	0.057 ± 0.021	0.059 ± 0.029	0.246 ± 0.044	4.8 ± 2.1	9.5 ± 5.0
NGC 0337	S250	0.092 ± 0.010	0.065 ± 0.006	0.139 ± 0.035	0.37 ± 0.07	0.76 ± 0.08	⋯	⋯
"	M160	0.092 ± 0.015	0.066 ± 0.008	0.137 ± 0.036	0.36 ± 0.07	0.72 ± 0.08	10.1 ± 3.1	16.5 ± 3.9
NGC 0628	S250	0.87 ± 0.10	0.60 ± 0.06	1.03 ± 0.25	2.7 ± 0.5	3.18 ± 0.38	⋯	⋯
"	M160	0.86 ± 0.11	0.59 ± 0.06	1.00 ± 0.24	2.67 ± 0.48	3.10 ± 0.34	32. ± 12.	106. ± 16.
NGC 0925	S250	0.330 ± 0.048	0.226 ± 0.044	0.29 ± 0.08	0.63 ± 0.12	0.85 ± 0.12	⋯	⋯
"	M160	0.33 ± 0.06	0.226 ± 0.048	0.28 ± 0.07	0.61 ± 0.12	0.82 ± 0.10	13.0 ± 3.8	37. ± 7.
NGC 1097	S250	1.19 ± 0.12	0.79 ± 0.07	1.22 ± 0.29	3.1 ± 0.5	6.5 ± 0.7	⋯	⋯
"	M160	1.17 ± 0.13	0.79 ± 0.08	1.19 ± 0.28	3.0 ± 0.5	6.4 ± 0.7	57. ± 26.	143. ± 34.
NGC 1266	S250	0.062 ± 0.007	0.048 ± 0.005	0.053 ± 0.014	0.099 ± 0.020	0.88 ± 0.09	⋯	⋯
"	M160	0.059 ± 0.008	0.046 ± 0.006	0.051 ± 0.013	0.095 ± 0.019	0.83 ± 0.09	11.5 ± 3.8	9.2 ± 4.1
NGC 1291	S250	1.99 ± 0.19	1.24 ± 0.12	0.84 ± 0.23	0.73 ± 0.14	0.53 ± 0.11	⋯	⋯
"	M160	1.97 ± 0.20	1.23 ± 0.13	0.82 ± 0.21	0.72 ± 0.14	0.51 ± 0.08	5.7 ± 9.6	25. ± 9.
NGC 1316	S250	1.55 ± 0.14	0.98 ± 0.08	0.65 ± 0.15	0.50 ± 0.09	0.353 ± 0.042	⋯	⋯
"	M160	1.47 ± 0.14	0.93 ± 0.08	0.62 ± 0.14	0.47 ± 0.09	0.334 ± 0.038	4.8 ± 1.3	9.6 ± 2.3
NGC 1377	S250	0.065 ± 0.007	0.092 ± 0.009	0.25 ± 0.06	0.43 ± 0.07	1.79 ± 0.19	⋯	⋯
"	M160	0.061 ± 0.008	0.087 ± 0.010	0.24 ± 0.05	0.41 ± 0.07	1.66 ± 0.17	6.0 ± 1.3	2.9 ± 1.0
NGC 1482	S250	0.380 ± 0.035	0.271 ± 0.022	0.63 ± 0.14	1.60 ± 0.27	2.33 ± 0.24	⋯	⋯
"	M160	0.372 ± 0.042	0.283 ± 0.029	0.60 ± 0.14	1.58 ± 0.27	2.07 ± 0.22	31. ± 12.	37. ± 10.
NGC 1512	S250	0.321 ± 0.030	0.207 ± 0.018	0.209 ± 0.049	0.39 ± 0.07	0.42 ± 0.05	⋯	⋯
"	M160	0.350 ± 0.042	0.228 ± 0.030	0.22 ± 0.05	0.41 ± 0.07	0.44 ± 0.06	6.1 ± 1.8	20.1 ± 3.8
NGC 2146	S250	⋯	2.11 ± 0.16	⋯	8.9 ± 1.5	10.4 ± 1.1	⋯	⋯
"	M160	⋯	2.17 ± 0.21	⋯	8.8 ± 1.6	10.8 ± 1.2	202. ± 42.	112. ± 75.
NGC 2798	S250	0.126 ± 0.014	0.091 ± 0.008	0.19 ± 0.06	0.63 ± 0.11	1.54 ± 0.16	⋯	⋯
"	M160	0.123 ± 0.018	0.088 ± 0.010	0.18 ± 0.06	0.61 ± 0.11	1.36 ± 0.14	21.8 ± 3.7	21. ± 5.
NGC 2841	S250	1.25 ± 0.12	0.77 ± 0.14	0.69 ± 0.18	1.14 ± 0.34	0.96 ± 0.12	⋯	⋯
"	M160	1.23 ± 0.12	0.77 ± 0.11	0.68 ± 0.17	1.13 ± 0.25	0.94 ± 0.12	9.9 ± 4.1	56. ± 12.
NGC 2915	S250	0.050 ± 0.008	0.033 ± 0.006	0.022 ± 0.008	0.027 ± 0.009	0.056 ± 0.012	⋯	⋯
"	M160	0.045 ± 0.010	0.030 ± 0.008	0.019 ± 0.008	0.024 ± 0.007	0.047 ± 0.010	1.12 ± 0.34	0.72 ± 1.21
NGC 2976	S250	0.392 ± 0.038	0.267 ± 0.023	0.43 ± 0.10	1.00 ± 0.18	1.40 ± 0.16	⋯	⋯
"	M160	0.377 ± 0.042	0.257 ± 0.026	0.41 ± 0.10	0.96 ± 0.17	1.34 ± 0.15	19.0 ± 3.2	46. ± 9.
NGC 3049	S250	0.043 ± 0.006	0.0291 ± 0.0049	0.048 ± 0.014	0.120 ± 0.024	0.44 ± 0.05	⋯	⋯
"	M160	0.044 ± 0.008	0.031 ± 0.007	0.047 ± 0.013	0.115 ± 0.022	0.404 ± 0.044	2.6 ± 1.3	4.2 ± 1.5
NGC 3077	S250	0.52 ± 0.06	0.35 ± 0.05	0.39 ± 0.10	0.85 ± 0.17	1.49 ± 0.17	⋯	⋯
"	M160	0.52 ± 0.07	0.35 ± 0.06	0.38 ± 0.10	0.84 ± 0.17	1.36 ± 0.15	18.0 ± 4.3	32. ± 8.
NGC 3184	S250	0.52 ± 0.06	0.348 ± 0.040	0.54 ± 0.14	1.37 ± 0.25	1.46 ± 0.18	⋯	⋯
"	M160	0.51 ± 0.07	0.341 ± 0.048	0.53 ± 0.14	1.33 ± 0.24	1.42 ± 0.16	15. ± 5.	63. ± 13.
NGC 3190	S250	0.340 ± 0.038	0.215 ± 0.028	0.188 ± 0.049	0.29 ± 0.06	0.263 ± 0.033	⋯	⋯
"	M160	0.319 ± 0.038	0.203 ± 0.029	0.175 ± 0.045	0.28 ± 0.06	0.245 ± 0.030	4.9 ± 1.5	13.7 ± 2.6
NGC 3198	S250	0.273 ± 0.031	0.184 ± 0.022	0.21 ± 0.10	0.67 ± 0.12	1.07 ± 0.12	⋯	⋯
"	M160	0.274 ± 0.041	0.185 ± 0.029	0.21 ± 0.09	0.66 ± 0.12	1.03 ± 0.12	9.8 ± 2.8	35. ± 8.
NGC 3265	S250	0.0288 ± 0.0041	0.0198 ± 0.0025	0.036 ± 0.010	0.095 ± 0.019	0.291 ± 0.033	⋯	⋯
"	M160	0.0273 ± 0.0040	0.0189 ± 0.0031	0.034 ± 0.010	0.090 ± 0.017	0.269 ± 0.029	2.4 ± 0.9	2.5 ± 0.9
NGC 3351	S250	0.75 ± 0.07	0.488 ± 0.042	0.58 ± 0.14	1.26 ± 0.23	2.52 ± 0.29	⋯	⋯
"	M160	0.74 ± 0.08	0.48 ± 0.05	0.56 ± 0.13	1.23 ± 0.22	2.44 ± 0.26	21. ± 8.	58. ± 14.
NGC 3521	S250	1.88 ± 0.18	1.28 ± 0.11	2.10 ± 0.49	5.8 ± 1.0	5.6 ± 0.6	⋯	⋯
"	M160	1.86 ± 0.19	1.28 ± 0.12	2.07 ± 0.48	5.7 ± 1.0	5.5 ± 0.6	64. ± 22.	203. ± 39.
NGC 3621	S250	1.62 ± 0.24	1.18 ± 0.13	2.2 ± 0.6	4.0 ± 0.7	3.63 ± 0.43	⋯	⋯
"	M160	1.62 ± 0.27	1.18 ± 0.15	2.1 ± 0.6	4.0 ± 0.7	3.60 ± 0.41	46. ± 13.	122. ± 25.
NGC 3627	S250	1.86 ± 0.17	1.28 ± 0.10	2.06 ± 0.47	5.3 ± 0.9	7.5 ± 0.8	⋯	⋯
"	M160	1.88 ± 0.20	1.29 ± 0.13	2.04 ± 0.48	5.2 ± 0.9	7.4 ± 0.8	88. ± 27.	218. ± 35.
NGC 3773	S250	0.0236 ± 0.0031	0.0157 ± 0.0021	0.020 ± 0.006	0.046 ± 0.011	0.143 ± 0.019	⋯	⋯
"	M160	0.0218 ± 0.0036	0.0146 ± 0.0027	0.019 ± 0.005	0.043 ± 0.009	0.129 ± 0.015	1.4 ± 0.5	1.8 ± 0.9
NGC 3938	S250	0.313 ± 0.033	0.213 ± 0.021	0.38 ± 0.09	0.99 ± 0.17	1.10 ± 0.13	⋯	⋯
"	M160	0.308 ± 0.040	0.211 ± 0.026	0.37 ± 0.09	0.96 ± 0.17	1.06 ± 0.12	13.2 ± 4.3	46. ± 10.
NGC 4236	S250	0.22 ± 0.06	0.155 ± 0.047	0.092 ± 0.098	0.15 ± 0.06	0.51 ± 0.08	⋯	⋯
"	M160	0.21 ± 0.06	0.150 ± 0.047	0.087 ± 0.072	0.145 ± 0.048	0.48 ± 0.07	7.8 ± 5.2	16. ± 5.
NGC 4254	S250	0.68 ± 0.06	0.48 ± 0.09	1.29 ± 0.30	3.9 ± 0.7	4.23 ± 0.45	⋯	⋯

Table 5
(Continued)

Galaxy	Mask	IRAC F_ν (Jy)				MIPS F_ν (Jy)		
		3.6 μm	4.5 μm	5.8 μm	8.0 μm	24 μm	70 μm	160 μm
''	M160	0.68 ± 0.07	0.47 ± 0.11	1.26 ± 0.29	3.8 ± 0.8	4.11 ± 0.45	46. ± 14.	127. ± 23.
NGC 4321	S250	0.88 ± 0.09	0.589 ± 0.048	1.04 ± 0.24	2.86 ± 0.49	3.39 ± 0.36	⋯	⋯
''	M160	0.89 ± 0.11	0.60 ± 0.06	1.03 ± 0.25	2.81 ± 0.49	3.33 ± 0.35	38. ± 11.	126. ± 26.
NGC 4536	S250	0.394 ± 0.040	0.293 ± 0.026	0.55 ± 0.14	1.61 ± 0.29	3.43 ± 0.37	⋯	⋯
''	M160	0.389 ± 0.048	0.295 ± 0.039	0.53 ± 0.13	1.59 ± 0.29	3.30 ± 0.35	30. ± 13.	54. ± 11.
NGC 4559	S250	0.402 ± 0.043	0.280 ± 0.029	0.38 ± 0.09	0.84 ± 0.15	1.13 ± 0.14	⋯	⋯
''	M160	0.388 ± 0.047	0.271 ± 0.033	0.37 ± 0.09	0.81 ± 0.14	1.07 ± 0.12	15.7 ± 4.0	46. ± 9.
NGC 4569	S250	0.65 ± 0.06	0.421 ± 0.034	0.47 ± 0.11	0.98 ± 0.17	1.41 ± 0.16	⋯	⋯
''	M160	0.61 ± 0.06	0.395 ± 0.034	0.44 ± 0.10	0.92 ± 0.16	1.32 ± 0.14	10.8 ± 3.9	37. ± 7.
NGC 4579	S250	0.76 ± 0.07	0.490 ± 0.041	0.44 ± 0.11	0.70 ± 0.13	0.79 ± 0.09	⋯	⋯
''	M160	0.74 ± 0.08	0.475 ± 0.043	0.43 ± 0.10	0.68 ± 0.13	0.75 ± 0.08	8.9 ± 2.1	36. ± 6.
NGC 4594	S250	3.26 ± 0.31	2.04 ± 0.17	1.38 ± 0.33	1.22 ± 0.24	0.71 ± 0.09	⋯	⋯
''	M160	3.14 ± 0.30	1.96 ± 0.17	1.33 ± 0.31	1.17 ± 0.23	0.68 ± 0.08	7.4 ± 2.6	36. ± 7.
NGC 4625	S250	0.045 ± 0.005	0.0296 ± 0.0034	0.050 ± 0.015	0.126 ± 0.023	0.132 ± 0.017	⋯	⋯
''	M160	0.044 ± 0.007	0.0291 ± 0.0048	0.049 ± 0.015	0.119 ± 0.022	0.122 ± 0.015	1.83 ± 0.48	4.7 ± 1.2
NGC 4631	S250	1.20 ± 0.11	0.85 ± 0.07	2.2 ± 0.5	5.8 ± 1.0	8.0 ± 0.8	⋯	⋯
''	M160	1.22 ± 0.14	0.88 ± 0.08	2.2 ± 0.5	5.9 ± 1.0	8.0 ± 0.8	134. ± 21.	265. ± 47.
NGC 4725	S250	1.03 ± 0.10	0.66 ± 0.06	0.60 ± 0.16	1.02 ± 0.18	0.85 ± 0.12	⋯	⋯
''	M160	1.03 ± 0.11	0.65 ± 0.07	0.60 ± 0.15	1.00 ± 0.18	0.83 ± 0.10	8.5 ± 4.3	51. ± 9.
NGC 4736	S250	3.29 ± 0.36	2.14 ± 0.21	2.3 ± 0.6	4.8 ± 0.9	5.6 ± 0.6	⋯	⋯
''	M160	3.26 ± 0.36	2.12 ± 0.22	2.3 ± 0.6	4.8 ± 0.8	5.5 ± 0.6	92. ± 29.	163. ± 29.
NGC 4826	S250	2.05 ± 0.18	1.31 ± 0.10	1.22 ± 0.28	2.04 ± 0.35	2.46 ± 0.26	⋯	⋯
''	M160	2.19 ± 0.21	1.40 ± 0.11	1.25 ± 0.29	2.05 ± 0.35	2.43 ± 0.26	52. ± 9.	85. ± 22.
NGC 5055	S250	2.25 ± 0.20	1.51 ± 0.12	2.3 ± 0.6	5.7 ± 1.0	5.7 ± 0.6	⋯	⋯
''	M160	2.28 ± 0.22	1.52 ± 0.13	2.3 ± 0.6	5.7 ± 1.0	5.7 ± 0.6	73. ± 14.	269. ± 44.
NGC 5398	S250	0.038 ± 0.007	0.027 ± 0.005	0.029 ± 0.009	0.058 ± 0.011	0.260 ± 0.029	⋯	⋯
''	M160	0.039 ± 0.010	0.027 ± 0.008	0.029 ± 0.009	0.055 ± 0.012	0.240 ± 0.027	1.8 ± 0.7	2.6 ± 1.0
NGC 5408	S250	0.082 ± 0.021	0.064 ± 0.012	0.041 ± 0.021	0.039 ± 0.010	0.403 ± 0.044	⋯	⋯
''	M160	0.082 ± 0.038	0.064 ± 0.021	0.042 ± 0.036	0.039 ± 0.014	0.370 ± 0.043	3.0 ± 0.6	1.8 ± 0.8
NGC 5457	S250	2.73 ± 0.39	1.83 ± 0.26	3.1 ± 0.9	7.6 ± 1.4	10.9 ± 1.3	⋯	⋯
''	M160	2.74 ± 0.41	1.84 ± 0.27	3.1 ± 0.9	7.6 ± 1.4	10.9 ± 1.2	123. ± 33.	410. ± 82.
NGC 5474	S250	0.101 ± 0.012	0.069 ± 0.008	0.082 ± 0.026	0.103 ± 0.025	0.160 ± 0.026	⋯	⋯
''	M160	0.101 ± 0.015	0.067 ± 0.010	0.082 ± 0.024	0.101 ± 0.022	0.151 ± 0.021	3.4 ± 1.4	8.7 ± 2.5
NGC 5713	S250	0.198 ± 0.020	0.136 ± 0.018	0.39 ± 0.09	1.13 ± 0.20	2.38 ± 0.25	⋯	⋯
''	M160	0.205 ± 0.029	0.137 ± 0.025	0.40 ± 0.10	1.09 ± 0.19	2.35 ± 0.25	23. ± 8.	38. ± 10.
NGC 5866	S250	0.61 ± 0.05	0.390 ± 0.030	0.26 ± 0.06	0.285 ± 0.050	0.214 ± 0.026	⋯	⋯
''	M160	0.55 ± 0.05	0.355 ± 0.029	0.24 ± 0.06	0.265 ± 0.046	0.195 ± 0.022	7.8 ± 1.4	16.5 ± 4.0
NGC 6946	S250	3.4 ± 0.5	2.44 ± 0.32	5.2 ± 1.3	13.8 ± 2.5	19.7 ± 2.1	⋯	⋯
''	M160	3.4 ± 0.6	2.41 ± 0.38	5.1 ± 1.3	13.6 ± 2.4	19.4 ± 2.1	202. ± 59.	438. ± 98.
NGC 7331	S250	1.51 ± 0.16	1.00 ± 0.09	1.59 ± 0.37	4.0 ± 0.7	4.04 ± 0.43	⋯	⋯
''	M160	1.52 ± 0.20	1.01 ± 0.11	1.54 ± 0.37	3.8 ± 0.7	3.91 ± 0.41	58. ± 13.	155. ± 35.
NGC 7793	S250	0.74 ± 0.09	0.503 ± 0.045	0.81 ± 0.21	1.90 ± 0.34	2.12 ± 0.25	⋯	⋯
''	M160	0.74 ± 0.10	0.50 ± 0.06	0.80 ± 0.21	1.88 ± 0.33	2.09 ± 0.23	33. ± 8.	108. ± 22.
IC 3583	S250	0.037 ± 0.005	0.0237 ± 0.0030	0.019 ± 0.007	0.034 ± 0.009	0.048 ± 0.010	⋯	⋯
''	M160	0.034 ± 0.007	0.0224 ± 0.0040	0.017 ± 0.005	0.033 ± 0.008	0.045 ± 0.007	0.84 ± 0.31	1.8 ± 0.7
NGC 0586	S250	0.00063 ± 0.00221	0.00031 ± 0.00132	−.0006 ± 0.0031	−.0001 ± 0.0032	0.029 ± 0.006	⋯	⋯
''	M160	0.00061 ± 0.00563	0.00051 ± 0.00264	−.0002 ± 0.0026	−.0000 ± 0.0021	0.0254 ± 0.0041	0.36 ± 0.33	1.3 ± 0.6
NGC 1317	S250	0.262 ± 0.028	0.164 ± 0.017	0.159 ± 0.040	0.269 ± 0.049	0.253 ± 0.030	⋯	⋯
''	M160	0.248 ± 0.030	0.156 ± 0.020	0.149 ± 0.037	0.253 ± 0.046	0.234 ± 0.027	5.1 ± 1.1	10.6 ± 2.6
NGC 1481	S250	0.0148 ± 0.0025	⋯	0.0132 ± 0.0041	⋯	0.050 ± 0.007	⋯	⋯
''	M160	0.019 ± 0.007	⋯	0.016 ± 0.007	⋯	0.052 ± 0.008	0.62 ± 0.74	0.73 ± 0.46
NGC 1510	S250	0.0149 ± 0.0017	0.0106 ± 0.0011	0.0102 ± 0.0027	0.0193 ± 0.0037	0.127 ± 0.014	⋯	⋯
''	M160	0.024 ± 0.005	0.0172 ± 0.0046	0.0133 ± 0.0043	0.024 ± 0.006	0.134 ± 0.016	1.08 ± 0.48	1.3 ± 0.5
NGC 3187	S250	0.0249 ± 0.0048	0.019 ± 0.005	0.030 ± 0.009	0.064 ± 0.014	0.101 ± 0.014	⋯	⋯
''	M160	0.027 ± 0.010	0.021 ± 0.010	0.029 ± 0.010	0.061 ± 0.018	0.093 ± 0.013	1.25 ± 0.46	3.8 ± 1.1
NGC 4533	S250	0.0158 ± 0.0023	0.0100 ± 0.0017	0.0088 ± 0.0047	0.022 ± 0.006	0.030 ± 0.007	⋯	⋯
''	M160	0.0165 ± 0.0042	0.0098 ± 0.0026	0.0067 ± 0.0047	0.021 ± 0.007	0.029 ± 0.007	0.51 ± 0.35	1.1 ± 0.8
NGC 7335	S250	0.047 ± 0.007	0.0305 ± 0.0034	0.021 ± 0.006	0.027 ± 0.006	0.0299 ± 0.0049	⋯	⋯
''	M160	0.040 ± 0.008	0.0260 ± 0.0043	0.020 ± 0.006	0.027 ± 0.006	0.0294 ± 0.0046	0.54 ± 0.17	1.6 ± 0.5
NGC 7337	S250	0.0278 ± 0.0040	0.0179 ± 0.0022	0.0135 ± 0.0040	0.0215 ± 0.0045	0.0201 ± 0.0035	⋯	⋯
''	M160	0.024 ± 0.006	0.0156 ± 0.0036	0.0117 ± 0.0042	0.019 ± 0.005	0.0171 ± 0.0031	0.33 ± 0.25	0.89 ± 0.40

Table 6
Herschel Photometry of KINGFISH Galaxies with Dust Detections

Galaxy	Mask	PACS F_ν (Jy)			SPIRE F_ν (Jy)		
		70 μm	100 μm	160 μm	250 μm	350 μm	500 μm
Hol2	S250	4.3 ± 3.1	4.2 ± 3.7	3.2 ± 2.5	1.8 ± 0.5	···	···
”	M160	4.1 ± 2.4	4.0 ± 2.9	2.9 ± 2.0	1.70 ± 0.39	0.96 ± 0.25	0.44 ± 0.14
IC 342	S250	465. ± 230.	904. ± 402.	1108. ± 325.	587. ± 81.	···	···
”	M160	462. ± 196.	901. ± 336.	1101. ± 293.	584. ± 81.	262. ± 37.	97. ± 14.
IC 2574	S250	5.8 ± 5.9	6.6 ± 7.0	8.5 ± 5.7	6.4 ± 1.7	···	···
”	M160	5.4 ± 4.2	6.0 ± 4.8	7.9 ± 4.7	6.0 ± 1.3	3.9 ± 0.8	1.79 ± 0.44
NGC 0337	S250	13.8 ± 3.9	21. ± 6.	19.8 ± 4.0	8.4 ± 1.1	···	···
”	M160	12.9 ± 3.7	20. ± 6.	18.6 ± 3.6	7.8 ± 1.1	3.6 ± 0.6	1.42 ± 0.23
NGC 0628	S250	41. ± 18.	81. ± 27.	113. ± 19.	61. ± 8.	···	···
”	M160	40. ± 15.	79. ± 22.	109. ± 17.	59. ± 7.	27.5 ± 3.3	10.6 ± 1.4
NGC 0925	S250	15. ± 8.	29. ± 11.	37. ± 8.	24.4 ± 3.2	···	···
”	M160	15. ± 6.	27. ± 9.	36. ± 7.	23.1 ± 2.8	13.1 ± 1.6	5.9 ± 0.8
NGC 1097	S250	79. ± 36.	126. ± 56.	134. ± 36.	67. ± 8.	···	···
”	M160	78. ± 29.	124. ± 48.	131. ± 35.	65. ± 7.	28.5 ± 3.2	10.3 ± 1.3
NGC 1266	S250	16. ± 6.	18. ± 8.	12. ± 5.	4.4 ± 0.6	···	···
”	M160	14.5 ± 4.4	17. ± 7.	11.2 ± 4.1	4.1 ± 0.5	1.59 ± 0.23	0.52 ± 0.10
NGC 1291	S250	4.6 ± 24.9	8.4 ± 27.6	24. ± 18.	16.3 ± 3.9	···	···
”	M160	4.4 ± 18.2	8.3 ± 18.1	23. ± 13.	15.7 ± 2.5	8.6 ± 1.5	3.4 ± 0.9
NGC 1316	S250	5.3 ± 2.4	9.9 ± 3.9	10.8 ± 2.7	4.8 ± 0.7	···	···
”	M160	5.0 ± 1.9	9.3 ± 3.4	10.2 ± 2.5	4.6 ± 0.6	1.88 ± 0.28	0.66 ± 0.13
NGC 1377	S250	7.6 ± 2.6	6.9 ± 3.0	3.9 ± 1.5	1.37 ± 0.29	···	···
”	M160	7.0 ± 1.7	6.3 ± 2.2	3.6 ± 1.2	1.22 ± 0.18	0.50 ± 0.09	0.171 ± 0.050
NGC 1482	S250	43. ± 17.	54. ± 23.	43. ± 10.	15.4 ± 1.8	···	···
”	M160	41. ± 13.	52. ± 19.	41. ± 10.	14.6 ± 1.6	5.5 ± 0.7	1.64 ± 0.29
NGC 1512	S250	7.0 ± 2.2	13.7 ± 3.8	18.3 ± 3.2	10.2 ± 1.3	···	···
”	M160	7.2 ± 3.1	12.9 ± 4.1	18.6 ± 4.0	11.2 ± 1.4	5.6 ± 0.8	2.22 ± 0.36
NGC 2146	S250	200. ± 37.	242. ± 140.	182. ± 96.	63. ± 7.	···	···
”	M160	194. ± 42.	235. ± 105.	176. ± 75.	62. ± 7.	22.6 ± 2.5	7.2 ± 0.9
NGC 2798	S250	26. ± 7.	30. ± 10.	21.9 ± 5.0	8.1 ± 1.0	···	···
”	M160	24.6 ± 4.5	28. ± 8.	20. ± 5.	7.6 ± 0.9	2.88 ± 0.36	0.89 ± 0.16
NGC 2841	S250	11. ± 10.	29. ± 15.	50. ± 13.	33.9 ± 4.5	···	···
”	M160	11. ± 8.	28. ± 11.	48. ± 13.	32.9 ± 3.8	15.9 ± 1.9	6.3 ± 0.9
NGC 2915	S250	1.1 ± 0.7	2.0 ± 1.4	1.8 ± 1.2	0.62 ± 0.23	···	···
”	M160	0.98 ± 0.52	1.7 ± 1.2	1.5 ± 1.1	0.46 ± 0.24	0.24 ± 0.13	0.098 ± 0.062
NGC 2976	S250	22. ± 6.	38. ± 9.	47. ± 9.	24.6 ± 3.1	···	···
”	M160	20.6 ± 4.5	36. ± 8.	45. ± 9.	23.6 ± 3.1	11.4 ± 1.5	4.4 ± 0.6
NGC 3049	S250	4.0 ± 2.2	5.7 ± 3.1	5.4 ± 2.0	2.78 ± 0.44	···	···
”	M160	3.7 ± 1.7	5.1 ± 2.4	4.9 ± 1.5	2.45 ± 0.32	1.32 ± 0.18	0.67 ± 0.10
NGC 3077	S250	21. ± 7.	30. ± 11.	30. ± 8.	15.3 ± 2.2	···	···
”	M160	20. ± 6.	29. ± 9.	29. ± 8.	15.0 ± 2.0	7.3 ± 1.0	2.94 ± 0.46
NGC 3184	S250	18. ± 13.	39. ± 17.	55. ± 15.	33.4 ± 4.6	···	···
”	M160	18. ± 9.	38. ± 13.	54. ± 13.	32.3 ± 3.8	15.3 ± 1.9	5.8 ± 0.9
NGC 3190	S250	6.5 ± 2.9	12.0 ± 4.1	15.7 ± 3.7	8.5 ± 1.1	···	···
”	M160	5.9 ± 2.3	11.2 ± 3.3	14.6 ± 2.8	7.9 ± 0.9	3.39 ± 0.41	1.16 ± 0.18
NGC 3198	S250	11.7 ± 4.4	24. ± 9.	31. ± 8.	18.6 ± 2.3	···	···
”	M160	11.4 ± 3.8	23. ± 9.	29. ± 8.	17.8 ± 2.1	9.3 ± 1.1	3.9 ± 0.5
NGC 3265	S250	3.5 ± 1.6	3.7 ± 2.0	2.9 ± 1.2	1.26 ± 0.25	···	···
”	M160	3.2 ± 1.2	3.4 ± 1.7	2.6 ± 1.0	1.15 ± 0.16	0.51 ± 0.09	0.199 ± 0.047
NGC 3351	S250	27. ± 14.	50. ± 23.	55. ± 17.	31.9 ± 4.0	···	···
”	M160	26. ± 11.	48. ± 18.	53. ± 15.	30.8 ± 3.5	13.8 ± 1.6	4.8 ± 0.7
NGC 3521	S250	83. ± 28.	168. ± 51.	210. ± 36.	108. ± 12.	···	···
”	M160	81. ± 26.	165. ± 48.	206. ± 38.	107. ± 12.	46. ± 5.	16.6 ± 2.1
NGC 3621	S250	52. ± 20.	100. ± 32.	130. ± 27.	67. ± 9.	···	···
”	M160	51. ± 18.	98. ± 27.	128. ± 26.	67. ± 8.	31.7 ± 3.8	12.8 ± 1.7
NGC 3627	S250	109. ± 32.	192. ± 56.	201. ± 30.	92. ± 10.	···	···
”	M160	107. ± 31.	190. ± 55.	198. ± 37.	92. ± 10.	37.0 ± 4.2	12.4 ± 1.6
NGC 3773	S250	1.5 ± 1.1	2.2 ± 1.5	2.4 ± 1.2	1.06 ± 0.22	···	···
”	M160	1.3 ± 0.8	2.0 ± 1.2	2.1 ± 0.9	0.92 ± 0.14	0.42 ± 0.07	0.148 ± 0.043
NGC 3938	S250	16. ± 8.	30. ± 12.	41. ± 10.	22.9 ± 3.0	···	···
”	M160	15. ± 6.	29. ± 10.	39. ± 10.	22.1 ± 2.6	10.1 ± 1.2	3.8 ± 0.5
NGC 4236	S250	7.4 ± 10.2	11. ± 13.	16. ± 8.	10.8 ± 2.3	···	···
”	M160	6.7 ± 8.0	10. ± 10.	14. ± 6.	10.2 ± 1.5	6.5 ± 1.0	3.3 ± 0.6
NGC 4254	S250	61. ± 18.	113. ± 30.	129. ± 21.	62. ± 7.	···	···

Table 6
(Continued)

Galaxy	Mask	PACS F_ν(Jy)			SPIRE F_ν(Jy)		
		70 μm	100 μm	160 μm	250 μm	350 μm	500 μm
"	M160	59. ± 17.	110. ± 30.	125. ± 23.	61. ± 7.	24.7 ± 2.8	8.3 ± 1.0
NGC 4321	S250	45. ± 15.	90. ± 27.	118. ± 25.	63. ± 7.	⋯	⋯
"	M160	45. ± 14.	88. ± 26.	115. ± 27.	62. ± 7.	26.8 ± 3.1	9.2 ± 1.2
NGC 4536	S250	41. ± 17.	57. ± 22.	56. ± 11.	26.8 ± 3.1	⋯	⋯
"	M160	40. ± 15.	55. ± 19.	54. ± 11.	25.9 ± 2.9	11.6 ± 1.4	4.5 ± 0.6
NGC 4559	S250	19. ± 6.	35. ± 11.	43. ± 9.	25.0 ± 3.1	⋯	⋯
"	M160	18.3 ± 4.9	34. ± 9.	41. ± 9.	24.0 ± 2.9	12.6 ± 1.5	5.5 ± 0.7
NGC 4569	S250	15. ± 6.	32. ± 11.	40. ± 7.	20.8 ± 2.4	⋯	⋯
"	M160	14.0 ± 4.5	30. ± 9.	38. ± 7.	19.5 ± 2.1	8.2 ± 0.9	2.81 ± 0.36
NGC 4579	S250	10.6 ± 3.9	27. ± 7.	35. ± 6.	19.7 ± 2.3	⋯	⋯
"	M160	10.2 ± 3.1	25. ± 6.	33. ± 6.	18.7 ± 2.1	8.2 ± 0.9	2.88 ± 0.39
NGC 4594	S250	8.4 ± 4.4	26. ± 9.	38. ± 7.	23.5 ± 2.8	⋯	⋯
"	M160	7.9 ± 3.5	25. ± 8.	36. ± 7.	22.4 ± 2.6	10.8 ± 1.3	4.3 ± 0.6
NGC 4625	S250	1.7 ± 1.0	3.8 ± 2.0	4.9 ± 1.4	2.49 ± 0.38	⋯	⋯
"	M160	1.6 ± 0.8	3.5 ± 1.6	4.4 ± 1.4	2.28 ± 0.28	1.11 ± 0.15	0.47 ± 0.09
NGC 4631	S250	141. ± 27.	235. ± 48.	244. ± 37.	116. ± 12.	⋯	⋯
"	M160	139. ± 25.	232. ± 49.	243. ± 47.	117. ± 12.	53. ± 6.	20.6 ± 2.4
NGC 4725	S250	11. ± 7.	27. ± 12.	47. ± 10.	30.5 ± 3.9	⋯	⋯
"	M160	11. ± 6.	26. ± 10.	45. ± 10.	29.9 ± 3.6	15.5 ± 1.9	6.3 ± 0.9
NGC 4736	S250	109. ± 43.	170. ± 60.	151. ± 30.	65. ± 9.	⋯	⋯
"	M160	108. ± 35.	168. ± 52.	148. ± 30.	64. ± 7.	26.2 ± 3.4	9.1 ± 1.4
NGC 4826	S250	57. ± 13.	97. ± 28.	92. ± 24.	38.2 ± 4.1	⋯	⋯
"	M160	55. ± 11.	95. ± 24.	91. ± 22.	38.1 ± 4.1	15.2 ± 1.8	5.1 ± 0.7
NGC 5055	S250	82. ± 21.	183. ± 42.	249. ± 42.	138. ± 15.	⋯	⋯
"	M160	82. ± 18.	180. ± 39.	245. ± 46.	137. ± 15.	60. ± 7.	21.7 ± 2.5
NGC 5398	S250	2.6 ± 1.4	3.4 ± 1.8	2.8 ± 1.1	1.74 ± 0.30	⋯	⋯
"	M160	2.3 ± 1.1	3.2 ± 1.7	2.5 ± 1.1	1.59 ± 0.22	0.87 ± 0.13	0.41 ± 0.08
NGC 5408	S250	3.5 ± 1.2	3.3 ± 1.5	2.2 ± 0.9	0.80 ± 0.21	⋯	⋯
"	M160	3.1 ± 1.0	2.9 ± 1.2	2.0 ± 0.8	0.71 ± 0.14	0.37 ± 0.08	0.123 ± 0.049
NGC 5457	S250	136. ± 56.	268. ± 93.	348. ± 82.	203. ± 26.	⋯	⋯
"	M160	136. ± 45.	267. ± 80.	347. ± 82.	202. ± 23.	100. ± 12.	41. ± 5.
NGC 5474	S250	4.4 ± 3.3	8.0 ± 4.9	7.7 ± 3.2	4.8 ± 0.8	⋯	⋯
"	M160	4.3 ± 2.6	7.9 ± 4.4	7.1 ± 2.8	4.6 ± 0.6	2.64 ± 0.38	1.23 ± 0.21
NGC 5713	S250	30. ± 9.	44. ± 15.	41. ± 10.	16.3 ± 1.9	⋯	⋯
"	M160	28. ± 10.	42. ± 14.	40. ± 10.	16.6 ± 2.0	6.8 ± 0.9	2.28 ± 0.39
NGC 5866	S250	9.2 ± 3.2	18. ± 6.	18.2 ± 4.5	7.8 ± 0.9	⋯	⋯
"	M160	8.4 ± 2.0	16.7 ± 4.5	16.7 ± 4.1	7.1 ± 0.8	2.89 ± 0.34	0.94 ± 0.14
NGC 6946	S250	260. ± 75.	465. ± 136.	531. ± 112.	249. ± 29.	⋯	⋯
"	M160	255. ± 63.	455. ± 116.	519. ± 100.	244. ± 28.	101. ± 12.	35.2 ± 4.3
NGC 7331	S250	68. ± 16.	138. ± 35.	175. ± 35.	89. ± 10.	⋯	⋯
"	M160	65. ± 15.	133. ± 33.	169. ± 35.	87. ± 9.	38.3 ± 4.2	14.2 ± 1.6
NGC 7793	S250	36. ± 14.	71. ± 24.	91. ± 23.	54. ± 7.	⋯	⋯
"	M160	36. ± 13.	70. ± 23.	89. ± 23.	53. ± 6.	27.9 ± 3.2	11.9 ± 1.5
IC 3583	S250	1.1 ± 0.7	2.0 ± 1.1	2.1 ± 0.7	1.27 ± 0.24	⋯	⋯
"	M160	0.96 ± 0.54	1.8 ± 0.9	2.0 ± 0.7	1.16 ± 0.19	0.62 ± 0.10	0.25 ± 0.06
NGC 0586	S250	0.29 ± 0.62	0.85 ± 0.91	1.4 ± 0.6	0.92 ± 0.18	⋯	⋯
"	M160	0.27 ± 0.46	0.76 ± 0.72	1.2 ± 0.6	0.80 ± 0.12	0.38 ± 0.07	0.130 ± 0.035
NGC 1317	S250	6.1 ± 1.9	10.9 ± 3.3	11.1 ± 2.8	5.0 ± 0.7	⋯	⋯
"	M160	5.6 ± 1.4	10.2 ± 3.0	10.3 ± 2.7	4.6 ± 0.6	1.88 ± 0.24	0.64 ± 0.10
NGC 1481	S250	1.0 ± 0.5	1.0 ± 0.5	0.88 ± 0.33	0.41 ± 0.08	⋯	⋯
"	M160	1.3 ± 0.9	0.93 ± 0.81	0.73 ± 0.54	0.42 ± 0.08	0.183 ± 0.049	0.024 ± 0.034
NGC 1510	S250	1.12 ± 0.27	1.19 ± 0.32	0.97 ± 0.25	0.43 ± 0.07	⋯	⋯
"	M160	1.5 ± 0.8	1.3 ± 0.8	1.3 ± 0.6	0.78 ± 0.15	0.44 ± 0.09	0.22 ± 0.06
NGC 3187	S250	1.5 ± 1.0	2.6 ± 1.3	3.9 ± 1.1	2.47 ± 0.36	⋯	⋯
"	M160	1.4 ± 0.9	2.2 ± 1.2	3.6 ± 1.2	2.32 ± 0.31	1.33 ± 0.18	0.63 ± 0.11
NGC 4533	S250	0.43 ± 0.49	1.4 ± 0.8	1.6 ± 0.6	0.95 ± 0.16	⋯	⋯
"	M160	0.50 ± 0.61	1.3 ± 0.7	1.5 ± 0.7	0.82 ± 0.14	0.40 ± 0.08	0.190 ± 0.043
NGC 7335	S250	0.60 ± 0.44	1.5 ± 0.7	1.7 ± 0.5	1.03 ± 0.17	⋯	⋯
"	M160	0.56 ± 0.29	1.3 ± 0.6	1.5 ± 0.5	0.91 ± 0.15	0.42 ± 0.07	0.171 ± 0.034
NGC 7337	S250	0.17 ± 0.33	0.62 ± 0.62	0.81 ± 0.39	0.69 ± 0.11	⋯	⋯
"	M160	0.14 ± 0.35	0.46 ± 0.51	0.67 ± 0.39	0.57 ± 0.10	0.27 ± 0.05	0.097 ± 0.022

claim dust detections, the SPIRE500 flux for our M160 galaxy mask is within 10% of the global SPIRE500 photometry from Dale et al. (2017). Thus, we are not missing a significant reservoir of dust in the outer parts of the disk.[36]

4.5. Gas Masses

For galaxies observed by THINGS, H I 21 cm line intensities were extracted over the area of the M160-resolution galaxy mask for each galaxy. The H I column density $N(\text{H I})$ was estimated assuming the 21 cm emission to be optically thin.

For the 38 galaxies in the HERACLES sample, $^{12}\text{CO}(2\text{–}1)$ line fluxes were obtained by integrating over the M160-resolution galaxy mask, and the H_2 mass was estimated from the CO $2 \rightarrow 1$ line flux assuming $T_B(2 \rightarrow 1)/T_B(1 \rightarrow 0) = 0.7$ and a standard conversion factor[37] $X_{\text{CO},1-0} = 2 \times 10^{20}\text{H}_2 \text{ cm}^{-2}(\text{K km s}^{-1})^{-1}$. The adopted X_{CO} value is representative of the values found in 26 nearby star-forming galaxies by Sandstrom et al. (2013).

For NGC 1266, we use the integrated CO emission and the lower bound on the H I mass from Alatalo et al. (2011).

5. Dust Modeling

5.1. DL07 Dust Model

We employ the DL07 dust model, using "Milky Way" grain size distributions (Weingartner & Draine 2001a). DL07 described the construction of the dust model, and AD12 described its usage in the context of the KINGFISH galaxies. The DL07 dust model has a mixture of amorphous silicate grains and carbonaceous grains, with a distribution of grain sizes. The distribution of grain sizes was chosen to reproduce the wavelength dependence of interstellar extinction within a few kiloparsecs of the Sun (Weingartner & Draine 2001a). The silicate and carbonaceous content of the dust grains was constrained by observations of the gas phase depletions in the ISM. It is assumed that the radiation field heating the dust has a universal spectrum, taken to be that of the local interstellar radiation field estimated by Mathis et al. (1983), scaled by a dimensionless factor U. Following DL07, we assume that in each pixel there is dust exposed to radiation with a single intensity $U_{\min}$, and also dust heated by a power-law distribution of starlight intensities with $U_{\min} < U < U_{\max}$:

$$\frac{dM_{\rm d}}{dU} = (1 - \gamma)M_{\rm d}\delta(U - U_{\min}) + \gamma M_{\rm d}\frac{(\alpha - 1)U^{-\alpha}}{U_{\min}^{1-\alpha} - U_{\max}^{1-\alpha}}, \quad (1)$$

where $M_{\rm d}$ is the total dust mass in the pixel, and γ is the fraction of the dust mass that is heated by the power-law distribution of starlight intensities.

The DL07 model has six adjustable parameters pertaining to the dust and the starlight heating the dust:

1. $q_{\rm PAH}$: fraction of the total grain mass contributed by PAHs containing fewer than 10^3 carbon atoms.
2. $U_{\min}$: intensity of the diffuse ISM radiation field heating the dust, relative to the solar neighborhood.
3. α: exponent of the power-law distribution of heating starlight intensities between $U_{\min}$ and $U_{\max}$. The case

$\alpha = 2$ corresponds to constant dust heating power per logarithmic interval in starlight intensity U; many galaxies seem to be characterized by $\alpha \approx 2$.

4. $U_{\max}$: maximum heating starlight intensity of the power-law distribution of heating starlight intensities.
5. γ: fraction of the dust mass exposed to the power-law distribution of starlight intensities.
6. $M_{\rm d}$: dust mass in the pixel.
   In addition, for modeling the observed fluxes in the IRAC bands, we have an additional adjustable parameter (see AD12):
7. $\Omega_\star$: solid angle subtended by stars within the pixel, determined from the "direct" starlight intensity in the infrared, that is, starlight that directly contributes to the IRAC photometry, without warming the dust. The stars are assumed to have color temperature 5000 K.

The mean starlight intensity seen by the dust is

$$\bar{U} = (1 - \gamma)U_{\min} + \gamma\frac{(\alpha - 1)}{(2 - \alpha)}\frac{U_{\max}^{2-\alpha} - U_{\min}^{2-\alpha}}{U_{\min}^{1-\alpha} - U_{\max}^{1-\alpha}},$$
$$\text{if } \alpha \neq 2, \qquad (2)$$

$$= (1 - \gamma)U_{\min} + \gamma U_{\min}\frac{\ln(U_{\max}/U_{\min})}{1 - (U_{\min}/U_{\max})},$$
$$\text{if } \alpha = 2. \qquad (3)$$

The parameter γ is directly related to f_{PDR}, defined to be the fraction of the total dust luminosity $L_{\rm d}$ that is radiated by dust in regions where $U > 10^2$, typically photodissociation regions (PDRS) near luminous stars:

$$f_{\text{PDR}}$$
$$= \frac{\gamma\left[1 - \left(\frac{100}{U_{\max}}\right)^{2-\alpha}\right]}{(1 - \gamma)\frac{(2-\alpha)}{(\alpha-1)}\left(\frac{U_{\min}}{U_{\max}}\right)^{2-\alpha}\left[1 - \left(\frac{U_{\min}}{U_{\max}}\right)^{\alpha-1}\right] + \gamma\left[1 - \left(\frac{U_{\min}}{U_{\max}}\right)^{2-\alpha}\right]}$$

if $\alpha \neq 2$, or

$$f_{\text{PDR}} = \frac{\gamma \ln\left(\frac{U_{\max}}{100}\right)}{(1 - \gamma)\left(1 - \frac{U_{\min}}{U_{\max}}\right) + \gamma \ln\left(\frac{U_{\max}}{U_{\min}}\right)} \text{ if } \alpha = 2. \quad (4)$$

For each set of dust parameters $(M_{\rm d}, q_{\text{PAH}}, \gamma, U_{\min}, U_{\max}, \alpha)$ and the adopted grain size distribution and grain properties, the dust emission spectrum is computed from first principles. The observed SEDs are consistent with models having $U_{\max} = 10^7$, and we therefore fix $U_{\max} \equiv 10^7$. Moreover, the model emission is linear in $M_{\rm d}$, $L_\star$, and γ (or, equivalently, f_{PDR}), so in the dust fitting algorithms we only need to explore a three-dimensional parameter space (q_{PAH}, $U_{\min}$, and α). The limits on adjustable parameters are given in Table 7. The allowed range for $U_{\min}$ is determined by the wavelength coverage of the data used in the fit.

The region observed is at a distance D from the observer, and Ω_j is the solid angle of pixel j. For each pixel j, the best-fit model vector $\{\Omega_\star, M_{\rm d}, q_{\text{PAH}}, \gamma, U_{\min}, \alpha\}_j$ corresponds to a dust mass surface density:

$$\Sigma_{M_{\rm d},j} \equiv \frac{1}{D^2\Omega_j}M_{{\rm d},j}. \qquad (5)$$

---

[36] For NGC 1512, Dale et al. (2017) find a SPIRE 500 flux that is 39% larger than our value, but part of the difference occurs because they included the companion galaxy NGC 1510, which we have treated separately.

[37] $X_{\text{CO},1-0} = 2 \times 10^{20}\text{H}_2 \text{ cm}^{-2}(\text{K km s}^{-1})^{-1}$ corresponds to $\alpha_{\text{CO},1-0} = 4.35 M_\odot \text{ pc}^{-2}(\text{K km s}^{-1})^{-1}$ if a factor of 1.36 is assumed to allow for helium and heavier elements.

Table 7
Allowed Ranges for Adjustable Parameters

Parameter	Min	Max		Parameter Grid Used
$L_\star$	0	∞		continuous fit
M_d	0	∞		continuous fit
q_{PAH}	0.00	0.10		in steps $\Delta q_{PAH} = 0.001$
f_{PDR}	0.0	$<1.00^a$		continuous fit
U_{min}	0.7	30	when $\lambda_{max} = 160\ \mu m$	in steps $\Delta U_{min} = 0.01^b$
	0.07	30	when $\lambda_{max} = 250\ \mu m$	in steps $\Delta U_{min} = 0.01^b$
	0.01	30	when $\lambda_{max} = 350\ \mu m$	in steps $\Delta U_{min} = 0.01^b$
	0.01	30	when $\lambda_{max} \geqslant 500\ \mu m$	in steps $\Delta U_{min} = 0.01^b$
α	1.0	3.0		in steps $\Delta \alpha = 0.1$
U_{max}	10^7	10^7		not adjusted

Notes.
[a] For each set of U_{min}, U_{max}, and α, there is maximum value of f_{PDR} possible.
[b] The fitting procedure uses precalculated spectra for $U_{min} \in \{0.01, 0.015, 0.02, 0.03, 0.05, 0.07, 0.1, 0.15, 0.2, 0.3, 0.4, 0.5, 0.6, 0.7, 0.8, 1.0, 1.2, 1.5, 2, 2.5, 3.0, 4.0, 5.0, 6.0, 7.0, 8.0, 10, 12, 15, 20, 25, 30\}$ interpolated onto a grid with $\Delta U_{min} = 0.01$.

Similarly, we can compute the infrared luminosity surface density $\Sigma_{L_{d,j}}$ and $\Sigma_{L_{PDR,j}}$, the surface density of dust luminosity from regions with $U > U_{PDR}$, as

$$\Sigma_{L_{d,j}} \equiv \frac{1}{D^2 \Omega_j} L_{d,j}, \qquad \Sigma_{L_{PDR,j}} \equiv \frac{1}{D^2 \Omega_j} f_{PDR,j} L_{d,j}, \qquad (6)$$

where $L_{d,j}$ is the model luminosity radiated by mass $M_{d,j}$ of dust heated by starlight characterized by $(U_{min,j}, \gamma_j, \alpha_j)$.

For each pixel j, we find the best-fit model parameters $\{U_{min,j}, \gamma_j, \alpha_j, M_{d,j}, q_{PAH,j}\}$ by minimizing χ^2, as described by AD12. After the resolved (pixel-by-pixel) modeling of the galaxy is performed, we compute a set of global quantities by adding or taking weighted means (denoted as $\langle ... \rangle$) of the quantities in each individual pixel of the map. The total dust mass M_d, total dust luminosity L_d, and total dust luminosity radiated by dust in regions with $U > 10^2$, $L_{d,tot}$, are given by

$$M_d \equiv \sum_{j=1}^{N} M_{d,j}, \quad L_{PDR} \equiv \sum_{j=1}^{N} L_{d,j},$$

$$L_{PDR} \equiv \sum_{j=1}^{N} L_{PDR,j} = \sum_{j=1}^{N} L_{d,j} f_{PDR,j}, \qquad (7)$$

where the sums extend over all the pixels j that correspond to the target galaxy (i.e., the "galaxy mask" pixels, as described in AD12). The dust-mass-weighted PAH mass fraction $\langle q_{PAH} \rangle$ and mean starlight intensity $\langle \overline{U} \rangle$ are given by

$$\langle q_{PAH} \rangle \equiv \frac{\sum_{j=1}^{N} q_{PAH,j} M_{d,j}}{\sum_{j=1}^{N} M_{d,j}}, \quad \langle U \rangle \equiv \frac{\sum_{j=1}^{N} \overline{U}_j M_{d,j}}{\sum_{j=1}^{N} M_{d,j}}. \qquad (8)$$

We similarly define the dust-mass-weighted minimum starlight intensity

$$\langle U_{min} \rangle \equiv \frac{\sum_{j=1}^{N} U_{min,j} M_{d,j}}{\sum_{j=1}^{N} M_{d,j}}. \qquad (9)$$

The dust-luminosity-weighted value of f_{PDR} is

$$\langle f_{PDR} \rangle \equiv \frac{L_{PDR}}{L_d}. \qquad (10)$$

While the average value of α is of little physical significance (the sum of two power laws is not a power law), for the purpose of discussion we define a representative value

$$\langle \alpha \rangle \equiv \frac{\sum_{j=1}^{N} \gamma_j M_{d,j} U_{min,j} \alpha_j}{\sum_{j=1}^{N} \gamma_j M_{d,j} U_{min,j}}. \qquad (11)$$

We also fit a dust model to the global photometry of each galaxy (i.e., a single-pixel dust model). Below we will compare the result of this single-pixel global model with summing over the fits to individual pixels.

5.2. Post-Planck Renormalization of DL07 Dust Masses and Starlight Intensities

Planck Collaboration et al. (2016) fitted the DL07 dust model to all-sky maps in the *Planck* 857, 545, 353, 217, 143, and 100 GHz (350 μm, 550 μm, 850 μm, 1.4 mm, 2.1 mm, and 3.0 mm) bands; DIRBE 100 μm, 140 μm, and 240 μm bands; IRAS 60 and 100 μm bands; and the *WISE* 12 μm band, to estimate the dust mass surface density for over 50 million 1.7×1.7 pixels. About 270,000 of these pixels contain spectroscopically confirmed Sloan Digital Sky Survey (SDSS) quasars, which were used to estimate the correlation of quasar reddening with the reddening predicted by the DL07 dust model. It was discovered that the DL07 model tends to overpredict the reddening by a factor of ~2. The *Panchromatic Hubble Andromeda Treasury* study of stars in M31 (Dalcanton et al. 2015) also found that the DL07 dust model, if constrained to reproduce the observed infrared emission (Draine et al. 2014), overpredicted the reddening of stars in M31 by a factor of ~2. The SDSS quasars allow the bias factor to be estimated: Planck Collaboration et al. (2016) found that the bias appeared to depend on the value of U_{min}:

$$\frac{E(B-V)_{QSO}}{E(B-V)_{DL07}} \approx 0.42 + 0.28\, U_{min} \text{ for } 0.4 \lesssim U_{min} \lesssim 1.0. \qquad (12)$$

If the reddening $E(B-V)$ has been overestimated, it is reasonable to suppose that the dust mass per area has also been overestimated, by approximately the same factor as the reddening. Therefore, we will correct the DL07 dust mass estimates by the same empirical correction factor as for the reddening.

Figure 2. PACS/MIPS global photometry for the KF62 sample (see Table 1). Eight galaxies where dust was not reliably detected have been excluded (see text). Dashed lines show medians. PACS and MIPS photometry typically differs by ~20% at 70 μm and ~10% at 160 μm, except for outliers (NGC 7337 and NGC 1481 at 70 μm; NGC 2146 and NGC 2915 at 160 μm). PACS70 fluxes are systematically higher than MIPS70.

Because the KINGFISH sample includes some pixels with high $U_{\rm min}$, we choose to limit the *Planck*-derived correction factor for $U_{\rm min} > 1$:

$$\Sigma_{M_{\rm d},{\rm renorm},j} = C_{{\rm dust},j} \times \Sigma_{M_{\rm d},{\rm DL07},j} \qquad (13)$$

$$C_{{\rm dust},j} = 0.42 + 0.28 \min(U_{\rm min,j}, 1.0). \qquad (14)$$

Because the dust models are required to reproduce the dust luminosity, a reduction in the estimated amount of dust implies a corresponding increase in the estimated starlight intensities. Thus we take, for pixel j,

$$\bar{U}_{{\rm renorm},j} = \frac{1}{C_{{\rm dust},j}} \bar{U}_{{\rm DL07},j} \qquad (15)$$

and

$$U_{\rm min,renorm,j} \approx \frac{1}{C_{{\rm dust},j}} U_{\rm min,DL07,j}. \qquad (16)$$

All of the dust and starlight parameters ($M_{\rm d}$, $U_{\rm min}$) reported below are "renormalized" values from Equations (13) and (16).

The above "renormalization" is required because observations indicate that the far-infrared and submillimeter opacity of interstellar dust per unit reddening is somewhat larger than the DL07 model values.[38] We will find below (Table 9) that the global average $\langle C_{\rm dust}\rangle$ for the 62 galaxies ranges from 0.45 to 0.69, with median $\langle C_{\rm dust}\rangle = 0.62$. Thus the typical correction relative to the DL07 model is a reduction in $M_{\rm d}$ by a factor of ~0.62.

Because Equation (13) has $C_{\rm dust} = 0.70$ for $U_{\rm min} \geqslant 1$, the estimated dust-to-gas ratios (DGR) in regions with $U_{\rm min} \geqslant 1$ are reduced by a constant factor of 0.70. This applies to the study of Sandstrom et al. (2013), which was dominated by regions with $\langle U \rangle > 1$. However, because $C_{\rm dust} = $ constant, the CO-to-H$_2$

ratios found by Sandstrom et al. (2013) are unaffected by the renormalization.

5.3. Why Both MIPS and PACS Are Needed

As discussed by Aniano et al. (2011), the MIPS160 PSF cannot be convolved safely into any of the PSFs of the remaining cameras. Therefore, if we wish to include MIPS160 photometry in the dust modeling, we must "degrade" all other images into the MIPS160 PSF.

There are two reasons why we want to include MIPS160 even though PACS160 imaging is available. First, using the larger PSF increases the S/N for the imaging, thereby allowing photometry to be extended to lower surface brightness regions. Second, there are significant and unexplained discrepancies between PACS160 and MIPS160 photometry. Similar discrepancies are found between PACS70 and MIPS70.

Figure 2 shows histograms of the global PACS70/MIPS70 flux ratio (left panel) and the global PACS160/MIPS160 flux ratio (right panel) for each of the KF62 galaxies with reliable dust detections. Each histogram shows the names of galaxies in the bin: "NGC," "DDO," "Holmberg," and "IC" are abbreviated to "n," "d," "Hol," and "i," respectively.

The PACS70 and MIPS70 bandpasses differ slightly, as do the PACS160 and MIPS160 bandpasses. However, AD12 show that for reasonable dust SEDs, the slight difference in bandpasses can explain differences in reported fluxes of only ≲9% at 70 μm and ~2% at 160 μm, whereas much larger PACS/MIPS discrepancies are often observed.

AD12 (their Appendix F) found that even when the global photometry has PACS/MIPS ≈ 1, the PACS and MIPS images (with PACS convolved to the MIPS PSF) can have local surface brightnesses discrepant by factors as large as 1.5–2.0. Similar discrepancies were found when comparing PACS and MIPS imaging of M31 (Draine et al. 2014) and NGC 4449 (Calzetti et al. 2018).

---

[38] The empirical finding that $C_{\rm dust}$ depends on $U_{\rm min}$ suggests that the dust opacity may decline less rapidly with increasing λ than assumed by DL07.

Figure 2 illustrates that even after summing over the full galaxy mask, PACS70 and MIPS70 often disagree by more than a factor of 1.2, and sometimes up to a factor of 1.4. The median ratio is 1.17.

PACS160 and MIPS160 are generally in better agreement, but often have discrepancies larger than 10%. There are two outliers in Figure 2: NGC 2146 (PACS160/MIPS160 = 1.6) and NGC 2915 (PACS160/MIPS160 = 2.3). The high value of PACS160/MIPS160 for NGC 2146 may be the result of the sublinear response of MIPS160 on the very bright nucleus of NGC 2146. The case of NGC 2915 is unclear: the peak surface brightness is modest. Perhaps the background has been oversubtracted in the MIPS160 image or undersubtracted in the PACS160 image.

Because it is usually unclear why PACS and MIPS disagree (the discrepancies are too large to be attributed to differences in bandpasses), we consider that both PACS and MIPS photometry should be included if we wish to estimate the dust parameters with the best accuracy available. AD12 also found that, for a given camera set, dust parameter estimates do not change significantly when using a broader PSF, so modeling at MIPS160 PSF does not significantly alter the dust parameter estimates. We consider our "gold standard" (i.e., the PSF and camera combination that gives the most accurate dust parameter estimates) to be resolved (i.e., multipixel) modeling done using the MIPS160 PSF, using photometry from all of the IRAC, MIPS, PACS, and SPIRE cameras.

6. Results

For each galaxy in the KF62 sample, Table 9 presents the global dust parameters estimated for the "gold standard" modeling, including information characterizing the intensity of the starlight heating the dust in each galaxy. The modeling was done at MIPS160 PSF, using all the cameras available; we also give results of modeling at S250 resolution.

The given quantities are obtained by summing or averaging over the resolved maps using Equations (7)–(10). The dust masses listed in Table 9 were obtained using the DL07 model, but then "renormalized" following Equation (13). The renormalization factor C_d depends on U_{min} and therefore varies from pixel to pixel. The overall renormalization factor

$$\langle C_{dust} \rangle \equiv \frac{\sum_{j=1}^{N} \Sigma_{Md,renorm,j}}{\sum_{j=1}^{N} \Sigma_{Md,DL07,j}} = \frac{\sum_{j=1}^{N} C_{dust,j} \Sigma_{Md,DL07,j}}{\sum_{j=1}^{N} \Sigma_{Md,DL07,j}} \quad (17)$$

for each galaxy is given in Table 9, for both M160 and S250 resolution. Henceforth, M_d, U_{min}, and $\overline{U}$ will refer to the renormalized values of these quantities (see Equations (13)–(16)).

6.1. One Example: NGC 5457 = M101

To illustrate the quality of the data and the modeling results for the KINGFISH galaxies, we choose the large, nearly face-on spiral NGC 5457 (M101) as an example. As for all our galaxies, the dust mass, PAH abundance, and starlight heating parameters are adjusted separately for each pixel.

The parameter α characterizes the distribution of starlight intensities heating dust within a pixel (see Equation (1)). Figure 3 shows maps of the best-fit α values for the M160- and S250-resolution modeling. At M160 resolution, α is azimuthally coherent but has a notable radial gradient, with $\alpha \approx 1.7$ in the center, and $\alpha \approx 2.3$ beyond galactocentric radius ~ 6 kpc.

While the variation in best-fit α is apparent, these values are all close to $\alpha = 2$, the case where there is equal power per unit $\log U$. At S250 resolution, the S/Ns are lower, and the S350, S500, and M160 cameras are not used; the α map for the S250-resolution modeling shows more pixel-scale variations, but with a radial trend similar to the M160-resolution modeling.

In general, the DL07 model successfully reproduces the resolved SEDs in M101. Figure 4 compares the model 500 μm surface brightness with observations. The upper panel shows modeling at M160 resolution (the observed SPIRE500 intensity is used as a model constraint). The DL07 model is generally within $\pm 10\%$ of the observed SPIRE500 intensity, except at the outer edges of the mask where the S/N is low. The model appears to fall short by $\sim 10\%$ in the outer regions (galactocentric radius ~ 15 kpc $= 0°13$), where the metallicity has dropped to $12 + \log_{10}(O/H) \approx 8.25$ (Li et al. 2013). This could indicate that the frequency dependence of the dust opacity becomes less steep as the metallicity drops, which is consistent with the SED of the SMC (Bot et al. 2010; Israel et al. 2010; Planck Collaboration et al. 2011; Draine & Hensley 2012) and with evidence for a submillimeter excess in galaxies with metallicities $12 + \log_{10}(O/H) \leqslant 8.3$ (Rémy-Ruyer et al. 2013).

The lower panel of Figure 4 compares modeling at S250 resolution (no data longward of 250 μm used to constrain the model) with the SPIRE500 observations. In the bright spiral arms, the 500 μm intensity is overpredicted by $\sim 25\%$. Once again we see a radial gradient: the model overpredicts SPIRE500 in the central regions and underpredicts SPIRE500 at $R \gtrsim 8$ kpc $= 0°07$. In the outer regions the fit is poorer, presumably due to the low S/N at S250 resolution.

Figure 5 shows maps of dust and starlight heating parameters for M101. There are two sets of figures: the first set (rows 1 and 2) corresponds to modeling done at M160 resolution, using data from all (IRAC, MIPS, PACS, and SPIRE) cameras, that is, "gold standard" modeling, and the second (rows 3 and 4) corresponds to modeling done at S250 resolution, using IRAC, MIPS24, PACS, and SPIRE250 cameras. This latter modeling is able to resolve smaller scale structures in the galaxies, but is overall less reliable, particularly in the outer regions where the surface brightness is lower and dust is cooler.

Because of the proximity of M101 ($D = 6.7$ Mpc), the spiral structure is visible even at M160 resolution. At M160 resolution (38″8 FWHM), the dust luminosity/area ranges from the surface brightness $\Sigma_{Ld,min} = 0.67 \, L_\odot \, pc^{-2}$ defining the boundary of the galaxy mask to a peak $\Sigma_{Ld} = 10^{2.5} \, L_\odot \, pc^{-2} \sim 8.5$ kpc ESE of the center, at the position of the giant H II region NGC 5461 (see, e.g., Esteban et al. 2009).

At S250 resolution, the peak at NGC 5461 has a dust/luminosity/area $\Sigma_{Ld} = 10^{3.2} \, L_\odot \, pc^{-2}$ (corresponding to a dust luminosity $L_d = 6 \times 10^7 \, L_\odot$ in a single $195 \times 195 \, pc^2$ S250 map pixel). Thus at S250 resolution, we are able to measure the IR emission from the dust over a dynamic range of ~ 2000 in Σ_{Ld}.

Maps of dust surface density Σ_{Md} are also shown for both the M160 and S250 modeling. At both M160 and S250 resolution, Σ_{Md} has a peak at the extranuclear luminosity peak. At S250 resolution, we estimate a peak dust surface density $5 \times 10^5 \, M_\odot \, kpc^{-2}$, corresponding to $M_d = 2 \times 10^4 \, M_\odot$ of dust in a single S250 map pixel.

Maps of the starlight modeling parameter $U_{min,DL07}$ are also shown at both M160 and S250 resolution. In M101, $U_{min,DL07}$
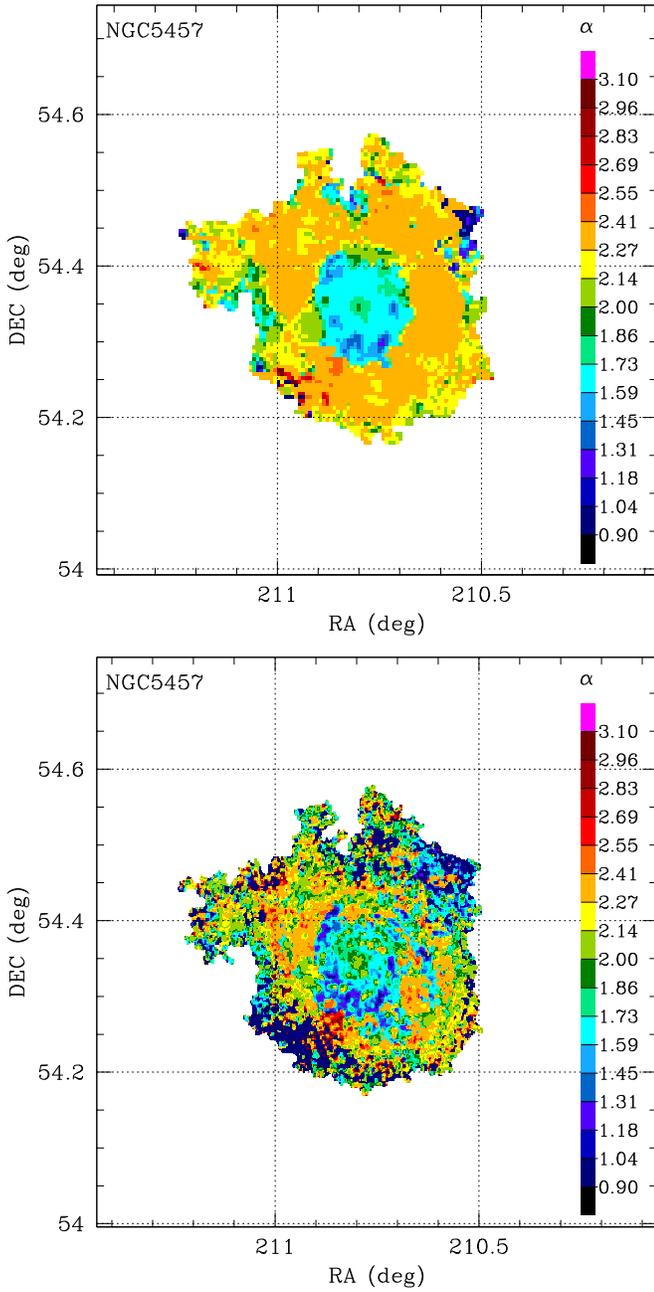
Figure 3. Starlight heating parameter α for NGC 5457 = M101, for modeling at M160 resolution (top) and at S250 resolution (bottom), for the "galaxy mask" defined by $\Sigma_{Ld} > \Sigma_{Ld,min} = 0.67\ L_{\odot}\ pc^{-2}$. At M160 resolution, where all cameras are used to constrain the model, α is azimuthally coherent but with a radial gradient: $\alpha \approx 1.7$ in the center, and $\alpha \approx 2.3$ in the outer regions. The S250 map is noisier, because not all of the cameras can be used, and the S/N of the bands that can be used is reduced.

Figure 4. $I_{\nu}^{model}/I_{\nu}^{obs}$ for NGC 5457, for modeling at M160 resolution (top) and S250 resolution (bottom). At M160 resolution, the model reproduces the SPIRE500 observations to within ∼15%, with a clear radial gradient in model/observation, suggesting a systematic change in the dust opacity with changing metallicity (see text). At S250 resolution, no data longward of 250 μm are used to constrain the model; the predicted 500 μm intensity (after convolving to the SPIRE500 PSF) agrees with observations to within ∼25%. A radial gradient is again seen.

ranges from values as high as 30 (the largest value permitted by our modeling) to values as low as ∼0.07 in the outer parts of the galaxy. The highest values of $U_{min} = 30$ arise in the S250 modeling, with high values of U_{min} appearing in a fraction of pixels in low-surface-brightness regions to the east of the center. The high U_{min} values found in these regions using S250-resolution data are probably unphysical, arising as the result of low-S/N data: an upward fluctuation in PACS70 (or a downward fluctuation in SPIRE250) can drive the fitting to a high U_{min} value. Within ∼5 kpc of the center, with higher surface brightnesses, we generally find $0.5 \lesssim U_{min} \lesssim 4$. And in

the M160 modeling, we do not obtain very high values of U_{min} even in the low-surface-brightness outer regions.

Maps of q_{PAH} are also shown at both M160 and S250 resolution. The modeling finds a very high value of q_{PAH} along the SSE edge of the galaxy; this is seen in both the M160 and S250 modeling of an extended region approximately 12 kpc SSE of the center. The high estimates for q_{PAH} could arise from errors in the IRAC 5.6 and 8 μm photometry, probably due to errors in background subtraction.
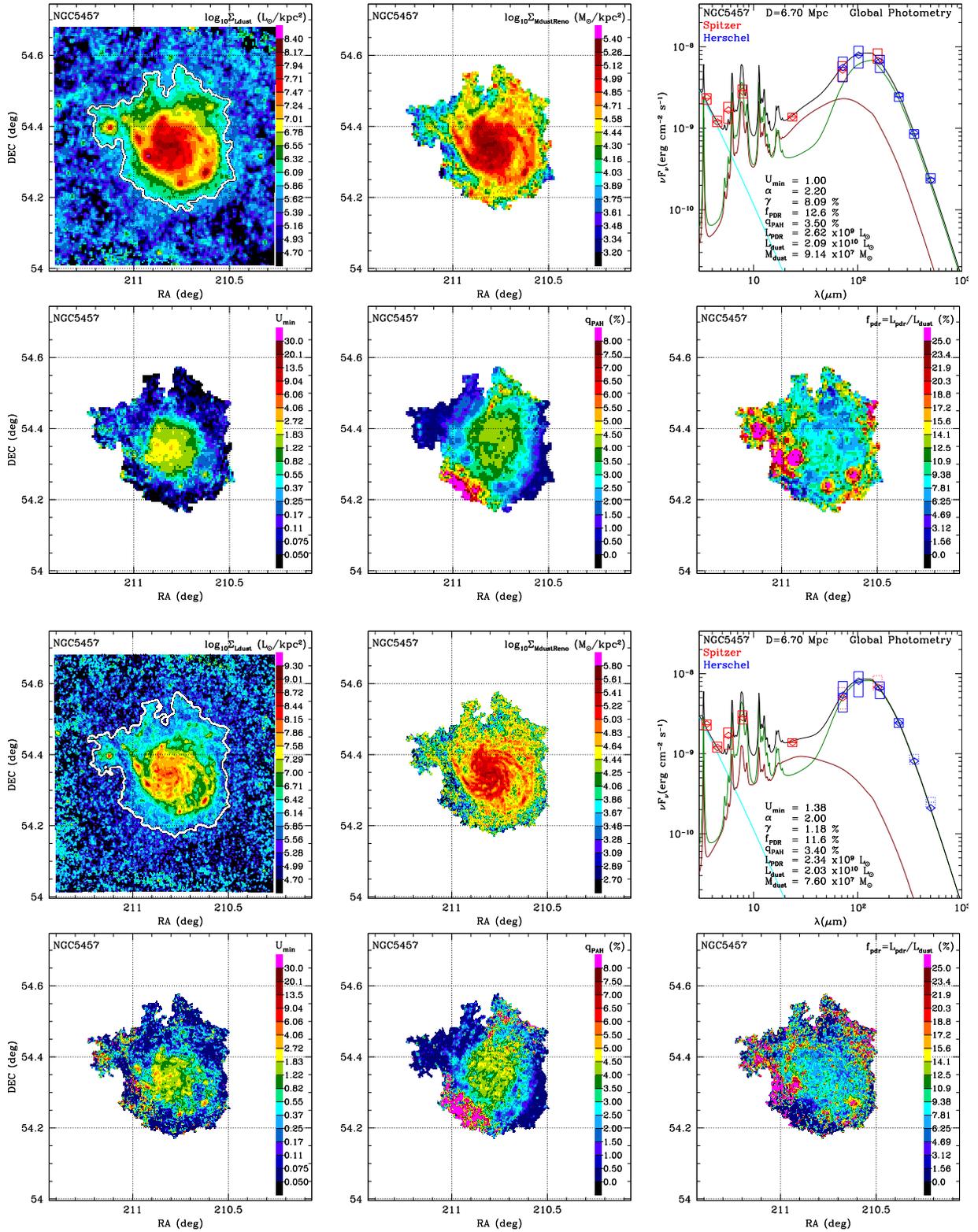
Figure 5. NGC 5457 = M101: model results at M160 PSF (rows 1 and 2) and at S250 PSF (rows 3 and 4). Dust luminosity per area Σ_{Ld} (column 1, rows 1 and 3) is shown for the entire field, with the adopted galaxy mask boundary in white. Dust mass per area Σ_{Md} (column 2, rows 1 and 3) is after renormalization (see text). $U_{min,DL07}$, q_{PAH}, and f_{PDR} are shown in rows 2 and 4. The global SED (column 3, rows 1 and 3) is shown for single-pixel modeling, with contributions from dust heated by U_{min} (green), dust heated by $U > U_{min}$ (red), and starlight (cyan); values of U_{min} and M_d in the figure label are for the DL07 model before renormalization. *Herschel* (blue rectangles) and *Spitzer* (red rectangles) photometry is shown. Diamonds show the band-convolved flux for the model. The horizontal extent of rectangles and diamonds is an arbitrary $\pm10\%$ wavelength range. The vertical extent of photometry rectangles is $\pm1\sigma$.

Table 8
Dust Mass Estimates for NGC 5457 = M101

| PSF | $M_{\rm d}/10^7 M_\odot$ | | | | multipix |
| | DL07 | | renorm. DL07 | | $\langle C_{\rm dust}\rangle$ |
	multipixel	single pixel	multipixel	single pixel	
M160	12.7 ± 0.5	9.14 ± 0.32	6.97 ± 0.20	6.40 ± 0.89	0.549
S250	12.1 ± 2.9	7.60 ± 0.10	6.88 ± 1.34	5.32 ± 0.28	0.569

Maps of $f_{\rm PDR}$—the fraction of the dust luminosity that is contributed by dust heated by starlight with $U > 100$—are shown at both M160 and S250 resolution. High values of $f_{\rm PDR}$ are seen at many of the positions where $\Sigma_{\rm Ld}$ peaks, which is consistent with the idea that these are regions with active star formation, with some fraction of the dust exposed to intense radiation fields in or near OB associations. However, we also see high $f_{\rm PDR}$ values in some of the lowest-surface-brightness regions near the edge of the galaxy mask; this is presumably an indication that photometric errors and errors in background subtraction are leading to overestimation of 24 or 70 μm emission relative to the total dust luminosity. Thus our derived values of $f_{\rm PDR}$ appear to be unreliable in the lowest-surface-brightness regions.

We also show the global SED for M101, extracted from the galaxy mask. In the upper right panel, the rectangular symbols show the measured fluxes $\pm1\sigma$ for the seven *Spitzer* cameras and the six *Herschel* cameras. At 70 and 160 μm, both red and blue rectangles are shown, with the MIPS and PACS photometry. Also shown is a *single-pixel* DL07 model, where the DL07 model is fitted to the global photometry. The diamonds show the model fluxes for each of the instrumental bandpasses. In the case of M101, the model (with six adjustable parameters: $L_\star$, $M_{\rm d}$, $q_{\rm PAH}$, $U_{\rm min}$, γ, α) is consistent with the photometry at 11 independent wavelengths (3.6 μm to 500 μm). In row 3, column 3, we show a single-pixel DL07 model fitted to only the photometry that is used for the S250 modeling (i.e., MIPS70, MIPS160, SPIRE350, or SPIRE500 are *not* used when adjusting the model parameters). The dashed rectangles show these unused measurements; we see that for M101 the single-pixel model does quite well at *predicting* the fluxes at 350 and 500 μm, with only a 1σ underprediction even at 500 μm. The single-pixel global fit parameters are given in the SED plots.

Table 8 compares total dust mass estimates for M101. Column 2 reports the dust mass estimated from the DL07 model at either M160 or S250 resolution, after summing the dust model over the galaxy mask. Because we opted to use the same $\Sigma_{\rm Ld,min}$ for the S250 and M160 modeling, the galaxy masks for the two cases are essentially the same. Column 3 reports the result of fitting a DL07 model to the global photometry; this is referred to as "single pixel" modeling. In columns 4 and 5, we show the multipixel or single-pixel dust masses after renormalizing following Equation (13).

Multipixel versus single-pixel modeling is of course expected to produce different estimates because the models are nonlinear. One notes in Table 8 that the discrepancies between the multipixel and single-pixel mass estimators are reduced when going from the original DL07 model to the renormalized model. It is not clear why this is the case, but this is a welcome result.

6.2. Full KINGFISH Sample

Dust is detected reliably for every galaxy in the KF62 sample. Selected images for each of these galaxies are given in Appendix A (Figures 17.1–17.62), following the scheme used for M101 in Figure 5. This is only a fraction of the maps and images that are available online; see Appendix C for a description of the data set.

The "galaxy mask" for each galaxy is shown for both the M160 PSF and the S250 PSF. As for M101, we have opted to use the same $\Sigma_{\rm Ld,min}$ for both the M160 and S250 modeling, so the M160 and S250 $\Sigma_{\rm Ld,min}$-based galaxy masks are nearly identical for each galaxy, except for the eight where dust emission is so weak that we treat them as nondetections (see Appendix B). The flux densities F_ν measured by *Spitzer* and *Herschel* within the M160 and S250 galaxy masks for each galaxy have been given in Tables 5 and 6. The model-derived parameters for the dust and starlight are given in Table 9. Note that α is not included in Table 9 because there is no natural way to define a "mean" α for multipixel modeling. The uncertainties listed for the parameters are based on repeating the fitting procedure with the "observed" fluxes obtained by Monte Carlo sampling from Gaussian distributions with means and widths given by the original observed values and uncertainty estimates (see discussion in Appendix E of AD12). Systematic errors associated with the DL07 model itself have not been estimated.

Figures 17.1–17.62 have 12 panels in all, with the top six panels showing results of modeling with the M160 PSF, and the lower six panels repeating this for the S250 PSF. For each PSF, the top row shows maps of the dust luminosity surface density $\Sigma_{L_{\rm d}}$ (upper left) and modeled dust surface density $\Sigma_{M_{\rm d}}$ (upper center), and the model SED (upper right). The lower row shows maps of the starlight intensity parameter $U_{\rm min}$ (left), the PAH abundance parameter $q_{\rm PAH}$ (center), and the PDR fraction $f_{\rm PDR}$ (right), all restricted to the "galaxy mask."

In the SED plot, the observed global photometry is represented by rectangular boxes (*Spitzer* IRAC and MIPS in red; *Herschel* PACS and SPIRE in blue). The vertical extent of each box shows the $\pm1\sigma$ uncertainty in the photometry for each band. The black line is the total DL07 model spectrum, and its different components are represented by three colors. The cyan line is the stellar contribution, the dark red line is the emission from dust heated by the power-law U distribution, and the dark green line is emission from dust heated by $U = U_{\rm min}$. The DL07 model used in this SED plot is a single-pixel model, which tries to reproduce the global photometry by treating the entire galaxy as a single pixel. These "single pixel" models generally do a good job at reproducing the global photometry. Multipixel models, where the photometry in every pixel is fit independently, have many more adjustable parameters, and they naturally do an even better job of reproducing the global photometry after summing over all the pixels in the galaxy mask. It is reasonable to presume that

Table 9
Dust Model Parameters for S250 and M160 Galaxy Masks

Galaxy	Mask	$M_{dust}(10^6 M_\odot)$[a]	$q_{PAH}(\%)$	$\langle U_{min}\rangle$[a]	$\langle \bar{U}\rangle$[a]	$f_{PDR}(\%)$	$\langle C_{dust}\rangle$	$L_{dust}(10^9 L_\odot)$
Hol2	S250	0.12 ± 0.05	0.95 ± 0.67	2.4 ± 4.6	3.1 ± 3.7	15.3 ± 4.1	0.500	0.061 ± 0.009
”	M160	0.134 ± 0.033	0.68 ± 0.34	1.0 ± 1.6	2.7 ± 0.9	18.1 ± 3.4	0.491	0.058 ± 0.006
IC 342	S250	$41. \pm 8.$	4.4 ± 0.8	1.9 ± 1.3	2.5 ± 1.2	12.9 ± 2.4	0.614	16.5 ± 2.3
”	M160	$35. \pm 5.$	4.25 ± 0.26	2.2 ± 0.6	2.7 ± 0.5	12.8 ± 3.7	0.640	16.0 ± 0.8
IC 2574	S250	1.08 ± 0.23	0.48 ± 0.07	0.56 ± 0.57	0.95 ± 0.50	11.8 ± 3.7	0.469	0.169 ± 0.025
”	M160	1.17 ± 0.34	0.44 ± 0.27	0.22 ± 0.21	0.85 ± 0.45	12.5 ± 1.0	0.452	0.163 ± 0.015
NGC 0337	S250	10.6 ± 2.2	2.05 ± 0.25	6.3 ± 1.8	7.0 ± 1.9	11.0 ± 2.3	0.685	12.1 ± 1.3
”	M160	12.2 ± 1.0	2.4 ± 0.6	5.0 ± 0.6	5.4 ± 0.6	13.6 ± 0.6	0.678	10.8 ± 0.6
NGC 0628	S250	20.5 ± 1.1	3.5 ± 0.7	1.96 ± 0.44	2.16 ± 0.34	11.5 ± 4.2	0.613	7.3 ± 1.0
”	M160	18.7 ± 1.0	3.6 ± 0.7	2.16 ± 0.21	2.30 ± 0.27	11.4 ± 2.1	0.622	7.08 ± 0.18
NGC 0925	S250	$16. \pm 5.$	2.59 ± 0.36	1.2 ± 1.3	1.5 ± 1.3	8.5 ± 2.5	0.525	3.88 ± 0.36
”	M160	17.1 ± 2.7	2.65 ± 0.47	0.56 ± 0.60	1.32 ± 0.37	9.3 ± 1.2	0.481	3.721 ± 0.027
NGC 1097	S250	$93. \pm 31.$	3.7 ± 0.9	2.4 ± 1.3	2.9 ± 1.2	$16.\pm5.$	0.549	$44. \pm 7.$
”	M160	$65. \pm 7.$	3.2 ± 0.9	3.4 ± 1.0	4.0 ± 0.9	16.6 ± 3.4	0.622	42.6 ± 2.5
NGC 1266	S250	13.2 ± 1.9	0.60 ± 0.16	$13. \pm 5.$	$13.\pm5.$	13.6 ± 3.9	0.576	27.5 ± 4.7
”	M160	9.6 ± 1.0	0.61 ± 0.44	$17. \pm 6.$	15.7 ± 2.6	$15. \pm 5.$	0.635	24.7 ± 2.3
NGC 1291	S250	$25. \pm 7.$	2.6 ± 0.8	0.54 ± 0.49	0.64 ± 0.57	8.4 ± 0.6	0.470	2.7 ± 0.7
”	M160	16.0 ± 4.4	2.4 ± 1.2	0.97 ± 0.27	1.04 ± 0.25	7.6 ± 3.3	0.516	2.72 ± 0.09
NGC 1316	S250	12.0 ± 2.9	1.8 ± 1.0	2.8 ± 1.8	3.2 ± 1.8	10.2 ± 2.7	0.612	6.22 ± 0.45
”	M160	8.7 ± 1.3	1.9 ± 1.3	3.8 ± 0.7	4.2 ± 0.6	10.5 ± 3.1	0.660	5.90 ± 0.31
NGC 1377	S250	2.5 ± 0.6	0.68 ± 0.15	$17.\pm7.$	$34.\pm15.$	56.7 ± 3.7	0.580	13.8 ± 1.3
”	M160	1.48 ± 0.22	0.73 ± 0.80	25.1 ± 3.8	$53.\pm8.$	55.9 ± 1.3	0.673	12.81 ± 0.13
NGC 1482	S250	20.4 ± 2.0	3.05 ± 0.38	13.8 ± 2.2	14.7 ± 2.4	12.2 ± 1.1	0.663	$49.\pm6.$
”	M160	16.6 ± 2.1	3.3 ± 0.5	15.5 ± 3.4	16.9 ± 3.4	11.7 ± 3.5	0.686	46.4 ± 4.8
NGC 1512	S250	10.1 ± 1.3	3.4 ± 0.7	1.63 ± 0.44	1.80 ± 0.41	7.5 ± 1.5	0.584	2.99 ± 0.32
”	M160	12.4 ± 1.2	3.3 ± 0.5	1.48 ± 0.35	1.50 ± 0.26	7.5 ± 1.8	0.553	3.06 ± 0.16
NGC 2146	S250	$53. \pm 13.$	4.1 ± 0.7	14.6 ± 4.5	15.3 ± 3.5	12.6 ± 3.1	0.665	$135. \pm 12.$
”	M160	40.2 ± 2.2	4.2 ± 0.7	17.9 ± 4.4	20.6 ± 1.7	11.8 ± 3.1	0.692	$137. \pm 7.$
NGC 2798	S250	15.8 ± 2.1	1.91 ± 0.41	14.7 ± 3.4	13.9 ± 2.8	14.5 ± 2.1	0.604	36.0 ± 3.9
”	M160	11.4 ± 0.6	2.19 ± 0.28	16.9 ± 2.1	17.99 ± 0.44	13.6 ± 2.0	0.683	33.4 ± 1.2
NGC 2841	S250	$68. \pm 9.$	3.4 ± 1.1	0.84 ± 0.19	0.92 ± 0.15	6.5 ± 3.2	0.540	10.37 ± 0.36
”	M160	53.0 ± 4.0	3.40 ± 0.48	1.11 ± 0.11	1.15 ± 0.11	6.6 ± 2.3	0.584	10.03 ± 0.20
NGC 2915	S250	0.052 ± 0.029	1.3 ± 0.6	3.7 ± 2.0	4.5 ± 1.7	10.1 ± 1.9	0.588	0.0377 ± 0.0046
”	M160	0.031 ± 0.010	1.4 ± 0.7	6.0 ± 2.2	6.6 ± 1.9	11.1 ± 2.0	0.676	0.0332 ± 0.0023
NGC 2976	S250	1.76 ± 0.31	2.93 ± 0.20	2.6 ± 0.6	2.8 ± 0.5	10.6 ± 1.2	0.611	0.800 ± 0.034
”	M160	1.77 ± 0.11	3.2 ± 1.0	1.9 ± 0.5	2.67 ± 0.31	11.4 ± 2.2	0.661	0.778 ± 0.049
NGC 3049	S250	6.6 ± 2.5	1.81 ± 0.21	2.1 ± 4.5	3.6 ± 4.7	27.4 ± 3.0	0.542	3.93 ± 0.32
”	M160	9.5 ± 0.8	2.1 ± 0.6	0.28 ± 0.52	2.09 ± 0.19	33.6 ± 1.5	0.472	3.24 ± 0.11
NGC 3077	S250	1.83 ± 0.33	3.5 ± 0.6	2.2 ± 1.1	2.6 ± 0.9	13.9 ± 1.4	0.506	0.79 ± 0.11
”	M160	1.51 ± 0.15	3.1 ± 0.8	2.69 ± 0.11	3.03 ± 0.33	14.1 ± 2.1	0.529	0.754 ± 0.020
NGC 3184	S250	35.7 ± 4.1	3.8 ± 0.8	1.45 ± 0.28	1.58 ± 0.14	9.8 ± 1.5	0.581	9.4 ± 0.8
”	M160	30.2 ± 2.7	3.8 ± 0.8	1.72 ± 0.21	1.82 ± 0.24	9.6 ± 3.4	0.612	9.08 ± 0.33
NGC 3190	S250	21.6 ± 3.8	3.00 ± 0.26	1.77 ± 0.48	1.87 ± 0.31	4.0 ± 0.5	0.588	6.64 ± 0.24
”	M160	14.8 ± 2.0	2.8 ± 0.5	2.4 ± 0.6	2.55 ± 0.48	3.8 ± 1.3	0.681	6.19 ± 0.33
NGC 3198	S250	26.8 ± 4.0	2.90 ± 0.38	1.4 ± 0.6	1.82 ± 0.47	14.6 ± 1.8	0.581	8.02 ± 0.14
”	M160	28.4 ± 2.8	3.1 ± 0.8	1.49 ± 0.31	1.65 ± 0.39	15.0 ± 3.0	0.555	7.71 ± 0.28
NGC 3265	S250	2.4 ± 1.1	1.73 ± 0.47	5.2 ± 9.3	7.1 ± 9.7	$27. \pm 7.$	0.542	2.74 ± 0.10
”	M160	2.0 ± 0.9	2.30 ± 0.35	4.6 ± 2.4	7.6 ± 2.7	30.1 ± 3.3	0.576	2.49 ± 0.17
NGC 3351	S250	$24. \pm 6.$	3.9 ± 1.5	1.4 ± 0.6	1.9 ± 0.5	$17. \pm 6.$	0.538	7.4 ± 0.9
”	M160	14.9 ± 1.0	3.2 ± 0.6	2.3 ± 0.6	2.85 ± 0.45	17.3 ± 3.8	0.623	6.99 ± 0.45
NGC 3521	S250	$89. \pm 12.$	4.16 ± 0.35	2.21 ± 0.29	2.34 ± 0.40	8.9 ± 2.0	0.586	34.5 ± 0.7
”	M160	$69. \pm 8.$	4.17 ± 0.16	2.8 ± 0.6	2.96 ± 0.39	8.7 ± 4.4	0.648	33.7 ± 1.3
NGC 3621	S250	$20. \pm 6.$	4.18 ± 0.38	2.0 ± 0.8	2.2 ± 0.6	10.8 ± 1.1	0.569	7.39 ± 0.41
”	M160	19.5 ± 3.3	4.8 ± 0.7	2.5 ± 0.7	2.23 ± 0.38	10.7 ± 2.8	0.567	7.28 ± 0.25
NGC 3627	S250	$38. \pm 7.$	3.3 ± 0.7	3.9 ± 1.8	4.3 ± 1.9	12.0 ± 1.5	0.645	27.0 ± 2.7
”	M160	30.1 ± 1.5	3.23 ± 0.32	4.85 ± 0.47	5.43 ± 0.40	11.7 ± 1.9	0.691	26.9 ± 0.8
NGC 3773	S250	1.12 ± 0.49	1.27 ± 0.35	2.6 ± 4.1	3.4 ± 4.0	21.3 ± 4.3	0.519	0.63 ± 0.10
”	M160	0.62 ± 0.07	1.90 ± 0.43	4.0 ± 1.5	5.5 ± 1.0	23.8 ± 3.6	0.631	0.563 ± 0.023
NGC 3938	S250	$52. \pm 14.$	3.71 ± 0.35	1.8 ± 0.7	2.0 ± 0.8	9.7 ± 3.4	0.572	16.9 ± 1.4
”	M160	41.5 ± 2.5	3.7 ± 0.7	2.26 ± 0.30	2.41 ± 0.31	9.3 ± 2.2	0.627	16.5 ± 1.0
NGC 4236	S250	2.12 ± 0.45	0.94 ± 0.32	0.64 ± 0.76	1.1 ± 0.7	14.4 ± 4.3	0.494	0.384 ± 0.043
”	M160	2.6 ± 1.4	0.86 ± 0.39	0.23 ± 0.10	0.85 ± 0.29	15.5 ± 1.7	0.449	0.367 ± 0.038
NGC 4254	S250	$66. \pm 16.$	4.3 ± 1.1	3.4 ± 1.0	3.6 ± 1.1	11.8 ± 3.0	0.631	39.0 ± 3.3
”	M160	51.5 ± 3.6	4.1 ± 0.8	4.03 ± 0.42	4.42 ± 0.33	11.6 ± 1.9	0.685	37.6 ± 0.8

Table 9
(Continued)

Galaxy	Mask	$M_{dust}(10^6 M_\odot)$[a]	$q_{PAH}(\%)$	$\langle U_{min}\rangle$[a]	$\langle \bar{U}\rangle$[a]	$f_{PDR}(\%)$	$\langle C_{dust}\rangle$	$L_{dust}(10^9 L_\odot)$
NGC 4321	S250	83.±13.	4.1 ± 1.7	2.08 ± 0.40	2.26 ± 0.50	10.4 ± 3.7	0.619	31.1 ± 1.7
”	M160	63.5 ± 3.4	3.7 ± 1.2	2.67 ± 0.20	2.92 ± 0.23	10.2 ± 1.7	0.681	30.6 ± 1.6
NGC 4536	S250	32.±10.	2.9 ± 1.2	3.6 ± 1.8	4.3 ± 1.5	18.±8.	0.578	22.6 ± 3.1
”	M160	27.1 ± 4.4	3.4 ± 0.5	4.4 ± 1.3	4.7 ± 0.7	19.8 ± 3.2	0.591	20.8 ± 0.5
NGC 4559	S250	7.71 ± 0.26	2.47 ± 0.42	2.1 ± 0.8	2.16 ± 0.22	9.5 ± 2.4	0.579	2.73 ± 0.15
”	M160	8.5 ± 1.2	2.7 ± 0.8	1.9 ± 0.9	1.89 ± 0.43	10.1 ± 2.1	0.541	2.65 ± 0.15
NGC 4569	S250	12.9 ± 4.0	3.7 ± 0.6	1.9 ± 0.6	2.4 ± 0.7	14.2 ± 1.6	0.635	5.14 ± 0.25
”	M160	9.2 ± 0.8	3.4 ± 0.9	2.63 ± 0.36	3.12 ± 0.33	13.9 ± 1.6	0.694	4.71 ± 0.40
NGC 4579	S250	39.±7.	3.1 ± 0.9	1.55 ± 0.26	1.65 ± 0.28	7.9 ± 2.8	0.611	10.58 ± 0.32
”	M160	29.0 ± 1.0	2.9 ± 0.9	1.88 ± 0.07	2.066 ± 0.046	9.0 ± 1.6	0.675	9.83 ± 0.31
NGC 4594	S250	16.4 ± 3.6	2.6 ± 1.4	1.06 ± 0.26	1.15 ± 0.24	6.2 ± 3.5	0.574	3.10 ± 0.16
”	M160	13.3 ± 1.0	2.6 ± 0.7	1.26 ± 0.11	1.34 ± 0.14	6.6 ± 0.9	0.619	2.94 ± 0.08
NGC 4625	S250	1.47 ± 0.31	3.7 ± 0.9	2.1 ± 0.5	2.23 ± 0.49	9.2 ± 2.8	0.590	0.542 ± 0.025
”	M160	1.18 ± 0.21	4.2 ± 0.9	2.7 ± 0.8	2.6 ± 1.0	9.0 ± 3.7	0.625	0.512 ± 0.021
NGC 4631	S250	28.4 ± 4.1	3.0 ± 0.5	4.4 ± 1.3	4.6 ± 1.4	10.9 ± 1.8	0.669	21.6 ± 1.4
”	M160	31.1 ± 2.9	2.90 ± 0.23	4.9 ± 0.6	4.3 ± 0.6	10.9 ± 1.0	0.631	22.0 ± 0.8
NGC 4725	S250	42.±9.	3.68 ± 0.49	0.90 ± 0.27	0.99 ± 0.23	5.7 ± 1.9	0.541	6.9 ± 0.7
”	M160	37.4 ± 3.7	3.6 ± 0.8	1.09 ± 0.16	1.09 ± 0.19	5.4 ± 2.6	0.566	6.72 ± 0.16
NGC 4736	S250	8.5 ± 0.6	4.2 ± 0.6	4.0 ± 0.8	4.3 ± 0.6	7.0 ± 2.6	0.552	5.99 ± 0.34
”	M160	5.4 ± 0.5	3.70 ± 0.50	6.6 ± 1.7	6.5 ± 1.6	6.7 ± 1.8	0.642	5.8 ± 0.7
NGC 4826	S250	4.0 ± 1.0	2.59 ± 0.39	5.5 ± 2.1	5.8 ± 1.3	6.5 ± 3.4	0.665	3.76 ± 0.16
”	M160	3.46 ± 0.30	2.57 ± 0.16	6.5 ± 1.3	6.5 ± 0.9	6.4 ± 3.6	0.673	3.67 ± 0.33
NGC 5055	S250	63.±14.	4.2 ± 0.8	1.70 ± 0.46	1.79 ± 0.40	7.8 ± 1.3	0.594	18.70 ± 0.44
”	M160	49.0 ± 3.0	3.89 ± 0.23	2.12 ± 0.17	2.28 ± 0.12	7.8 ± 3.8	0.659	18.4 ± 0.6
NGC 5398	S250	0.69 ± 0.16	2.25 ± 0.37	1.4 ± 0.5	3.1 ± 0.8	28.0 ± 2.1	0.528	0.352 ± 0.013
”	M160	0.75 ± 0.22	1.8 ± 0.7	0.61 ± 1.42	2.4 ± 1.6	33.0 ± 4.8	0.488	0.297 ± 0.042
NGC 5408	S250	0.049 ± 0.007	0.14 ± 0.28	8.5 ± 3.8	21.±6.	37.±5.	0.627	0.172 ± 0.016
”	M160	0.047 ± 0.017	0.14 ± 0.64	10.±6.	20.±7.	39.±5.	0.661	0.154 ± 0.009
NGC 5457	S250	69.±13.	3.0 ± 0.6	1.58 ± 0.47	1.79 ± 0.42	12.4 ± 2.2	0.569	20.3 ± 1.2
”	M160	69.7 ± 2.0	3.0 ± 0.9	1.84 ± 0.35	1.77 ± 0.10	12.7 ± 1.8	0.550	20.3 ± 0.6
NGC 5474	S250	1.5 ± 1.2	1.7 ± 0.8	1.5 ± 1.0	1.8 ± 0.9	6.9 ± 2.1	0.552	0.466 ± 0.043
”	M160	1.81 ± 0.29	2.10 ± 0.05	0.40 ± 0.10	1.49 ± 0.27	7.7 ± 1.2	0.489	0.442 ± 0.020
NGC 5713	S250	28.±6.	2.81 ± 0.41	6.8 ± 2.0	7.6 ± 2.1	17.5 ± 4.0	0.639	34.7 ± 3.8
”	M160	28.1 ± 2.4	2.74 ± 0.27	7.3 ± 1.9	7.2 ± 1.1	18.3 ± 3.3	0.610	33.3 ± 1.9
NGC 5866	S250	9.4 ± 0.8	1.7 ± 0.9	3.36 ± 0.31	2.92 ± 0.33	1.3 ± 1.0	0.600	4.48 ± 0.21
”	M160	6.0 ± 0.5	1.6 ± 0.8	4.63 ± 0.41	4.54 ± 0.34	0.32 ± 0.61	0.692	4.46 ± 0.08
NGC 6946	S250	57.±6.	3.5 ± 0.8	3.4 ± 0.6	3.8 ± 0.6	13.5 ± 2.9	0.658	35.7 ± 3.2
”	M160	47.1 ± 4.1	3.5 ± 0.7	3.8 ± 0.6	4.4 ± 0.6	14.3 ± 2.9	0.688	34.1 ± 2.0
NGC 7331	S250	116.±32.	4.2 ± 0.9	2.3 ± 1.0	2.4 ± 1.0	7.6 ± 4.1	0.619	45.7 ± 4.0
”	M160	97.±9.	3.95 ± 0.36	2.79 ± 0.44	2.73 ± 0.42	7.1 ± 1.8	0.641	43.7 ± 2.9
NGC 7793	S250	5.5 ± 1.3	3.0 ± 0.9	1.9 ± 0.8	1.9 ± 0.7	8.1 ± 0.9	0.585	1.76 ± 0.13
”	M160	6.0 ± 0.8	3.2 ± 0.6	2.0 ± 0.9	1.8 ± 0.5	7.9 ± 2.5	0.545	1.78 ± 0.08
IC 3583	S250	1.75 ± 0.08	2.12 ± 0.13	1.53 ± 0.46	1.91 ± 0.32	8.3 ± 1.7	0.569	0.548 ± 0.041
”	M160	1.53 ± 0.23	2.3 ± 0.6	1.82 ± 0.42	2.05 ± 0.38	9.3 ± 0.9	0.523	0.514 ± 0.040
NGC 0586	S250	4.0 ± 1.0	3.873 ± 0.039	0.89 ± 0.62	1.0 ± 0.7	10.9 ± 2.2	0.549	0.67 ± 0.10
”	M160	2.31 ± 0.23	3.78 ± 0.12	1.50 ± 0.31	1.66 ± 0.18	8.6 ± 4.2	0.639	0.633 ± 0.022
NGC 1317	S250	11.3 ± 1.5	3.0 ± 0.7	4.1 ± 1.5	3.7 ± 0.9	4.2 ± 0.8	0.596	6.9 ± 0.6
”	M160	7.6 ± 0.7	3.13 ± 0.28	5.0 ± 1.0	5.1 ± 0.9	3.9 ± 2.2	0.687	6.34 ± 0.38
NGC 1481	S250	0.94 ± 0.15	1.5 ± 1.4	5.9 ± 3.7	6.0 ± 2.1	16.1 ± 2.8	0.567	0.93 ± 0.11
”	M160	0.95 ± 0.24	2.3 ± 1.7	3.6 ± 3.2	5.9 ± 2.4	18.6 ± 4.0	0.578	0.93 ± 0.10
NGC 1510	S250	0.244 ± 0.048	0.60 ± 0.35	4.0 ± 2.9	8.5 ± 3.4	35.1 ± 3.8	0.569	0.339 ± 0.011
”	M160	1.16 ± 0.20	0.70 ± 0.26	0.47 ± 0.12	1.94 ± 0.37	34.9 ± 1.6	0.465	0.367 ± 0.014
NGC 3187	S250	7.5 ± 1.8	1.80 ± 0.48	1.2 ± 1.0	1.4 ± 1.0	11.6 ± 1.8	0.541	1.75 ± 0.21
”	M160	9.1 ± 0.9	2.92 ± 0.30	0.56 ± 0.55	1.12 ± 0.26	11.4 ± 3.5	0.476	1.67 ± 0.13
NGC 4533	S250	1.49 ± 0.27	2.4 ± 0.5	1.5 ± 0.8	1.6 ± 0.7	6.4 ± 2.5	0.538	0.393 ± 0.048
”	M160	1.183 ± 0.043	2.3 ± 0.5	1.5 ± 0.5	1.83 ± 0.16	8.2 ± 1.5	0.534	0.355 ± 0.021
NGC 7335	S250	54.±7.	1.6 ± 0.5	1.35 ± 0.42	1.49 ± 0.36	5.6 ± 2.1	0.573	13.1 ± 1.6
”	M160	38.2 ± 2.9	2.1 ± 0.5	1.9 ± 0.5	2.0 ± 0.5	6.7 ± 3.6	0.608	12.3 ± 1.3
NGC 7337	S250	66. ± 30.	3.51 ± 0.13	0.59 ± 0.27	0.68 ± 0.23	8.6 ± 1.5	0.490	7.4 ± 0.7
”	M160	30. ± 6.	3.1 ± 1.2	1.25 ± 0.31	1.45 ± 0.40	7.3 ± 5.4	0.589	7.0 ± 0.9

Note.
[a] Renormalized as described in Section 5.2.

models that do a better job of reproducing the photometry will also be preferred for dust mass estimation.

The dust mass surface densities and dust luminosities per unit area range over three orders of magnitude in our brightest galaxies. Figures 17.1–17.62 illustrate that the DL07 model does a satisfactory job of fitting the SEDs. Although each pixel is modeled independently of its neighbors, it is noteworthy that the dust parameters are smoothly varying over the confines of the galaxy, except for the low-surface-brightness outer regions at S250 resolution, where the S/N in individual pixels may become low enough that certain dust and starlight parameters, such as $\Sigma_{\rm Md}$ and $U_{\rm min}$, become somewhat noisy.

6.3. Special Cases

6.3.1. NGC 1404

The E1 galaxy NGC 1404 is faint at infrared wavelengths, and there is a foreground star $\sim 180''$ to the SSE. However, NGC 1404 is unambiguously detected in IRAC bands 1–4 and by MIPS24. At $\lambda \geqslant 70$ μm, there appears to be excess emission at the position of NGC 1404, but the surface brightness is low, and the possibility that the emission is from a foreground or background source cannot be excluded (Dale et al. 2012). Using the procedure described in Appendix B, we find a 3σ upper bound $M_{\rm dust} < 2.0 \times 10^6 M_{\odot}$ for NGC 1404.

NGC 1404 has an estimated stellar mass $M_{\star} \approx 8 \times 10^{10} M_{\odot}$, and evolved stars are probably injecting dust at a rate $\dot{M}_{\rm dust} \approx 0.005 \times M_{\star}/10^{10}$ yr $= 0.04 M_{\odot}$ yr^{-1}.[39] Thus the observed dust mass upper limit would be consistent with a dust lifetime $M_{\rm d}/\dot{M}_{\rm dust} \lesssim 5 \times 10^7$ yr. If the ISM in NGC 1404 has a temperature $T \approx 10^7$ K, silicate or carbonaceous dust grains would be eroded by thermal sputtering at a rate $da/dt \approx -1 \times 10^{-10}$ cm yr$^{-1}(n_{\rm H}/{\rm cm}^{-3})$ (Draine & Salpeter 1979) for a grain lifetime $a/|da/dt| = 10^7(a/0.1$ μm$)$ $(0.01$ cm$^{-3}/n_{\rm H})$ yr. The dust mass upper limit would thus be consistent with erosion of $a \approx 0.1$ μm grains by sputtering in a $T \approx 10^7$ K ISM with $n_{\rm H} \gtrsim 0.002$ cm^{-3}.

6.3.2. NGC 1377

NGC 1377 has a compact, dusty core, with an extremely high far-infrared surface brightness. The infrared spectrum (Roussel et al. 2006) shows that it is optically thick at $\lambda \lesssim 20$ μm. Weak PAH emission is detected, but because of the uncertain infrared extinction, it is not possible to reliably estimate the PAH abundance parameter $q_{\rm PAH}$. The dust mass estimates should also be regarded as uncertain because of the unusual nature of the ISM in this galaxy.

6.4. Gold Standard DL07 Fit Results for KINGFISH Galaxies

Figure 6 shows the dust parameter distributions for the 61 KINGFISH galaxies plus nine "extras." The dust parameters shown are the result of the "gold standard" modeling, which is multipixel modeling for each galaxy using the M160 PSF and data from all cameras.

The first row shows the distributions of $M_{\rm d}$ (left column) and $L_{\rm d}$ (right column) for the KF62 galaxies. The second row shows the distributions of $\langle U \rangle$ (left column) and $q_{\rm PAH}$ (right column), and the bottom row shows the distributions of $\langle f_{\rm PDR} \rangle$

(left column) and $\langle \alpha \rangle$ (right column). In these histograms, the dust masses $M_{\rm d}$ and $\langle U \rangle$ are renormalized, as discussed in Section 5.2.

Figure 6 illustrates the large region in the model parameter space spanned by the KINGFISH sample, allowing us to probe the dust properties in a variety of ISM conditions. The total dust mass and dust luminosity found in the galaxies span almost four decades: $10^{4.5} \leqslant M_{\rm d}/M_{\odot} \leqslant 10^{8.0}$ and $10^{7.5} \leqslant L_{\rm d}/L_{\odot} \leqslant 10^{11.1}$, from the blue dwarf NGC 2915 ($L_{\rm d} = 3.3 \times 10^7 L_{\odot}$) to the luminous starburst galaxy NGC 2146 ($L_{\rm d} = 1.4 \times 10^{11} L_{\odot}$).

The mean value of the starlight heating parameter $U_{\rm min}$ also presents wide variations across the galaxy sample. Here, $\langle U_{\rm min} \rangle$ spans the range $0.1 \leqslant \langle U_{\rm min} \rangle \leqslant 8.5$ (these values of $U_{\rm min}$ are for the DL07 model without renormalization). The PAH mass fraction $q_{\rm PAH}$ also shows wide variation, from 0.005 to 0.045, with median $q_{\rm PAH} = 0.027$. The mean fraction of the dust luminosity coming from dust heated by high-intensity radiation fields, $\langle f_{\rm PDR} \rangle$, typically ranges from 0.05 to 0.20.

There are four KINGFISH galaxies where the fitted DL07 dust models have very high values of $\langle f_{\rm PDR} \rangle > 0.30$: NGC 1316 = Fornax A (SAB0), NGC 3049 (SBab), NGC 3265 (E), NGC 5408 (IBm), and the "extra" galaxy NGC 1510 (SA0). NGC 1316 = Fornax A has a central active galactic nucleus (AGN)/LINER spectrum, NGC 3265 has an emission-line nuclear region (Dellenbusch et al. 2008), NGC 1510 hosts a strong central starburst, and NGC 3049 and NGC 5408 are often classified as starburst galaxies. Thus, the high $\langle f_{\rm PDR} \rangle$ values for these galaxies may be indicative of concentrated star formation or nuclear activity.

Finally, the mean power-law exponent $\langle \alpha \rangle$ spans $1.5 \leqslant \langle \alpha \rangle \leqslant 2.5$. Allowing α to vary does improve the quality of the fit to the observed SED, but in most cases the fit quality does not suffer greatly if α is held fixed at $\alpha = 2$, reducing the number of free parameters. Recall that $\alpha = 2$ corresponds to equal amounts of dust power per logarithmic interval in starlight intensity U.

Compared with the "gold standard," modeling using PSFs smaller than M160, and hence having fewer cameras available, can affect the derived dust and starlight parameters. As the PSF shrinks, data are provided by fewer cameras, the wavelength coverage shrinks as the PSF is reduced below S500, and the photometry becomes noisier because it is being smoothed over smaller PSFs. Above we have compared two cases: modeling with the M160 PSF versus modeling with the S250 PSF, but additional comparisons are made in Appendix D. Here we simply note some trends. In general, $M_{\rm d}$ is fairly robust: the S250 modeling typically overestimates $M_{\rm d}$ by $\sim 25\%$, but agrees with the "gold standard" to within a factor of 1.5 for over 75% of the galaxies (see Figure 19). The $q_{\rm PAH}$ estimates are also robust, with typical changes of less than 15%. Longer wavelength coverage (SPIRE350 and SPIRE500) gives more reliable dust estimates. Even comparing resolved and global modeling of dust properties can give different results; although most parameters are consistent to within a few percent, global modeling can underestimate $M_{\rm d}$ by as much as 35%, as for NGC 1481 and NGC 3077 (see Figure 21). This is because the resolved models can have "cold" regions with low $U_{\rm min}$ values that contribute to dust mass estimates but do not emerge in the global results (e.g., Galliano et al. 2011; Galametz et al. 2012).

---

[39] This is a rough estimate, assuming ~ 1 $M_{\odot}$ stars each lose ~ 0.5 $M_{\odot}$ of envelope before becoming white dwarfs and that $\sim 1\%$ of the envelope mass consists of dust.
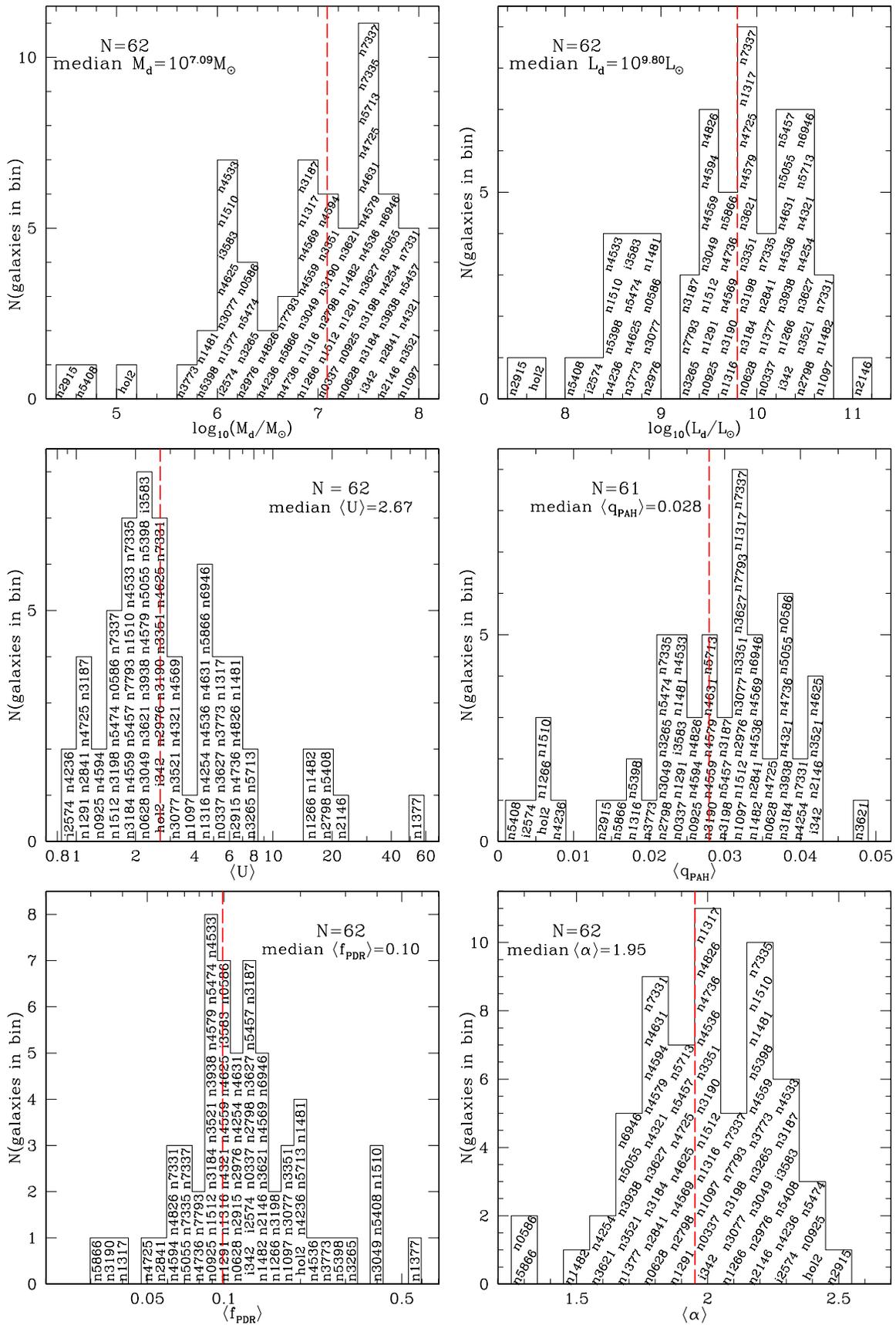
Figure 6. Distributions of dust and starlight parameters for the KF62 sample. NGC 1377 is omitted from the $q_{\rm PAH}$ histogram (see the text). $M_{\rm d}$ and $\langle U \rangle$ are renormalized values.
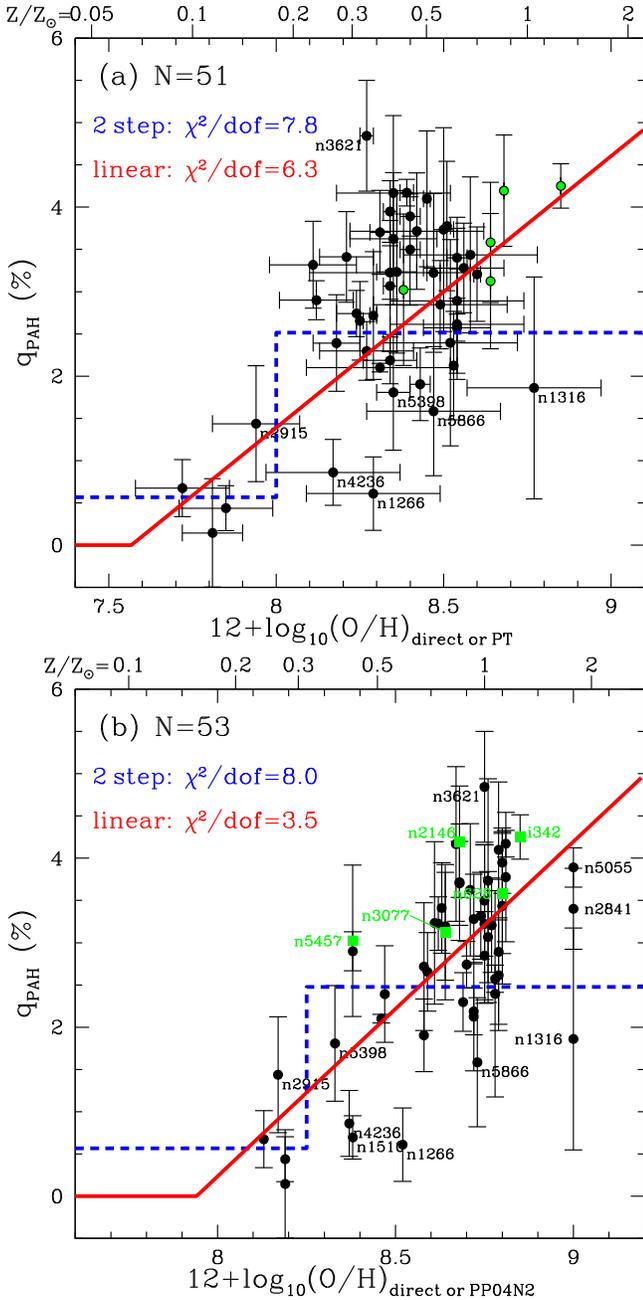
Figure 7. (a) PAH abundance parameter q_{PAH} versus oxygen abundance (direct or PT) for 51 galaxies (see text). Two q_{PAH} estimators are shown: one is a step function, and the other is linear above a threshold value. Selected galaxies have been labeled. The step function and linear estimators have similar $\chi^2/\mathrm{dof} = 7.8$ and 6.3. (b) Same but for PP04N2 oxygen abundance, now for 53 galaxies (PP04N2 oxygen abundances are available for NGC 1512 and NGC3077). The five galaxies where O/H has been determined by "direct" methods are shown in green. The linear fit of q_{PAH} versus $12 + \log_{10}(\mathrm{O/H})$ (Equation (18)) gives an improved fit, with $\chi^2/\mathrm{dof} = 3.5$ and a threshold $(\mathrm{O/H}) \approx 0.15(\mathrm{O/H})_\odot$.

6.5. Dependence of Global PAH Fraction on Metallicity

Figure 7(a) shows q_{PAH} versus $\log(\mathrm{O/H})$ for 51 galaxies using direct determinations of (O/H) where available (five galaxies), and PT estimates otherwise. Nineteen galaxies have been omitted: eight dust nondetections have been excluded, NGC 1377 (a dense starburst with a core that is optically thick at 8 μm; see Section 6.3.2), plus 10 galaxies for which we have no PT estimate for O/H. The oxygen abundance in these

galaxies ranges over more than a factor of 10, and q_{PAH} shows a clear tendency to increase with increasing O/H, although there is considerable scatter. The observed behavior can be approximated by a step function, with an abrupt increase in q_{PAH} when $12 + \log_{10}(\mathrm{O/H})_{PT}$ rises above ~ 8.0. Alternatively, q_{PAH} can be approximated by a linear dependence on $\log(\mathrm{O/H})$. The best-fit step function and linear function are shown in Figure 7(a), with χ^2 per degree of freedom of 8.0 and 6.6, respectively.

Figure 7(b) shows q_{PAH} versus the PP04N2 estimate for metallicity. Again, we show both step functions and a linear dependence on $\log_{10}(\mathrm{O/H})$. In this case, the function linear in $\log(\mathrm{O/H})_{PP04N2}$ gives a much better fit to the data:

$$q_{PAH} \approx 0.0396[(12 + \log_{10}(\mathrm{O/H})_{PP04N2}) - 7.94] \qquad (18)$$

(for $12 + \log_{10}(\mathrm{O/H})_{PP04N2} > 7.94$). This fit, with $53 - 2 = 51$ degrees of freedom (dof), has $\chi^2/\mathrm{dof} = 3.5$: the PP04N2 metallicity is evidently a *much* better predictor of q_{PAH} than is the PT metallicity.[40] This strongly suggests that the PP04N2 metallicities are more tightly related to the properties of the ISM—including metallicity—that regulate the balance between PAH formation and destruction.

The observed tendency for q_{PAH} to increase with increasing metallicity is consistent with many previous studies. The connection between PAH abundance and metallicity was first noted in ground-based spectroscopy by Roche et al. (1991) and further investigated using *Infrared Space Observatory* data (Boselli et al. 1998; Madden 2000; Sturm et al. 2000). Hunt et al. (2005, 2010) found PAH emission to be weak in low-metallicity, blue compact dwarf galaxies. Engelbracht et al. (2005) used IRAC and MIPS24 photometry to show that there was an abrupt drop in the 8 μm/24 μm flux ratio when the metallicity dropped below 8.2, interpreting this as being due to a sharp drop in the abundance of PAHs that normally dominate the emission at 8 μm. Draine et al. (2007) estimated q_{PAH} for 61 SINGS galaxies, using the DL07 model with IRAC and MIPS photometry, and found a similar result: a sharp increase in q_{PAH} when $12 + \log_{10}(\mathrm{O/H})_{PT}$ rises above ~ 8.2.

Nevertheless, there are outliers in Figure 7(b). The SB0 galaxy NGC 1266 has $q_{PAH} = 0.70\%$, unusually low for a galaxy with $12 + \log_{10}(\mathrm{O/H})_{PP04N2} = 8.51$. The *Spitzer* and *Herschel* photometry of NGC 1266 (see Figure 17.8) appears to be reliable. Because the optical spectrum of NGC 1266 is AGN-dominated, the metallicity is not based on emission lines and is therefore highly uncertain. Moustakas et al. (2010) estimated the metallicity from an assumed luminosity–metallicity relation. The resulting $12 + \log_{10}(\mathrm{O/H})_{PP04N2} = 8.51$ is consistent with the stellar mass–metallicity relation (Andrews & Martini 2013). Perhaps the PAH abundance in this galaxy has been suppressed by phenomena associated with the AGN that is driving a molecular outflow characterized by shocked gas (Alatalo et al. 2011, 2015; Pellegrini et al. 2013).

The SAB0 galaxy NGC 1316 = Fornax A is another outlier. The dust emission is weak relative to the starlight, making the q_{PAH} estimate uncertain. In addition, the starlight heating the dust is likely from an old population, similar to the bulge of M31, and our estimate of q_{PAH} (based on single-photon heating by starlight assumed to have the solar neighborhood spectrum)

---

[40] For some galaxies, we use "direct" metallicities rather than the PT or PP04N2 weak-line estimates, but χ^2 is dominated by the 51 galaxies where we use PP04N2 instead of the PT metallicity estimate.

would then be biased low. The estimate for q_{PAH} in the center of M31 increases by almost a factor of two when calculated using the correct starlight spectrum (Draine et al. 2014), and a similar correction might bring q_{PAH} for NGC 1316 closer to the general trend in Figure 7(b). In addition, the high metallicity estimated for NGC 1316 may be influenced by the AGN contribution to the emission line spectrum.

In Figure 7 it is striking that the bulk of the galaxies with $12 + \log_{10}(O/H)_{PP04N2} > 8.3$ have q_{PAH} in the 1.5%–5% range. Evidently the physical processes responsible for formation and destruction of PAHs in normal star-forming galaxies tend to maintain PAH abundances near 3% provided that the metallicity $Z/Z_{\odot} \gtrsim 0.3$. From Equation (18) it appears that there is a threshold metallicity for PAH formation: $q_{PAH} \approx 0$ for $12 + \log_{10}(O/H)_{PP04N2} \lesssim 7.94$, or $Z/Z_{\odot} \lesssim 0.15$.

6.6. Dependence of Global Dust-to-gas Ratio on Metallicity

6.6.1. Theoretical Expectations

The abundance of dust in the ISM is the result of competition between processes that form dust (dust formation in stellar outflows and dust growth in the ISM) and processes that return material to the gas phase (e.g., sputtering in hot gas and vaporization in high-speed grain–grain collisions). In the Milky Way and other star-forming galaxies with near-solar metallicity, accretion of atoms onto grains is rapid in the cool, dense phases of the ISM, and the balance between grain growth and grain destruction maintains a large fraction of the refractory elements in grains. Most of the dust in the Milky Way must have been grown in the ISM; there is simply no other way to understand the observed extreme depletions of elements like Si, Al, Ca, Ti, and Fe in the diffuse ISM (see, e.g., Draine 1990; Weingartner & Draine 1999; Draine 2009).

The black dashed line in Figure 8(a) shows the expected dependence of M_d/M_H on O/H if all galaxies had heavy element abundances proportional to solar abundances and the same depletion pattern as measured in the well-studied cloud toward the nearby star ζOph; in this cloud, the refractory elements (e.g., Mg, Si, Fe) are almost completely incorporated into grains, and we infer a dust/H mass ratio of 0.0099 (see Table 23.1 of Draine 2011). For this scenario, we then expect

$$\left(\frac{M_d}{M_H}\right) = 0.0099\left(\frac{Z}{Z_{\odot}}\right), \qquad (19)$$

where we take $Z/Z_{\odot} = 1$ for $12 + \log_{10}(O/H) = 8.72$ (Asplund et al. 2009, corrected for diffusion). However, in the overall ISM, M_d/M_H will fall below this limiting value, because of dust destruction processes.

A simple toy model can illustrate the competition between formation and destruction processes (similar models have been discussed by, e.g., Edmunds 2001; Mattsson et al. 2012; Asano et al. 2013).

Let Z_m be the fraction of the ISM mass in "refractory" elements ($Z_m \approx 0.007 \times (Z/Z_{\odot}) = 0.007 \times 10^{(12+\log_{10}(O/H)-8.75)}$) and Z_d be the fraction of the ISM mass in dust grains made of these refractory elements ($M_d/M_H = 1.4Z_d$). Clearly $Z_d < Z_m$, since some of the refractory elements are in the gas phase.

Destruction and grain growth in the ISM both contribute to the rate of change of Z_d. We also include a term representing injection of solid grains into the ISM from stellar sources (AGB stars, supernovae, and so on). The rate of change of Z_d is
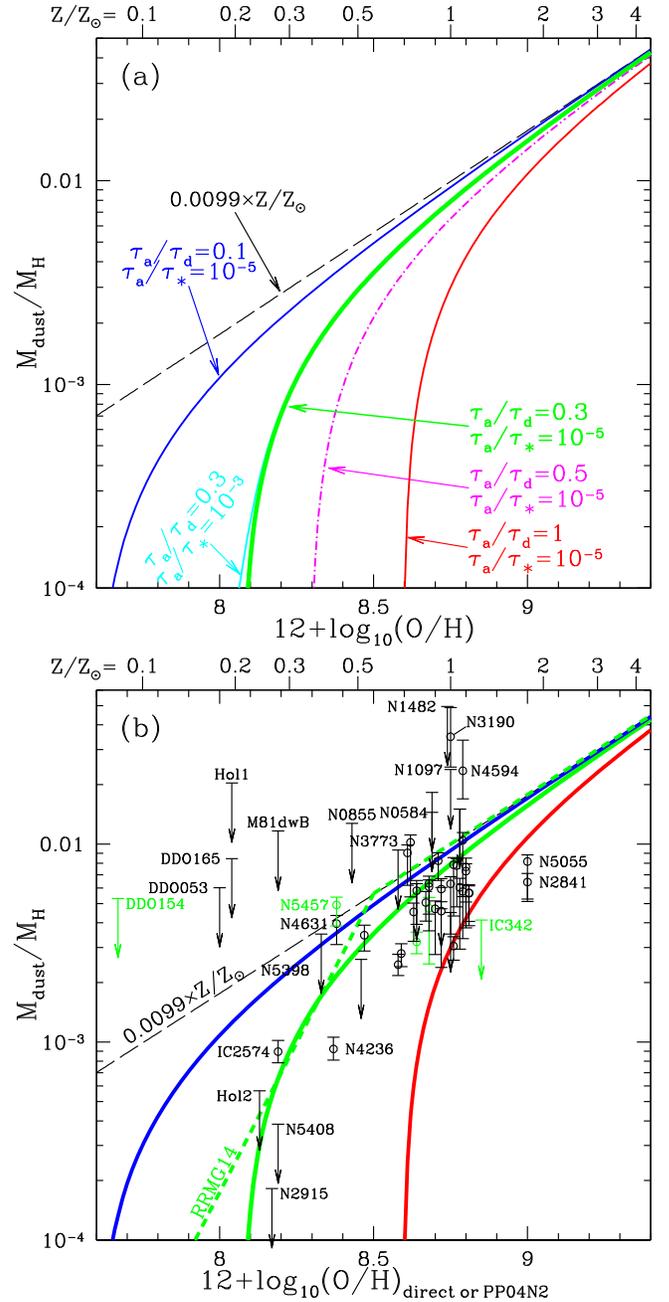

Figure 8. (a) Dust/H mass ratio versus metallicity for the toy model (Equation (21)) for selected values of τ_a/τ_d and $\tau_a/\tau_{\star}$ (see text). (b) Measured M_d/M_H (for the M160-resolution galaxy mask) versus $12 + \log_{10}(O/H)$ (see text) for 57 KINGFISH galaxies. Selected galaxies have been labeled. Arrows indicate upper limits for the 16 galaxies lacking CO data. The green curve is Equation (21) for $\tau_a/\tau_d = 0.3$ and $\tau_a/\tau_{\star} \lesssim 10^{-3}$; the blue and red curves are for $\tau_a/\tau_d = 0.1$ and 1. The green dashed line is the broken power-law fit from Rémy-Ruyer et al. (2014).

given by

$$\dot{Z}_d = -\frac{Z_d}{\tau_d} + \frac{(Z_d/0.007)}{\tau_a}(Z_m - Z_d) + \frac{Z_m}{\tau_{\star}}. \qquad (20)$$

The first term $-Z_d/\tau_d$ is the rate of dust destruction: τ_d is the lifetime of solid material in the ISM against destructive processes that return material to the gas phase. The destruction rate τ_d^{-1} is a mass-weighted average over the dust in the

multiphase ISM. Studies of the effects of supernova blast waves in the local ISM suggest timescales $\tau_d \approx 4 \times 10^8$ yr (see discussion in, e.g., Draine 2009). Realistic estimation of τ_d requires a detailed, dynamic multiphase model of the ISM (e.g., Zhukovska et al. 2016). The appropriate value of τ_d will obviously vary with galactocentric radius within a galaxy and from galaxy to galaxy.

The term in Equation (20) representing grain growth is proportional to $Z_d(Z_m - Z_d)$ because it depends on grain surface area ($\propto Z_d$, for a fixed distribution of grain sizes) and on the gas-phase abundance of condensible elements ($\propto (Z_m - Z_d)$). Here, $(Z_d/0.007)\tau_a^{-1}$ is the probability per unit time that a refractory atom in the gas phase will collide with and stick to a grain.

The last term, $Z_m/\tau_\star$, represents injection of dust into the ISM from stellar sources, such as cool AGB stars, planetary nebulae, and core-collapse supernovae. This term will obviously depend on the stellar populations. Here, for illustration, we take the injection rate to be proportional to the metallicity Z_m. For the galaxies of interest here, this injection term is small compared to the other terms in Equation (20), and the precise form adopted in Equation (20) is not critical.

If the shortest of the timescales $\{\tau_a, \tau_d\}$ is short compared to the $\sim 10^9$ yr timescale for galactic chemical evolution, and $\tau_\star \gg \{\tau_a, \tau_d\}$, we can neglect the time dependence of the metallicity Z_m. The toy model will approach a quasi-steady-state solution with $\dot{Z}_d \approx 0$:

$$Z_d = \frac{1}{2}\left(Z_m - \frac{0.007}{\tau_d/\tau_a}\right) + \frac{1}{2}\left[\left(Z_m - \frac{0.007}{\tau_d/\tau_a}\right)^2 + \frac{0.028}{\tau_\star/\tau_a}Z_m\right]^{1/2}.$$
(21)

This solution for Z_d depends only on Z_m and on ratios of timescales, τ_a/τ_d and $\tau_\star/\tau_d$. Equation (21) for Z_d is plotted in Figure 8(a) for several choices of the ratios τ_a/τ_d and $\tau_a/\tau_\star$. Note that for all of our examples we take $\tau_\star^{-1} \ll \tau_a^{-1}$: dust formation in stellar outflows is secondary to dust growth in the ISM (i.e., only a small fraction of interstellar dust is "stardust"). For large values of Z_m, all models approach the upper limit $Z_d/Z_m = 1$ (long-dashed line in Figure 8(b)).

Models of interest have $\tau_a < \tau_d$, so that for near-solar abundances, accretion is faster than destruction, and a solar-metallicity ISM can maintain a large fraction of the refractory elements in dust (i.e., $Z_d/Z_m \gtrsim 0.5$). However, for sufficiently low O/H, accretion rates become slow, resulting in low values of Z_d/Z_m.

6.6.2. Observations

Using dust mass estimates based on modeling the infrared emission, radial variations in DGRs were found for galaxies in the SINGS sample (Muñoz-Mateos et al. 2009) and for M101 (Vílchez et al. 2019). The dust-to-metals ratio was approximately constant for KK04 metallicities $12 + \log_{10}(O/H)_{KK} \geqslant 9.0$, but for $12 + \log_{10}(O/H)_{KK} \leqslant 8.8$ the dust-to-metals ratio appeared to decline with decreasing metallicity. Chiang et al. (2018) found variations in the dust-to-metals ratio in M101, which they related to variations in both metallicity and H_2 fraction. De Cia et al. (2016) found similar behavior in a sample that included 55 damped Lyα systems (DLAs), where dust abundances were inferred from depletions of Si and metallicities from [Zn/Fe]. It

appears that as metallicity decreases below a certain threshold (e.g., $12 + \log_{10}(O/H)_{KK}$), an increasing fraction of refractory elements (Mg, Si, Fe, ...) remains in the gas phase.

DGRs for the KF57 sample (see Table 1) are plotted against O/H in Figure 8(b), with dust masses estimated from our model, gas masses taken from Table 10, and the PP04N2 estimate for O/H. Fourteen galaxies have detections of both dust and H I, but were either not observed or not detected in CO, resulting in DGR upper limits. An additional seven galaxies were detected in H I but not in dust, resulting in DGR upper limits.

Figure 8(b) shows a clear dependence of dust/gas ratio on metallicity. With some exceptions, the observed dust/H mass ratios for the KF57 sample are in broad agreement with the toy model (Equation (19)) for $0.1 \lesssim \tau_a/\tau_d \lesssim 1$, with $\tau_a/\tau_d = 0.3$ (green curve in Figure 8(b)) providing a reasonable fit to the main trend in M_d/M_H versus O/H.

We do not expect all galaxies to be characterized by a single value of τ_a/τ_d. Allowing for reasonable variation of τ_a/τ_d from galaxy to galaxy (ranging from $\tau_a/\tau_d = 1$ for the red curve to $\tau_a/\tau_d = 0.1$ for the blue curve) can accommodate almost all of the measured values. However, there are some notable exceptions:

1. NGC 1482 (type SA0): This galaxy with near-solar O/H has a measured dust/H mass ratio several times larger than the "upper limit" $0.0099(Z/Z_\odot)$ (although NGC 1482 is missing CO measurements). It is notable that the ISM appears to have been subject to unusual activity. NGC 1482 shows evidence of a galactic-scale "superwind": the X-ray morphology shows a striking "hourglass" shape emerging from the plane of the disk (Strickland et al. 2004; Vagshette et al. 2012). Interestingly, this galaxy is completely missing H I in its central region, with atomic gas only found in two blobs $\sim$2 kpc distant from its center, roughly at the confines of the X-ray emission (Hota & Saikia 2005). CO observations of NGC 1482 are needed. If NGC 1482 were found to have $M(H_2) + M(H II) \approx 1.3 \times 10^9 M_\odot$, the M_d/M_H ratio would be normal for its metallicity.

2. NGC 4594 (M104 "Sombrero," type SAb) also has near-solar O/H, but a dust/H mass ratio several times larger than the expected upper limit $0.0099(Z/Z_\odot)$. NGC 4594 has diffuse X-ray emission, suggesting the presence of a galactic-scale outflow (Li et al. 2011). Li et al. (2011) estimate the hot gas to have a temperature $T \approx 6 \times 10^6$ K and total mass $M_{hot} \approx 2.9 \times 10^8 M_\odot$. Adding this to the Bajaja et al. (1984) value for H I and the H_2 mass estimated with a standard X_{CO} factor, we find $M_H = 6.0 \times 10^8 M_\odot$ and $M_d/M_H = 0.023$, about a factor of 2.5 above the ratio expected for metallicity $Z/Z_\odot \approx 1$. The gas in the hot phase, with a density $n_H \approx 0.1$ cm^{-3}, has a cooling time $\tau \approx 5 \times 10^7$ yr (Li et al. 2011). Some of the hot gas may have cooled down to $\sim 10^4$ K, perhaps making an additional contribution to the total gas mass present in NGC 4594. We suggest that NGC 4594 may contain a substantial mass of diffuse H II at $\sim 10^4$ K that has not yet been detected.

Gravity, radiation pressure, and inertia can all lead to velocity differences between gas and dust, allowing the two to separate. However, because dust is generally well coupled to the gas by both gas drag and the Lorentz force on charged grains, gas–grain "slip" velocities are generally small (e.g., Weingartner & Draine 2001b), and scenarios where gas is removed but dust is left behind are not viable unless the gas flows are slow enough that the small

Table 10
Gas Masses for M160-resolution Galaxy Mask and Dust/Gas Ratio

Galaxy	$M(\mathrm{H\,I})^{[a]}$ $(10^9 M_\odot)$	$M(\mathrm{H_2})^{[a]}$ $(10^9 M_\odot)$	$M_{\mathrm{dust}}^{[b]}$ $(10^6 M_\odot)$	$M_{\mathrm{dust}}/M_{\mathrm{H}}^{[a]}$
DDO 053	0.0382 ± 0.0038	...	<0.21	<0.0060
DDO 154	0.128 ± 0.013	<0.0010	<0.61	<0.0053
DDO 165	0.069 ± 0.007	...	<0.52	<0.0085
Ho I	0.0366 ± 0.0037	<0.00077	<0.67	<0.020
Ho II	0.232 ± 0.023	<0.0016	0.112 ± 0.006	<0.00057
IC 342	14.3 ± 4.3	...	41.28 ± 0.21	<0.0041
IC 2574	0.87 ± 0.09	0.0084 ± 0.0014	0.782 ± 0.019	0.00089 ± 0.00012
M81dwB	0.0079 ± 0.0008	<0.00057	<0.081	<0.012
NGC 0337	4.13 ± 0.41	0.389 ± 0.042	15.67 ± 0.32	0.0035 ± 0.0005
NGC 0584	0.157 ± 0.047	...	<1.59	<0.014
NGC 0628	2.30 ± 0.23	1.38 ± 0.14	21.44 ± 0.08	0.0058 ± 0.0012
NGC 0855	0.115 ± 0.034	...	<1.02	<0.013
NGC 0925	4.45 ± 0.45	0.256 ± 0.027	13.19 ± 0.17	0.0028 ± 0.0004
NGC 1097	4.4 ± 1.3	...	73.3 ± 0.7	<0.024
NGC 1266	>0.0095	...	12.14 ± 0.29	<1.31
NGC 1291	1.32 ± 0.39	...	13.63 ± 0.23	<0.015
NGC 1482	0.67 ± 0.20	...	22.5 ± 0.6	<0.050
NGC 1512	2.9 ± 0.9	...	12.10 ± 0.13	<0.0060
NGC 2146	3.3 ± 1.0	8.5 ± 0.9	55.9 ± 0.6	0.0047 ± 0.0014
NGC 2798	0.96 ± 0.10	2.52 ± 0.25	15.95 ± 0.44	0.0046 ± 0.0014
NGC 2841	6.6 ± 0.7	0.89 ± 0.09	48.42 ± 0.30	0.0064 ± 0.0009
NGC 2915	0.35 ± 0.11	...	0.039 ± 0.006	<0.00018
NGC 2976	0.142 ± 0.014	0.073 ± 0.007	1.948 ± 0.031	0.0090 ± 0.0019
NGC 3049	1.01 ± 0.10	0.144 ± 0.018	6.84 ± 0.21	0.0059 ± 0.0010
NGC 3077	0.429 ± 0.043	0.0161 ± 0.0017	1.425 ± 0.018	0.0032 ± 0.0004
NGC 3184	3.68 ± 0.37	1.98 ± 0.20	31.91 ± 0.27	0.0056 ± 0.0011
NGC 3190	0.46 ± 0.14	0.058 ± 0.013	18.2 ± 0.5	0.035 ± 0.012
NGC 3198	8.1 ± 0.8	0.62 ± 0.06	26.71 ± 0.30	0.0031 ± 0.0004
NGC 3265	0.17 ± 0.05	...	2.00 ± 0.24	<0.018
NGC 3351	1.08 ± 0.11	1.02 ± 0.10	16.34 ± 0.15	0.0078 ± 0.0018
NGC 3521	10.4 ± 1.0	4.18 ± 0.42	82.6 ± 0.9	0.0057 ± 0.0011
NGC 3621	5.2 ± 0.5	...	20.75 ± 0.27	<0.0045
NGC 3627	1.12 ± 0.11	3.02 ± 0.30	42.22 ± 0.20	0.0102 ± 0.0029
NGC 3773	0.109 ± 0.033	...	0.689 ± 0.024	<0.0093
NGC 3938	5.1 ± 0.5	2.51 ± 0.25	48.42 ± 0.32	0.0063 ± 0.0012
NGC 4236	1.91 ± 0.19	0.0028 ± 0.0010	1.77 ± 0.06	0.00092 ± 0.00012
NGC 4254	4.93 ± 0.49	7.2 ± 0.7	69.99 ± 0.42	0.0058 ± 0.0015
NGC 4321	3.38 ± 0.34	6.9 ± 0.7	81.16 ± 0.39	0.0079 ± 0.0021
NGC 4536	4.62 ± 0.46	1.86 ± 0.19	29.5 ± 0.6	0.0045 ± 0.0009
NGC 4559	3.16 ± 0.32	0.051 ± 0.006	7.90 ± 0.14	0.0025 ± 0.0003
NGC 4569	0.248 ± 0.025	1.30 ± 0.13	11.88 ± 0.16	0.0077 ± 0.0024
NGC 4579	0.73 ± 0.07	2.42 ± 0.24	32.95 ± 0.11	0.0105 ± 0.0030
NGC 4594	0.20 ± 0.06	0.043 ± 0.007	12.57 ± 0.11	$0.023 \pm 0.008^{[c]}$
NGC 4625	0.241 ± 0.024	0.0285 ± 0.0039	1.365 ± 0.046	0.0051 ± 0.0008
NGC 4631	7.7 ± 0.8	1.62 ± 0.16	36.84 ± 0.30	0.0040 ± 0.0006
NGC 4725	3.51 ± 0.35	0.67 ± 0.07	34.40 ± 0.20	0.0082 ± 0.0013
NGC 4736	0.50 ± 0.05	0.59 ± 0.06	6.676 ± 0.034	0.0061 ± 0.0015
NGC 4826	0.112 ± 0.011	0.66 ± 0.07	4.66 ± 0.06	0.0060 ± 0.0019
NGC 5055	3.70 ± 0.37	3.35 ± 0.33	57.54 ± 0.27	0.0082 ± 0.0018
NGC 5398	0.26 ± 0.08	...	0.593 ± 0.038	<0.0035
NGC 5408	0.24 ± 0.07	...	0.0603 ± 0.0049	<0.00039
NGC 5457	11.5 ± 1.1	2.58 ± 0.26	69.15 ± 0.17	0.0049 ± 0.0008
NGC 5474	0.62 ± 0.06	<0.0049	1.429 ± 0.035	<0.0026
NGC 5713	3.24 ± 0.32	4.00 ± 0.40	34.1 ± 0.6	0.0047 ± 0.0012
NGC 6946	3.52 ± 0.35	6.6 ± 0.7	63.46 ± 0.30	0.0063 ± 0.0017
NGC 7331	10.7 ± 1.1	5.2 ± 0.5	$116. \pm 1.$	0.0073 ± 0.0014
NGC 7793	0.99 ± 0.10	...	5.75 ± 0.05	<0.0065

Notes.
[a] He is not included.
[b] Renormalized as described in Section 5.2.
[c] M_{H} includes $M = 2.9 \times 10^8 M_\odot$ of hot gas (Li et al. 2011).

gas–grain "slip" velocities suffice to prevent the dust grains from leaving the galaxy. Even if gas is stripped or lost in an outflow, we expect the metallicity in the remaining gas (and therefore the upper bound Equation (19) on the dust/mass ratio) to be unaffected. If NGC 1482 and NGC 4594 truly have high dust/gas ratios, then this would appear to require a mechanism for concentrating the dust in part of the gas and removing the dust-poor gas via an outflow or stripping. Alternatively, perhaps the dust/gas ratio is actually normal, but the dust mass has been overestimated because the dust material for some reason has a far-infrared/submillimeter opacity that is significantly larger than found in normal star-forming galaxies. The elevated dust/gas mass ratios in NGC 1482 and NGC 4594 require further study.

3. NGC 2841 (Type SAb) and NGC 5055 (M63, Type SAbc): These two galaxies have much *lower* dust/gas ratios than would be expected given their high estimated metallicities ($12 + \log_{10}(O/H)_{PP04N2} = 9.31$; $Z/Z_\odot = 3.6$). The photometry for these galaxies is reliable, and the models reproduce the SED out to 500 μm. However, it seems likely that the metallicities given in Table 2 are overestimated. Moustakas et al. (2010) with KK04 found that NGC 2841 and NGC 5055 have $12 + \log_{10}(O/H)$ significantly greater than 9.0, $\sim$0.2 dex higher than the values found for the central regions in the same galaxies by Pilyugin et al. (2014). Pilyugin et al. (2014) also deduce strong metallicity gradients in these two galaxies, implying that at 0.5 R_{25}, the characteristic $12 + \log_{10}(O/H) \sim 8.6$. Such metallicities, better representing the average over the galactic disk, would be consistent with the observed dust/gas ratios for these two galaxies.

In Figure 8(b) we also show the broken power-law empirical trend found by Rémy-Ruyer et al. (2014), with $M_d/M_H \propto (O/H)$ for O/H above a critical value,[41] but with $M_d/M_H \propto (O/H)^{3.02}$ for lower values of (O/H). This empirical result is seen to fall close to our toy model with $\tau_a/\tau_d = 0.3$.

6.7. Resolved Trends of DL07 Parameters

Using data at M160 resolution, the synergy of *Herschel* and *Spitzer* for the KINGFISH sample enables an assessment of dust properties on kiloparsec scales in nearby galaxies (the FWHM of the M160 PSF, 38″8, corresponds to 1.86 kpc at the median KINGFISH sample distance of 9.9 Mpc). The number of M160 18″ × 18″ pixels in each galaxy ranges from 20 for the smallest galaxies (M81 dwB, NGC 584) to >4000 pixels for the largest ones (NGC 5457 = M101 and IC 342); the resolved sample as a whole, including the nine "extra" galaxies, comprises >32,000 pixels with well-defined dust parameters and photometry.

Figure 9 shows how the starlight intensity parameters $U_{min,DL07}$ and $\overline{U}_{DL07}$ are distributed over the $\sim$32,000 galaxy mask pixels (i.e., $\Sigma_{Ld} > \Sigma_{Ld,min}$) where we are able to estimate the dust and starlight parameters. Half of the pixels have $\overline{U} < 1$, and half of the pixels have $U_{min} < 1$. The $\overline{U}$ distribution for the KF62 sample (Figure 9) is similar to that for Local Group galaxies (Utomo et al. 2019).

Figure 9. Distributions of U_{min} and $\overline{U}$ (U_{bar}) for all galaxies. U_{min} and $\overline{U}$ are the renormalized values (see Equations (13)–(16)). Both distributions are fairly broad; for a given pixel, $\overline{U}-U_{min}$ may be smaller than or comparable to U_{min} given that f_{PDR} is usually modest. Thus, it is not surprising that the two peaks are similar.

The distributions of dust luminosity densities Σ_{Ld} and dust mass densities Σ_{Md} are displayed in Figure 10. The Σ_{Ld} distribution peaks toward fainter Σ_{Ld}, increasing down to the lowest values of $\Sigma_{Ld} \approx 10^6 L_\odot$ kpc^{-2} allowed by the luminosity surface density cutoff $\Sigma_{Ld,min}$ defining the "galaxy mask" for each galaxy.[42] While the pixel histogram peaks at faint $\Sigma_{Ld} \approx 10^6 L_\odot$ kpc^{-2}, the infrared luminosity is dominated by the bright pixels with $\Sigma_{Ld} \approx 10^8 L_\odot$ kpc^{-2}. The distribution of dust surface densities Σ_{Md} peaks near $10^5 M_\odot$ kpc^{-2}, which corresponds to $A_V \approx 0.7$ mag, and $\sim$90% of the dust mass is contributed by pixels with $\Sigma_{Md} \gtrsim 10^{4.75} M_\odot$ kpc^{-2}, or $A_V \gtrsim 0.4$ mag. The distribution of the light-to-mass ratio Σ_{Ld}/Σ_{Md} is shown in the right panel of Figure 10. This is of course equivalent to the distribution of $\overline{U}$. The histogram peaks at $L_d/M_d \approx 150 L_\odot/M_\odot$, corresponding to a starlight heating rate parameter $U \approx 1$.

The dust light and mass surface densities that most contribute to the total dust budget are more clearly seen in Figure 11, where we show the cumulative distributions of dust luminosity L_d and dust mass M_d plotted against Σ_{Ld} and Σ_{Md}, respectively.

The vertical dashed lines in Figure 11 show the surface-density thresholds that provide 50% of the total: $\Sigma_{Ld} = 10^{8.2} L_\odot$ kpc^{-2} and $\Sigma_{Md} = 10^{5.1} M_\odot$ kpc^{-2}. Regions with dust light and mass surface densities greater than these values comprise only a small fraction of the total: from Figure 10 we see that 50% of the dust light comes from only $\sim$3% of the (brightest) pixels, and 50% of the total dust mass from $\sim$22% of the (densest) pixels.

In what follows we have applied a limit in dust surface brightness $\Sigma_{Ld} \geqslant 2 \times 10^6 L_\odot$ kpc^{-2}; thus the low-S/N, faint outer regions of the sample galaxies (where estimates of parameters such as Σ_{Md} and q_{PAH} may become unreliable) will not be considered. As seen above, such regions contribute very little to either the light budget or the mass budget of the dust

---

[41] Using PT metallicities, Rémy-Ruyer et al. (2014) estimated this critical metallicity to be $12 + \log_{10}(O/H) = 8.02$. Here we adjust the critical value to 8.42 to allow for the systematic offset of $\sim$0.4 between PT and PP04N2 metallicities at low O/H (see Figure 1).
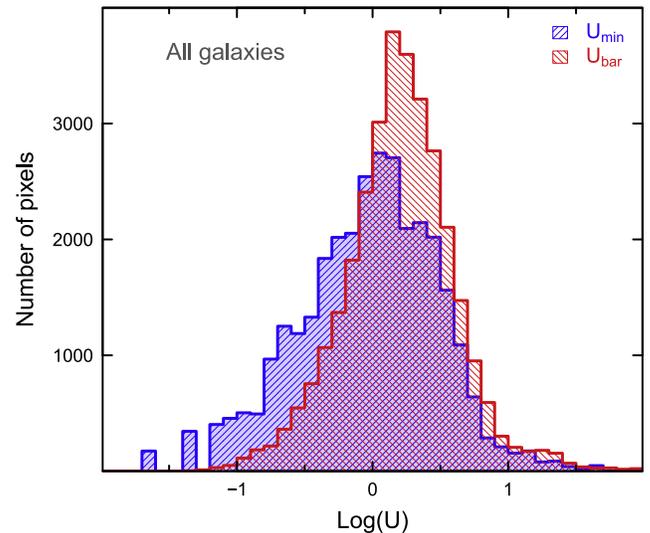
[42] Because our $\Sigma_{Ld,min}$ cutoff varies from galaxy to galaxy, ranging from $10^{5.6} L_\odot$ kpc^{-2} for DDO 165 to $10^{7.4} L_\odot$ kpc^{-2} for NGC 2146, the pixel histogram has a broad peak near $\sim$$10^{6.3} L_\odot$ kpc^{-2}.

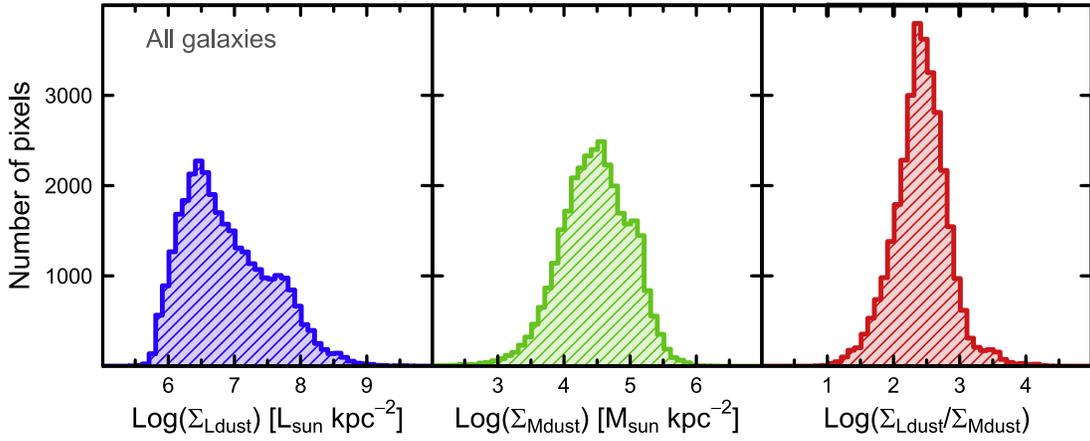**Figure 10.** Distributions of Σ_{Ld} (left panel), Σ_{Md} (middle), and Σ_{Ld}/Σ_{Md} (right) for all galaxies. The cutoffs at low Σ_{Ld} and low Σ_{Md} are due to limitations in sensitivity. The total dust luminosity L_d is contributed mainly by higher surface brightness pixels, with $\Sigma_{Ld} \approx 10^8\, L_\odot$ kpc^{-2}. The total mass is contributed mainly by pixels with $\Sigma_{Md} \approx 10^{5.2} M_\odot$ kpc^{-2}, corresponding to extinction $A_V \approx 1$ mag. The right panel shows that most of the dust has $L_d/M_d \approx 150\, L_\odot/M_\odot$, corresponding to a heating rate $\overline{U} \approx 1$.
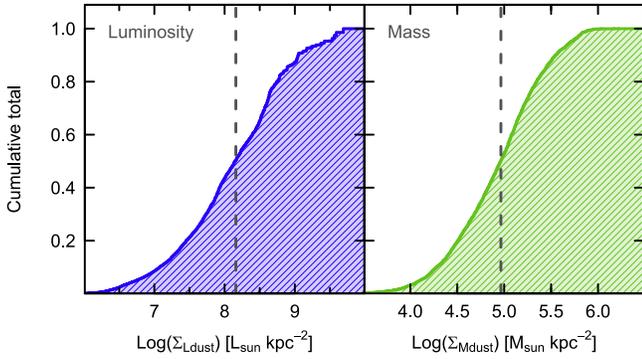

Figure 11. Cumulative distributions of dust luminosity L_d (left panel) and dust mass M_d (right panel) for all galaxies. The vertical dashed lines show the surface brightness Σ_{Ld} and surface density Σ_{Md}, above and below which provides 50% of the total dust luminosity and dust mass, respectively: $\Sigma_{Ld} = 10^{8.2}\, L_\odot$ kpc^{-2} and $\Sigma_{Md} = 10^{5.1} M_\odot$ kpc^{-2}. The regions with $\Sigma_{Ld} > 10^{8.2}\, L_\odot$ kpc^{-2} comprise ~3% of the pixels, and those with $\Sigma_{Md} > 10^{5.1} M_\odot$ kpc^{-2} ~22% of the pixels.

over the sample as a whole. Applying such a cut ensures that the plotted DL07 parameters (and the photometric quantities) will be as accurate as possible, given the constraints of the data; the total number of $18'' \times 18''$ pixels in the sample is reduced to ~25,500.

We now investigate the IR observational signatures associated with dust heating ($U_{\min}$). Figure 12 shows $U_{\min}$ for all galaxies plotted versus MIPS and SPIRE flux density ratios, f_{70}/f_{160}, f_{70}/f_{250}, and f_{160}/f_{500}. Because of the unexplained discrepancies between MIPS and PACS photometry (see Figure 2), we have elected to use only MIPS photometry for f_{70} and f_{160}. The left panel shows that the flux ratio f_{70}/f_{160} is not a very good predictor of $U_{\min}$. This is because when $U_{\min} \lesssim 1$, the 70 μm emission has an appreciable contribution from (1) single-photon heating of small grains and (2) dust in regions with high starlight intensities (assuming $\gamma > 0$, which is almost always the case). The flux ratio f_{160}/f_{250}, shown in the middle panel, ameliorates the potential domination of the emission by small-grain stochastic heating, but the wavelength ratio of the two fluxes is insufficient to reliably sample $U_{\min}$; a small range in flux ratio corresponds to as much as an order of magnitude change in $U_{\min}$. However, the right panel shows that the f_{160}/f_{500} flux ratio correlates quite well with $U_{\min}$ because

the emission at both 160 and 500 μm is dominated by the larger grains heated by starlight intensities near $U_{\min}$. Because 160 μm is not in the Rayleigh–Jeans limit for the grain temperatures in these galaxies, the f_{160}/f_{500} ratio is sensitive to large-grain temperature, and hence to starlight heating rate. The best-fit correlation, obtained with median clipping and a "robust" regression algorithm, effective for minimizing the effects of outliers (R Core Team 2014), is given by

$$\log_{10}(U_{\min}) = (-1.81 \pm 0.01) + (1.95 \pm 0.01)\log_{10}\left(\frac{f_{160}}{f_{500}}\right). \tag{22}$$

This relation predicts $U_{\min}$ to within 0.21 dex (rms) over a range of $U_{\min}$ of more than two orders of magnitude. Because the emission at these wavelengths is dominated completely by large grains, this long-wavelength ratio predicts very well the minimum starlight heating intensity.

The PAH abundance parameter q_{PAH} varies from galaxy to galaxy, as discussed in Section 6.5, where it is apparent that there is a correlation between q_{PAH} and the gas-phase metallicity O/H. Note that q_{PAH} also exhibits significant variations within individual galaxies, as can be seen from the map of q_{PAH} in M101 (see Figure 5), as well as for other well-resolved galaxies (see Figures 17.1–17.62). If q_{PAH} is sensitive to metallicity, then we may expect radial variations within galaxies, with q_{PAH} generally declining with radius. However, our q_{PAH} maps also exhibit substantial azimuthal variations, suggesting that the PAH abundance responds to changes in environmental conditions beyond metallicity alone.

In Figure 13, we explore—using three different proxies for the starlight intensity—whether q_{PAH} is affected by the intensity of the radiation field. The left panel in Figure 13 indicates that q_{PAH} seems to be relatively independent of variations in the f_{70}/f_{160} flux ratio. The f_{70}/f_{160} flux ratio is apparently not uniquely tracing the temperature of the larger grains; as seen in Figure 12 and discussed below, this ratio begins to reflect $U_{\min}$, and thus large-grain temperature, only above a certain $U_{\min}$ threshold ($U_{\min} \gtrsim 0.5$). The middle panel shows little correlation between q_{PAH} and $\nu L_\nu(24\,\mu\text{m})/L_{dust}$, but the right panel shows a stronger trend where q_{PAH} tends to
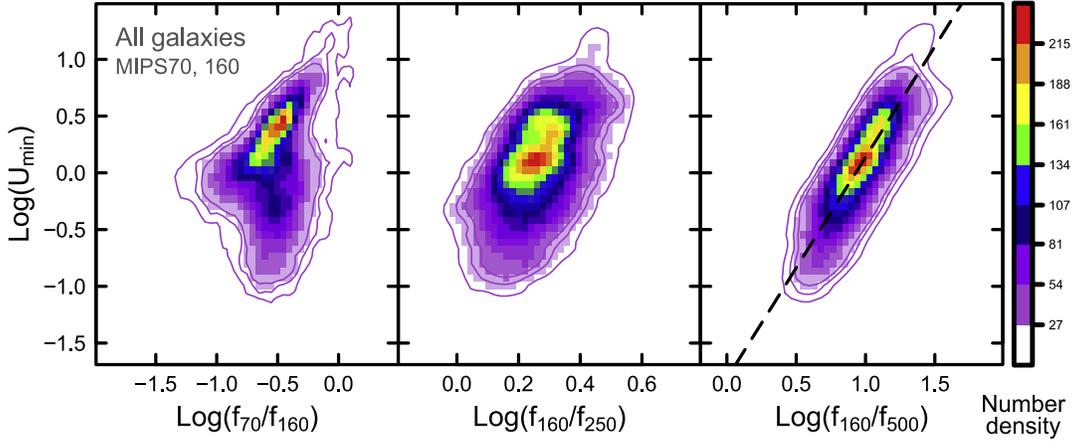
Figure 12. Minimum starlight heating intensity $U_{\min}$ versus f_{70}/f_{160} (left panel), f_{160}/f_{250} (middle), and f_{160}/f_{500} (right) for all galaxies. The 70 and 160 μm flux densities f_{70} and f_{160} are from MIPS only (see text). The color coding corresponds to number density of pixels, as shown by the rightmost color bar. The left panel shows that f_{70}/f_{160} is not a good indicator of $U_{\min}$, because f_{70} is sensitive to both single-photon heating and the emission from dust exposed to starlight intensities $U > U_{\min}$. The middle panel with f_{160}/f_{250} avoids using f_{70}, but the wavelength range is insufficient to adequately sample $U_{\min}$ and a luminosity-weighted dust temperature. Instead, the right panel shows the tight correlation between $U_{\min}$ and f_{160}/f_{500} (the dashed line is Equation (22)), illustrating the close relationship between the minimum heating intensity and the coolest dust.
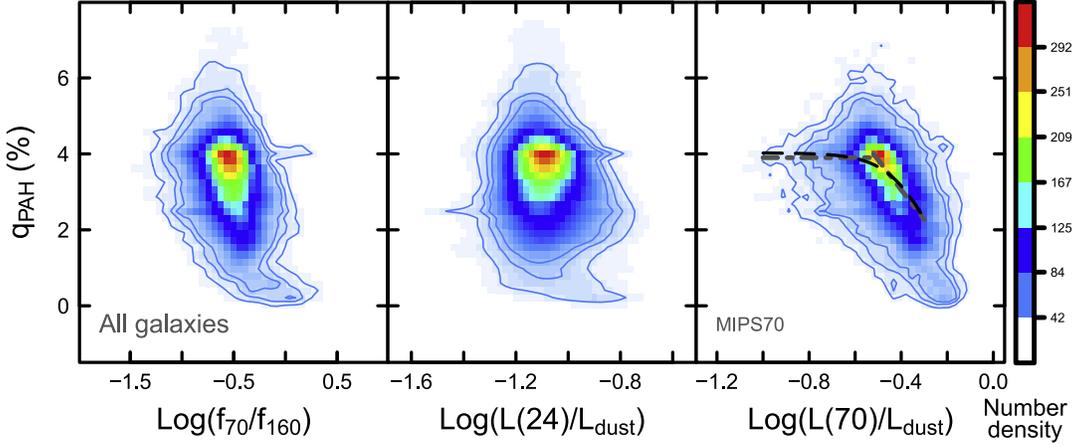

Figure 13. PAH fraction q_{PAH} versus f_{70}/f_{160} (left panel), $\nu L_{24\,\mu\mathrm{m}}/L_{\mathrm{d}}$ (middle), and $\nu L_{70\,\mu\mathrm{m}}/L_{\mathrm{d}}$ (right) for all galaxies. The 70 and 160 μm flux densities f_{70} and f_{160} are from MIPS only (see text). The color coding corresponds to number density of pixels, as shown by the rightmost color bar. The trend in the right panel for q_{PAH} to decrease with increasing $\nu L_{24\,\mu\mathrm{m}}/L_{\mathrm{d}}$ reflects the power of $\nu L_{70\,\mu\mathrm{m}}/L_{\mathrm{d}}$ to trace q_{PAH}. The (black) long-dashed line represents the best-fit function given in Equation (23) with rms residuals of $\sim$1.2% on q_{PAH}; similar residuals are given by the (gray) dashed–dotted line, a broken power-law fit as given in Equation (24).

fall significantly when $\nu L_{\nu}(70\,\mu\mathrm{m})/L_{\mathrm{dust}}$ rises to the highest levels. The lack of dependence on the $L(24)/L_{\mathrm{d}}$ ratio (and the relatively small 0.5 dex range in $L(24)/L_{\mathrm{d}}$) arises because single-photon heating generally dominates at 24 μm; big grains only get hot enough to radiate at 24 μm when the radiation field is extremely intense. Instead, at 70 μm, single-photon heating makes a significant contribution only for $U_{\min} \lesssim 0.5$. Thus, $L(70)/L_{\mathrm{d}}$ is a better indicator of warm, large grains than $L(24)/L_{\mathrm{d}}$, and it is these warm, large grains that are the signature of high-intensity radiation fields that could be associated with PAH destruction.

As seen in the right panel of Figure 13, the PAH fraction appears to vary with $L(70)/L_{\mathrm{dust}}$ according to the empirical relation

$$q_{\mathrm{PAH}} \approx \frac{0.0402}{1 + 15\,[L(70)/L_{\mathrm{dust}}]^{4.4}}, \qquad (23)$$

where the normalization constant 0.0402 corresponds to $q_{\mathrm{PAH}} \approx 4.0\%$; the rms residual of this fit is 1.2% on q_{PAH}. A similar empirical fit is given by the broken power law shown by the gray dashed–dotted line in Figure 13:

$$q_{\mathrm{PAH}} \approx \begin{cases} 0.039 & \text{if } \log_{10}\!\left(\frac{L70}{L_{\mathrm{dust}}}\right) \leqslant -0.52 \\[2mm] 0.3 - 7.0\log_{10}\!\left(\frac{L70}{L_{\mathrm{dust}}}\right) & \text{if } \log_{10}\!\left(\frac{L70}{L_{\mathrm{dust}}}\right) > -0.52. \end{cases}$$

$$(24)$$

Such a trend may reflect a tendency for PAH destruction to occur in star-forming regions, where O stars supply high-energy photons that photodestroy PAHs, and a significant fraction of the dust is exposed to starlight intensities high enough to elevate the $L(70)/L_{\mathrm{dust}}$ ratio. Many studies have previously noted suppression of PAH emission in H II regions
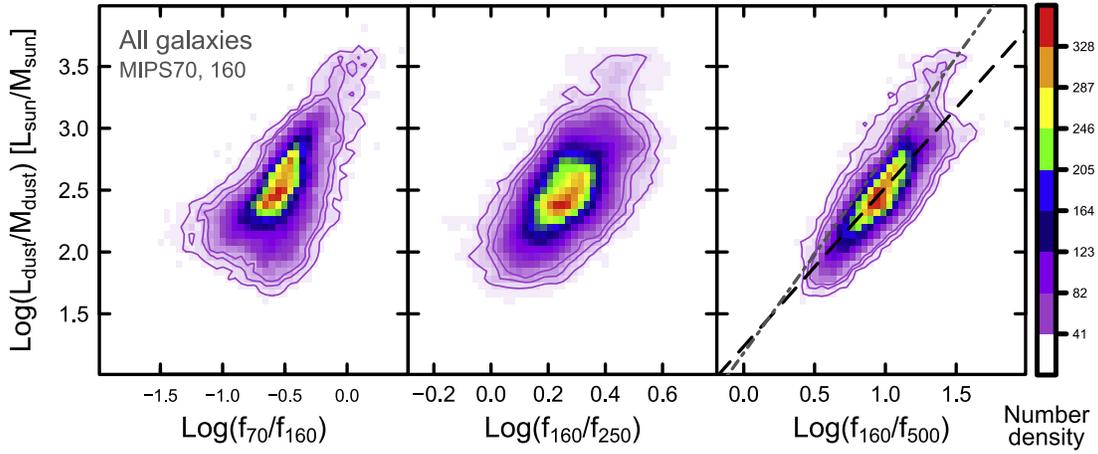
Figure 14. Dust mass-to-light ratio L_d/M_d versus f_{70}/f_{160} (left panel), f_{160}/f_{250} (middle), and f_{160}/f_{500} (right) for all galaxies. The color coding corresponds to pixel number density, as shown by the rightmost color bar. The best-fit (robust) regression for f_{160}/f_{500} is shown as a (black) long-dashed line and corresponds to rms residuals of ~ 0.18 dex (see Equation (25)). The (gray) dashed–dotted line is the analogous best-fit regression for only IC 2574 and NGC 2146 (with 383 dof; see Figure 15).

(e.g., Giard et al. 1994; Helou et al. 2004; Povich et al. 2007; Relaño et al. 2016). In a detailed study of PAH abundances in the Magellanic Clouds, Chastenet et al. (2019) show that q_{PAH} is reduced in regions close to sources of H-ionizing radiation.

High values of $L(70)/L_d$ also occur in low-metallicity galaxies, because of radiative transfer effects (hotter stars, less dust attenuation), and is consistent with the tendency for lower q_{PAH} in a metal-poor ISM.

6.7.1. Resolved Dust Light-to-mass Ratios

The dust light-to-mass ratio in galaxies and within galaxies, L_d/M_d, should reflect the peak and spread of luminosity-weighted dust temperatures. In the DL07 model, $\overline{U} \propto L_d/M_d$, so $\overline{U}$ also probes dust temperatures. We would thus expect L_d/M_d to depend on photometric flux ratios, as long as the two wavelengths in the flux ratios are sampling a sufficiently broad spectral range to be sensitive to large-grain temperature variations. Figure 14 illustrates the correlations in the resolved pixels of all galaxies between Σ_{Ld}/Σ_{Md} (noted as L_d/M_d in the ordinate axis label) and, as in Figure 12, three flux density ratios, f_{70}/f_{160}, f_{160}/f_{250}, and f_{160}/f_{500}. The longer the wavelength ratio (in this case 160 μm/500 μm), the better that Σ_{Ld}/Σ_{Md} can be predicted from observations. The right panel (black long-dashed line) of Figure 14 shows the correlation with f_{160}/f_{500} given by

$$\log_{10}\left(\frac{L_d/M_d}{L_\odot/M_\odot}\right) = (1.24 \pm 0.01)$$
$$+ (1.28 \pm 0.01)\log_{10}\left(\frac{f_{160}}{f_{500}}\right). \quad (25)$$

This fit with f_{160}/f_{500} has an rms deviation of 0.16 dex over >22,000 degrees of freedom (dof). The trend of L_d/M_d with f_{160}/f_{250} is much less reliable, so we have not shown any regression in the middle panel of Figure 14. Because of the limited wavelength lever arm for the f_{160}/f_{250} flux ratio (see also Figure 12), for a given f_{160}/f_{250} ratio, L_d/M_d can vary by a factor of 30 or more; this makes it difficult to accurately determine the dust light-to-mass ratio from f_{160}/f_{250}. Nevertheless, if we know the dust luminosity L_d and have a measure of a flux around the

peak of dust emission (e.g., f_{160}) and one sufficiently far away and in the Rayleigh–Jeans regime (e.g., f_{500}), we can estimate the dust mass M_d to within $\sim 50\%$.

Figure 15 shows the same quantities but separately for three galaxies representative of the extremes probed by the KING-FISH sample: IC 2574, a metal-poor dwarf; NGC 5457 (M101), a face-on grand-design spiral; and NGC 2146, a luminous IR galaxy (LIRG). For a flux density ratio with short +long wavelengths (e.g., f_{70}/f_{160}), the L_d/M_d ratio within these galaxies can differ by up to an order of magnitude. As has been seen in previous figures, because f_{70}/f_{160} is sensitive to both single-photon heating and the possible exposure of a small fraction of the dust to starlight intensities $U > U_{min}$, the f_{70}/f_{160} ratio does not strongly constrain the temperature of the dust grains that dominate the total emission. Instead, the longer wavelength ratio (e.g., f_{160}/f_{500}) is a much better indicator of large-grain temperature, and consequently better correlated with the dust light-to-mass ratio L_d/M_d. Two regressions are shown in Figures 14 and 15; the (black) long-dashed line, described above (see Equation (25)), is for the entire sample. The (gray) dashed–dotted one is the regression obtained for only IC 2574 and NGC 2146 and is given by

$$\log_{10}\left(\frac{L_d/M_d}{L_\odot/M_\odot}\right) = (1.18 \pm 0.05)$$
$$+ (1.59 \pm 0.04)\log_{10}\left(\frac{f_{160}}{f_{500}}\right). \quad (26)$$

The regression for the entire sample is entirely consistent with NGC 5457 (M101), but not for IC 2574 and NGC 2146, which may be considered two "extreme" galaxies. The overall radiation fields $\overline{U}$ in IC 2574 and NGC 2146 are higher (in the mean, by $\sim 40\%$ and a factor of 13, respectively) than that of NGC 5457. These more intense heating fields, possibly a signature of starbursts, result in a slightly steeper slope relating L_d/M_d and f_{160}/f_{500} than in more quiescent environments such as the disk of NGC 5457 (and most of the KINGFISH sample).

In the present model, the dust temperatures are determined by the starlight intensity distribution within a pixel, which is
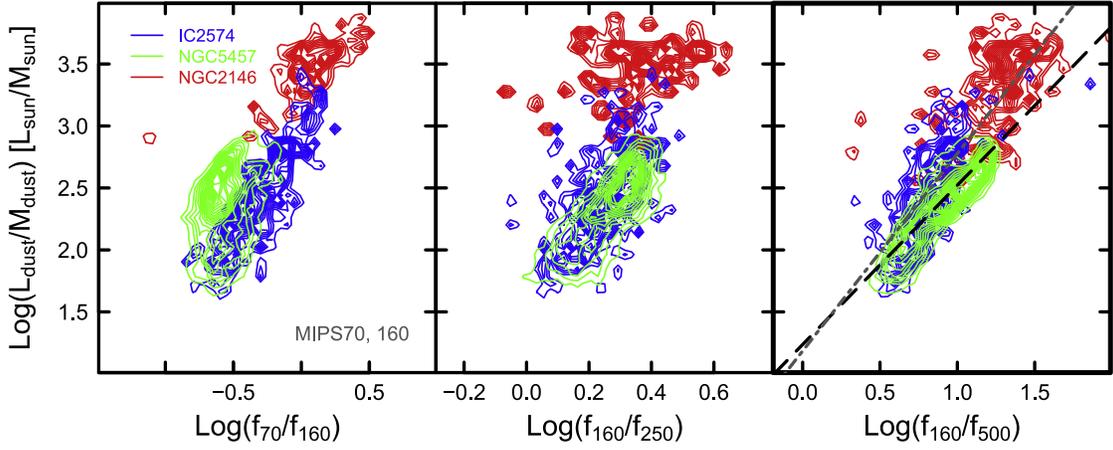
Figure 15. Dust mass-to-light ratio L_d/M_d plotted against f_{70}/f_{160} (left panel) f_{160}/f_{250} (middle), and f_{160}/f_{500} (right) for three galaxies separately: IC 2547, a low-metallicity dwarf; NGC 5457 (M101), a large grand-design spiral; and NGC 2146, an LIRG. The contours reflect the individual galaxies (IC 2547 blue, NGC 5457 green, and NGC 2146 red) and correspond to pixel number densities. In the right panel, the (black) long-dashed line corresponds to the best-fit regression reported in Figure 14 for the sample as a whole (see Equation (25)), and the (gray) dashed–dotted line corresponds to the analogous best-fit regression for only IC 2574 and NGC 2146 (383 dof).
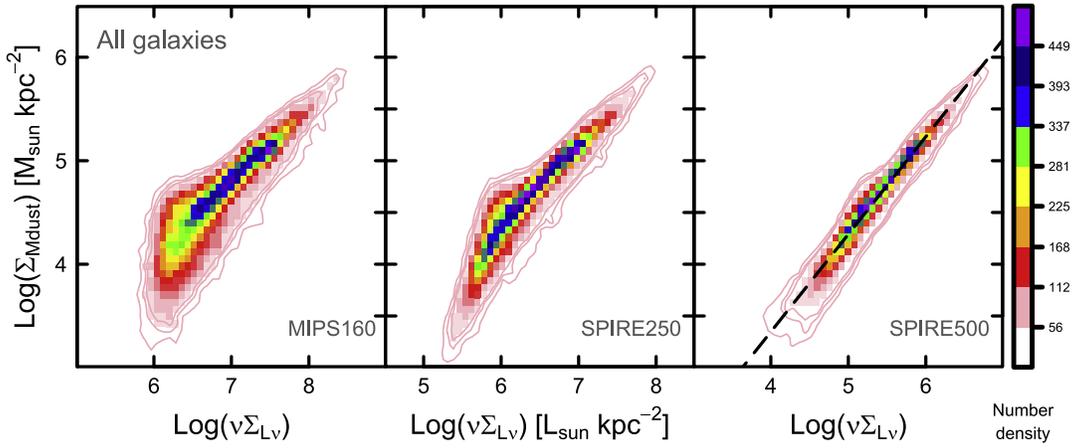

Figure 16. Dust mass surface density Σ_{Mdust} versus monochromatic surface brightness $\nu\Sigma_{L_\nu} = 4\pi\nu I_\nu$ in the MIPS 160 μm (left panel), SPIRE 250 μm (middle), and SPIRE 500 μm (right) bands, for all galaxies. The color coding corresponds to pixel number density, as shown by the rightmost color bar. The dashed line in the right panel (SPIRE500) shows the best-fit regression relating dust mass surface density Σ_{Mdust} to 500 μm luminosity surface density $\nu\Sigma_{L_\nu}(500 \ \mu\text{m})$ (Equation (27)). See Section 6.7.2 for more details.

characterized by three parameters, $U_{\min}$, γ, and α (see Section 5), and we need more than two bands if we wish to determine the distribution of temperatures for the emitting dust well enough to reliably estimate the mass of dust in the pixel. On the other hand, if flux ratios at longer wavelengths are considered (right panel of Figure 15), there is much less variation within and between galaxies. Such behavior was also seen with $U_{\min}$ in Figure 12 and suggests that ratios at these longer wavelengths better trace L_d/M_d because they provide better information about the temperatures of the large grains that dominate the dust luminosity.

6.7.2. Resolved Dust Mass Surface Densities

Given the relative constancy of dust-to-metals ratios for galaxies with metallicities $12 + \log_{10}(\text{O/H}) \gtrsim 8.4$ (see Figure 8(b)), the dust luminosity in the Rayleigh–Jeans (R-J) regime of the dust SED has become a popular tracer of ISM mass (e.g., Corbelli et al. 2012; Eales et al. 2012; Scoville et al. 2014, 2016, 2017; Groves et al. 2015). This is an effective technique both locally and at high redshift because the R-J tail of the dust emission probes optically thin dust and is relatively insensitive to dust temperature. Here we

explore whether this is also true for the spatially resolved dust emission in the KINGFISH sample. Figure 16 shows the dust mass surface density Σ_{M_d} (estimated from the renormalized DL07 model) plotted against monochromatic dust luminosity surface density $\Sigma_{\nu L_\nu} = 4\pi\nu I_\nu$ in the MIPS 160 μm, SPIRE 250 μm, and SPIRE 500 μm bands. It can be seen that at 160 μm, a wavelength that generally probes the dust emission peak, there is only a broad correlation with more than an order of magnitude dispersion at low surface brightness. As wavelength increases toward the SPIRE bands, the correlation improves and becomes very good at 500 μm, similar to the trends found for KINGFISH global values by Groves et al. (2015).

The rightmost panel reports the best-fit correlation, obtained with the robust regression algorithm:

$$\log_{10}\left(\frac{\Sigma_{M_{\text{dust}}}}{M_\odot \ \text{kpc}^{-2}}\right) = (-0.42 \pm 0.01)$$
$$+ (0.942 \pm 0.001)\log_{10}\left(\frac{\Sigma_{\nu L_\nu}(500 \ \mu\text{m})}{L_\odot \ \text{kpc}^{-2}}\right). \quad (27)$$

This fit gives an rms scatter $\sigma = 0.07$ dex on $\log_{10}(M_{\rm d})$ (with $\sim$25,400 dof), implying that dust mass surface densities can be inferred from 500 μm luminosity surface densities to within $\sim$20%. The slope is significantly sublinear, over almost three decades of 500 μm luminosity surface densities, reflecting the tendency for dust to be somewhat warmer in pixels where $\Sigma_{\rm Md}$ is high, presumably because these pixels are more likely to harbor star-forming regions. Groves et al. (2015) obtained a similar result globally for inferring gas mass from L_{500} for all KINGFISH galaxies, including dwarfs (stellar mass $\leqslant 10^9\,M_\odot$); however, once Groves et al. (2015) considered only the more massive galaxies, the slope steepened and became approximately linear.

The rms deviation of only 0.07 dex from Equation (27) implies that one can estimate $M_{\rm d}$ more reliably from $L_\nu(500\ \mu{\rm m})$ alone than from the total dust luminosity $L_{\rm d}$ and the ratio of two flux densities $L_\nu(160\ \mu{\rm m})$ and $L_\nu(500\ \mu{\rm m})$. This is because obtaining $M_{\rm d}$ from $L_{\rm d}$ using Equation (25) in effect requires estimation of $\langle T_{\rm d}^{4+\beta} \rangle$, whereas obtaining $M_{\rm d}$ from $L_\nu(500\ \mu{\rm m})$ from Equation (27) (with an rms of 0.16 dex) requires estimating only $\langle T_{\rm d} \rangle$, since at 500 μm the dust emission is in the Rayleigh–Jeans limit, with $L_\nu(500\ \mu{\rm m}) \propto M_{\rm d} \times \langle T_{\rm d} \rangle$.

To estimate ISM mass from Equation (27), the dust mass from Equation (27) needs to be combined with a gas-to-dust ratio, as discussed in Section 6.6. However, this ratio depends on metallicity (see Figure 8); thus, oxygen abundance needs to be incorporated to estimate gas mass for metal-poor galaxies. In any case, Figure 16 shows that the slope between dust mass and luminosity is steeper, closer to unity, at *lower* surface brightnesses, roughly independent of wavelength. However, global integrated values of quantities such as long-wavelength IR luminosity are luminosity weighted, thus sampling preferentially *higher* surface brightnesses. Thus, our new result for resolved regions in KINGFISH galaxies is inconsistent with a strictly linear trend of dust mass with long-wavelength IR luminosity. Indeed, as noted above, a nonlinear behavior would be expected since the dust in high $\Sigma_{\rm Md}$ pixels is, on average, somewhat warmer.

7. Summary

Dust modeling results for 70 galaxies (61 KINGFISH galaxies, plus nine additional galaxies present in the observed fields) are presented here. Dust is detected reliably in 62 galaxies, and upper limits are reported for the remaining eight. Tables 5 and 6 report the global galaxy photometry, and the best-fit dust parameter estimates are given in Table 9. Dust parameter maps are displayed in Figures 17.1–17.62. The DL07 dust model successfully reproduces the dust SEDs over the wide variety of environments present in the KINGFISH sample.

Long-wavelength imaging can be omitted in order to increase the angular resolution of the modeling, but results become unreliable if the long-wavelength coverage is insufficient. For maximum reliability, we recommend using all cameras available, including MIPS160, SPIRE250, SPIRE350, and SPIRE500. If better angular resolution is critical, the lowest-resolution cameras (SPIRE500 and MIP160) can be left out, but estimates of dust mass become unreliable unless at least SPIRE250 is included. If SPIRE350, SPIRE500, and MIPS160 are not included, the DL07 model dust masses can be low by as much as a factor of 0.8 or high by as much as a factor of 2 (see Figures 20); the median factor is 1.25. The $q_{\rm PAH}$ and

$f_{\rm PDR}$ estimates are fairly insensitive to the camera combination used, so they can be obtained reliably without $\lambda > 250\ \mu$m photometry, provided that the S/N is adequate.

Resolved (multipixel) modeling and global (single-pixel) modeling generate similar estimates of $M_{\rm d}$, $q_{\rm PAH}$, and $f_{\rm PDR}$ when all the *Spitzer* and *Herschel* cameras are employed. The single-pixel modeling tends to slightly underestimate the total dust mass $M_{\rm d}$ by $\sim$13% (see Figure 21).

Our analysis shows that $q_{\rm PAH}$, the fraction of the dust mass contributed by PAHs, correlates much better with the PP04N2 estimate for O/H than for the PT estimate, strongly suggesting that PP04N2 is a better strong-line abundance estimator than the PT estimator. We find that $q_{\rm PAH}$ appears to increase monotonically with increasing metallicity, with $q_{\rm PAH}$ varying linearly with $\log({\rm O/H})$ for $12 + \log_{10}({\rm O/H})_{\rm PP04N2} > 7.94$ (see Figure 7(b) and Equation (18)).

For most star-forming galaxies with metallicity $Z \gtrsim Z_\odot$, the dust/gas ratio is close to the limiting value where nearly all of the refractory elements are locked up in grains. However, at lower metallicity, the dust/gas ratio is often well below this limiting value, consistent with what is expected from a simple toy model with accretion rate $\tau_a^{-1} \propto Z_d$ (see Figure 8(b)).

The resolved regions in the KINGFISH galaxy sample show several trends with $U_{\rm min}$, $q_{\rm PAH}$, and mass-to-light ratios for dust emission. The characteristic starlight intensity $U_{\rm min}$ can be estimated from long-wavelength flux ratios (e.g., f_{160}/f_{500}) to within a factor of two over more than two orders of magnitude in $U_{\rm min}$ (see Equation (22)). From the same flux ratio, and with a measurement of dust luminosity, dust mass can be estimated to within $\sim$50% (see Equation (25)). Despite a variation of $\gtrsim$3 orders of magnitude in IR surface brightness, for the adopted physical dust model it is possible to estimate dust mass from IR luminosity at 500 μm to within $\sim$0.07 dex), affording an accuracy of $\sim$20% (see Equation (27)). There are of course systematic errors coming from the choice of dust model, but these are difficult to estimate. Estimating gas mass for metal-poor galaxies requires incorporating metallicity, because of the metallicity dependence of DGRs. Our formulations for inferring starlight heating intensity and dust mass from flux ratios and integrated IR or monochromatic luminosities have been calibrated over $\gtrsim$22,000 independent regions in 62 galaxies, spanning metal-poor dwarf irregulars to grand-design spiral disks and actively star-forming LIRGs. These calibrated prescriptions are designed with the aim of facilitating comparison with high-redshift galaxies, where frequently rest-frame f_{160} and at least one longer wavelength flux are available.

Figure 17. Hol2: Model results at M160 PSF (rows 1 and 2) and at S250 PSF (rows 3 and 4). Dust luminosity per area Σ_{Ld} (column 1, rows 1 and 3) is shown for the entire field, with the adopted galaxy mask boundary in white. Dust mass per area Σ_{Md} (column 2, rows 1 and 3) is after renormalization (see text). $U_{min,DL07}$, q_{PAH}, and f_{PDR} are shown in rows 2 and 4. The global SED (column 3, rows 1 and 3) is shown for single-pixel modeling, with contributions from dust heated by U_{min} (green) and dust heated by $U > U_{min}$ (red) and starlight (cyan); values of U_{min} and M_d in the figure label are for the DL07 model before renormalization. *Herschel* (blue rectangles) and *Spitzer* (red rectangles) photometry is shown; the vertical extent is $\pm 1\sigma$. Diamonds show the band-convolved flux for the model.

(The complete figure set (62 images) is available.)

HIPE v11.1.0 (Ott 2010); Scanamorphos v24.0 (Roussel 2013); R (R Core Team 2014); SM.

Appendix A
Resolved Dust Parameter Maps for KINGFISH Galaxies

As described in the text, each galaxy where we have a positive dust detection has two figures: the first (a) shows the model done at MIPS160 resolution, using data from all cameras (IRAC, MIPS, PACS, and SPIRE). This is our "gold standard" modeling. The second (b) shows a model at SPIRE250 resolution, using IRAC, MIPS24, PACS, and SPIRE250 cameras (i.e., omitting MIPS70, MIPS160, SPIRE350, and SPIRE500). This latter modeling, while able to resolve smaller scale structures in the galaxies, is overall less reliable.

Each figure in the Figure 17 figure set has 12 panels. For each of the resolutions, the top row is a map of dust luminosity surface density Σ_{L_d} (left), dust surface density Σ_{M_d} (center), and the model SED (right). The lower row shows the starlight intensity parameter $U_{\mathrm{min,DL07}}$ (left), the PAH abundance parameter q_{PAH} (center), and the PDR fraction f_{PDR} (left). The dust luminosity surface density Σ_{L_d} is shown for the full field, with the white contour showing the minimum surface brightness $\Sigma_{Ld,min}$ below which we do not attempt to model the emission. Maps of derived quantities (Σ_{M_d}, U_{min}, q_{PAH}, and f_{PDR}) are limited to the "galaxy mask" region with $\Sigma_{L_d} > \Sigma_{Ld,min}$. In the SED plot, the observed photometry is represented by rectangular boxes (*Spitzer* IRAC and MIPS in red; *Herschel* PACS and SPIRE in blue) showing $\pm 1\sigma$ uncertainties. The black line is a single-pixel DL07 model that seeks to reproduce the observed SED, with different components shown. The values of U_{min} and M_d in the label are for the DL07 model before renormalization. The cyan line is the stellar contribution, the dark red line is the emission from dust heated by the power-law U distribution, and the dark green line is emission from dust heated by $U = U_{\mathrm{min}}$.

Appendix B
Cases with 3σ Upper Limits for Dust Mass

Eight galaxies in the KINGFISH sample, five dwarfs (DDO 053, DDO 154, DDO 165, Hol1, and M81dwB) and three ellipticals (NGC 0584, NGC 0855, and NGC 1404), yield upper limits on the dust mass from our modeling. In these cases, the signal from the galaxy in the far-IR is of comparable magnitude to the contamination from background galaxies, leading to uncertain dust mass measurements.

For the three elliptical galaxies, we employ a Σ_{Ld}-based mask that roughly coincides with the optical galaxy. To obtain

Table 11
Dust Upper Limits

Galaxy	$M_d (M_\odot)$	Method
DDO 053	$<2.1 \times 10^5$	H I mask
DDO 154	$<6.1 \times 10^5$	H I mask
DDO 165	$<5.2 \times 10^5$	H I mask
Hol1	$<6.7 \times 10^5$	H I mask
M81dwB	$<8.1 \times 10^4$	H I mask
NGC 0584	$<1.6 \times 10^6$	Σ_{Ld} mask
NGC 0855	$<1.0 \times 10^6$	Σ_{Ld} mask
NGC 1404	$<2.0 \times 10^6$	Σ_{Ld} mask

an upper limit on the dust mass in the case of these nondetections, we randomly shift the mask around in the M160-resolution dust mass image, avoiding overlap with the original mask, and remeasure the total dust mass. We construct a distribution of these "background" dust mass measurements to obtain a mean and standard deviation. In all galaxies mentioned above, the mean of the "background" dust mass values is positive, as would be expected due to the real signal at far-IR wavelengths from unidentified background sources ("confusion noise"). The measured dust mass at the expected galaxy location is within $\sim 1\sigma$ of the mean. In the text and Table 11, we provide the 3σ upper limit on the dust mass generated with this procedure.

The definition of the galaxy mask itself is also potentially affected by confusion noise. In the case of the dwarf galaxies, we use the H I observations from THINGS and LittleTHINGS to create an alternative galaxy mask, based on a cut at an H I column density of 10^{20} cm^{-2} from the H I image convolved to M160 resolution. The H I-based galaxy mask is typically somewhat larger than that defined by the dust luminosity surface density cut. We apply the same procedure described above to obtain the background mean and standard deviation.

Table 11 and Figure 18 provide the results of this procedure. Table 11 lists the 3σ upper limits for each galaxy using the H I-based masks for the dwarfs and the dust luminosity surface density masks (as described in the text) for the ellipticals. Histograms of the dust masses from the randomly shifted masks are shown in Figures 18.1–18.8. We note that the dust mass limits from this procedure are expected to be very conservative. Higher S/N could be obtained by a careful treatment of the integrated photometry for each galaxy, taking the confusion noise into account.

Figure 18. DDO 053: Left: Σ_{Ld} map; contours: $\Sigma_{Ld,min} = 0.6\,L_\odot\,pc^{-2}$. Center: Σ_{Md} map within the galaxy mask. Right: histogram of M_d for H I-based mask, shifted randomly. Red dotted–dashed line: M_d for mask centered on galaxy. 68% of random masks give M_d between green dashed lines.

(The complete figure set (8 images) is available.)

Appendix C
Online KINGFISH Data and Dust Models

The processed KINGFISH imaging and dust models are available online at https://doi.org/10.34770/kyb8-bw61 (Aniano et al. 2019).

Here we briefly describe the types of data that are available there.

For each of the 70 galaxies (61 KINGFISH galaxies + nine "extras"), we provide results for resolved modeling at four different resolutions: M160, S500, S350, and S250. For each case, we use all compatible cameras (see Table 4). FITS files of the following maps are provided:

1. Dust mass surface density Σ_{Md} (renormalized).
2. Dust luminosity per unit projected area Σ_{Ld}.
3. PAH mass fraction q_{PAH}.
4. $U_{min,DL07}$ = minimum starlight intensity parameter for the DL07 model. The renormalized U_{min} can be obtained from $U_{min,DL07}$ using Equation (16).
5. $\bar{U}_{DL07}$ = mean starlight intensity parameter for the DL07 model. The renormalized $\bar{U}$ can be obtained from $\bar{U}_{DL07}$ using Equation (15).
6. f_{PDR} = fraction of the total starlight heating of dust taking place in subregions where $U > 10^2$.
7. Global SED for the dust model.

For each case, the data in the FITS files are limited to the "galaxy mask" defined by $\Sigma_{Ld} > \Sigma_{Ld,min}$, where $\Sigma_{Ld,min}$ for each galaxy is given in Table 2.

Appendix D
Dependence of Model Results on PSF Used and Wavelength Coverage

Obviously, one would like to model the dust emission with the best angular resolution that is feasible. Some of the cameras (e.g., PACS160) have small PSFs, which would seem to allow observations and modeling with high angular resolution. However, deciding to use a small PSF means not being able to use data from cameras with larger PSFs, which both reduces the amount of redundant data (e.g., MIPS70 and MIPS160) and limits the wavelength coverage by preventing use of the longer

wavelength cameras (e.g., SPIRE500). In addition, use of a smaller PSF implies a lower S/N, which is a limiting factor in regions with low surface brightness.

Here we examine the degree to which derived dust and starlight parameters are sensitive to the choice of PSF. We also compare the results obtained from the resolved modeling and those from global photometry.

D.1. Comparison of Modeling at S250 Resolution with the Gold Standard (M160)

Figure 19 shows the comparison of the dust parameter estimates obtained from models using the S250 PSF (18.2″ FWHM) with parameters estimated from (our "gold standard") modeling using all cameras (IRAC, MIPS, PACS, SPIRE) and the M160 PSF (39″ FWHM).

The results for L_d and M_d at S250 resolution appear to be quite robust: the median change in L_d is only 5%, which may be due in part to calibration differences between MIPS160 and PACS160, with MIPS160 data being used only in the M160 PSF modeling. Note that M_d shows more variation, with a median change of 25%; this is likely because loss of SPIRE350 and SPIRE500 may allow modeling at the S250 PSF to include a bit more cool dust than is actually present. However, it is gratifying that the median change is only 25%, indicating that the DL07 model is relatively good at "predicting" $\lambda > 300\,\mu$m emission using data shortward of 300 μm. However, in some cases, the dust mass is overestimated by as much as a factor of 2 (see Figure 20), and we therefore recommend using M160-resolution modeling rather than the riskier S250 PSF.

D.2. Dust Mass Estimates at Different Resolutions

Figure 20 shows the comparison of the dust mass estimates for four different resolutions and camera combinations. The compared resolutions are as follows:

1. M160 (the "gold standard") uses all the cameras (IRAC, MIPS, PACS, SPIRE) at the MIPS160 PSF; this is taken to be our best estimate for M_d.
2. S500: IRAC, MIPS24, MIPS70, PACS, and SPIRE at the SPIRE500 PSF.

Figure 19. Comparison of modeling with the S250 PSF to results obtained with the M160 PSF (the "gold standard"). With S250 modeling, the dust mass tends to be slightly overestimated; the median overestimation is ~25%.

3. S350: IRAC, MIPS24, MIPS70, PACS, SPIRE250, and SPIRE350 at the SPIRE350 PSF.
4. S250: IRAC, MIPS24, PACS, and SPIRE250 at the SPIRE250 PSF.
5. P160: IRAC, MIPS24, and PACS at the PACS160 PSF. This is the riskiest PSF we are willing to consider.

For each resolution, Figure 20 shows a histogram of the galactic total dust mass estimates divided by the gold standard estimate.

We observe that dust mass discrepancies can be large, with the errors and bias increasing as fewer cameras are used, and long-wavelength data are lost. The S500 case (coverage out to 500 μm, a PSF that is not much smaller than the M160 PSF, but no MIPS160 photometry) gives dust mass estimates that are

close to our gold standard estimate, with a median ratio of 1.21. However, there are a few outliers where M_d appears to be overestimated by as much as a factor of 2. These are all galaxies with very weak dust emission and low-S/N data, where loss of the data from one camera (MIPS160) causes a significant change in the apparent SED.

The systematic bias in M_d and the scatter both increase as we move to smaller PSFs (S350, S250, P160). At P160 resolution, fully 25% of the cases have M_d *under* estimated by a factor of 2 or more.

On balance, it appears that modeling at S250 resolution is reasonable, although slightly risky: there is a significant chance that the dust mass may be overestimated or underestimated by a factor of 1.5 or more. S350 resolution is safer, and S500 even better.

Figure 20. Comparison of estimates for dust mass M_d obtained from multipixel modeling with different PSFs and camera combinations. The "gold standard" refers to modeling with the M160 PSF and all cameras. Here we compare M_d obtained with the S500, S350, S250, and P160 PSFs (see Table 4). Because of the limited wavelength coverage and lower S/N, for the P160 PSF the dust mass can be in error by up to a large factor: 10/62 cases underestimate the dust mass by more than a factor of 2, and 2/62 cases by more than a factor of 5.

D.3. Modeling Using Only Global Photometry (Single Pixel)

The KINGFISH galaxies are close ($D < 30$ Mpc) and large enough that they can be resolved using the *Herschel* Space Telescope. When studying galaxies at larger distances, only their global photometry may be available. Here we compare our dust mass estimates using resolved imaging and multipixel modeling with "single-pixel" modeling that makes use of only the global SED. We recall that the dust modeling is not a linear process, and differences in parameter estimates are to be expected.

Figure 21 shows the ratio of the dust model parameter estimates from fitting global photometry (a "single pixel" model) versus our "gold standard" multipixel modeling at M160 resolution, where each pixel is modeled separately. In

both cases we use all cameras: IRAC, MIPS, PACS, and SPIRE. We observe that L_d is very reproducible, with the single-pixel luminosity estimate differing from the multipixel result by only a few percent.

The dust mass estimate is probably most important, and is found to be moderately robust: for 75% of the cases, the single-pixel modeling obtains a mass estimate within 25% of the resolved multipixel analysis. Thus, dust mass estimates for unresolved distant galaxies should be reliable, assuming only that the photometry covers a suitable range of wavelengths (rest-frame wavelengths $50 \lesssim \lambda \lesssim 300\ \mu$m), with an adequate S/N.

The $\langle f_{\mathrm{PDR}} \rangle$ and $\langle q_{\mathrm{PAH}} \rangle$ estimates are both quite robust, with the single-pixel results agreeing with the multipixel analysis to within $\sim$5% in most cases.

Figure 21. Dust mass estimation using global (single-pixel) modeling versus sum over resolved (multipixel) modeling at M160 resolution. Single-pixel modeling estimates the total dust mass to within a factor of 2 in the worst case (Holmberg II), but for ~70% of the cases the single-pixel mass is within 25% of the multipixel mass.

ORCID iDs

G. Aniano ⓞ https://orcid.org/0000-0001-9015-2654
B. T. Draine ⓞ https://orcid.org/0000-0002-0846-936X
L. K. Hunt ⓞ https://orcid.org/0000-0001-9162-2371
K. Sandstrom ⓞ https://orcid.org/0000-0002-4378-8534
D. Calzetti ⓞ https://orcid.org/0000-0002-5189-8004
R. C. Kennicutt ⓞ https://orcid.org/0000-0001-5448-1821
D. A. Dale ⓞ https://orcid.org/0000-0002-5782-9093
M. Galametz ⓞ https://orcid.org/0000-0002-0283-8689
K. D. Gordon ⓞ https://orcid.org/0000-0001-5340-6774
A. K. Leroy ⓞ https://orcid.org/0000-0002-2545-1700
J.-D. T. Smith ⓞ https://orcid.org/0000-0003-1545-5078
H. Roussel ⓞ https://orcid.org/0000-0001-5617-7129
M. Sauvage ⓞ https://orcid.org/0000-0002-0809-2574
F. Walter ⓞ https://orcid.org/0000-0003-4793-7880
L. Armus ⓞ https://orcid.org/0000-0003-3498-2973
A. D. Bolatto ⓞ https://orcid.org/0000-0002-5480-5686
M. Boquien ⓞ https://orcid.org/0000-0003-0946-6176
A. Crocker ⓞ https://orcid.org/0000-0001-8513-4945
I. De Looze ⓞ https://orcid.org/0000-0001-9419-6355
J. Donovan Meyer ⓞ https://orcid.org/0000-0002-3106-7676
G. Helou ⓞ https://orcid.org/0000-0003-3367-3415
J. Hinz ⓞ https://orcid.org/0000-0003-3339-0546
B. D. Johnson ⓞ https://orcid.org/0000-0002-9280-7594
J. Koda ⓞ https://orcid.org/0000-0002-8762-7863
E. J. Murphy ⓞ https://orcid.org/0000-0001-7089-7325
M. Relaño ⓞ https://orcid.org/0000-0003-1682-1148
H.-W. Rix ⓞ https://orcid.org/0000-0003-4996-9069
E. Schinnerer ⓞ https://orcid.org/0000-0002-3933-7677
M. G. Wolfire ⓞ https://orcid.org/0000-0003-0030-9510

References

Alatalo, K., Blitz, L., Young, L. M., et al. 2011, ApJ, 735, 88
Alatalo, K., Lacy, M., Lanz, L., et al. 2015, ApJ, 798, 31
Andrews, B. H., & Martini, P. 2013, ApJ, 765, 140
Aniano, G., Draine, B. T., Calzetti, D., et al. 2012, ApJ, 756, 46
Aniano, G., Draine, B. T., Gordon, K. D., & Sandstrom, K. M. 2011, PASP, 123, 1218
Aniano, G., Draine, B. T., Hunt, L. K., et al. 2019, Dust and Starlight Maps for Galaxies in the KINGFISH Sample (Princeton, NJ: Princeton Univ.), http://arks.princeton.edu/ark:/88435/dsp01hx11xj13h
Asano, R. S., Takeuchi, T. T., Hirashita, H., & Inoue, A. K. 2013, EP&S, 65, 213
Asplund, M., Grevesse, N., Sauval, A. J., & Scott, P. 2009, ARA&A, 47, 481
Bajaja, E., van der Burg, G., Faber, S. M., et al. 1984, A&A, 141, 309
Berg, D. A., Skillman, E. D., Croxall, K. V., et al. 2015, ApJ, 806, 16
Boselli, A., Lequeux, J., Sauvage, M., et al. 1998, A&A, 335, 53
Bot, C., Ysard, N., Paradis, D., et al. 2010, A&A, 523, A20
Calzetti, D., Wilson, G. W., Draine, B. T., et al. 2018, ApJ, 852, 106
Chastenet, J., Sandstrom, K., Chiang, I.-D., et al. 2019, ApJ, 876, 62
Chiang, I. D., Sandstrom, K. M., Chastenet, J., et al. 2018, ApJ, 865, 117
Corbelli, E., Bianchi, S., Cortese, L., et al. 2012, A&A, 542, A32
Croxall, K. V., Pogge, R. W., Berg, D. A., Skillman, E. D., & Moustakas, J. 2016, ApJ, 830, 4
Dalcanton, J. J., Fouesneau, M., Hogg, D. W., et al. 2015, ApJ, 814, 3
Dale, D. A., Aniano, G., Engelbracht, C. W., et al. 2012, ApJ, 745, 95
Dale, D. A., Cohen, S. A., Johnson, L. C., et al. 2009, ApJ, 703, 517
Dale, D. A., Cook, D. O., Roussel, H., et al. 2017, ApJ, 837, 90
De Cia, A., Ledoux, C., Mattsson, L., et al. 2016, A&A, 596, A97
Dellenbusch, K. E., Gallagher, J. S. I., Knezek, P. M., & Noble, A. G. 2008, AJ, 135, 326
Donovan Meyer, J., Koda, J., Momose, R., et al. 2013, ApJ, 772, 107
Draine, B. T. 1990, in ASP Conf. Ser. 12, The Evolution of the Interstellar Medium, ed. L. Blitz (San Francisco, CA: ASP), 193
Draine, B. T. 2003, ARA&A, 41, 241
Draine, B. T. 2009, in ASP Conf. Ser. 414, Cosmic Dust—Near and Far, ed. T. Henning, E. Grün, & J. Steinacker (San Francisco, CA: ASP), 453
Draine, B. T. 2011, Physics of the Interstellar and Intergalactic Medium (Princeton, NJ: Princeton Univ. Press)
Draine, B. T., Aniano, G., Krause, O., et al. 2014, ApJ, 780, 172
Draine, B. T., Dale, D. A., Bendo, G., et al. 2007, ApJ, 663, 866
Draine, B. T., & Hensley, B. 2012, ApJ, 757, 103
Draine, B. T., & Li, A. 2007, ApJ, 657, 810
Draine, B. T., & Salpeter, E. E. 1979, ApJ, 231, 77
Eales, S., Smith, M. W. L., Auld, R., et al. 2012, ApJ, 761, 168
Edmunds, M. G. 2001, MNRAS, 328, 223
Engelbracht, C. W., Gordon, K. D., Rieke, G. H., et al. 2005, ApJL, 628, L29
Engelbracht, C. W., Rieke, G. H., Gordon, K. D., et al. 2008, ApJ, 678, 804
Esteban, C., Bresolin, F., Peimbert, M., García-Rojas, J., Peimbert, A., & Mesa-Delgado, A. 2009, ApJ, 700, 654
Fazio, G. G., Hora, J. L., Allen, L. E., et al. 2004, ApJS, 154, 10
Galametz, M., Kennicutt, R. C., Albrecht, M., et al. 2012, MNRAS, 425, 763
Galliano, F., Hony, S., Bernard, J. P., et al. 2011, A&A, 536, A88
Giard, M., Bernard, J. P., Lacombe, F., Normand, P., & Rouan, D. 1994, A&A, 291, 239
Gordon, K. D., Meixner, M., Meade, M. R., et al. 2011, AJ, 142, 102
Griffin, M. J., Abergel, A., Abreu, A., et al. 2010, A&A, 518, L3
Groves, B. A., Schinnerer, E., Leroy, A., et al. 2015, ApJ, 799, 96
Helou, G., Roussel, H., Appleton, P., et al. 2004, ApJS, 154, 253
Hota, A., & Saikia, D. J. 2005, MNRAS, 356, 998
Hunt, L., Bianchi, S., & Maiolino, R. 2005, A&A, 434, 849
Hunt, L., Dayal, P., Magrini, L., & Ferrara, A. 2016, MNRAS, 463, 2002
Hunt, L. K., Draine, B. T., Bianchi, S., et al. 2015, A&A, 576, A33
Hunt, L. K., Thuan, T. X., Izotov, Y. I., & Sauvage, M. 2010, ApJ, 712, 164
Hunter, D. A., Ficut-Vicas, D., Ashley, T., et al. 2012, AJ, 144, 134
Israel, F. P., Wall, W. F., Raban, D., et al. 2010, A&A, 519, A67
Kennicutt, R. C., Armus, L., Bendo, G., et al. 2003, PASP, 115, 928
Kennicutt, R. C., Calzetti, D., Aniano, G., et al. 2011, PASP, 123, 1347
Kewley, L. J., & Ellison, S. L. 2008, ApJ, 681, 1183
Kobulnicky, H. A., & Kewley, L. J. 2004, ApJ, 617, 240
Leroy, A. K., Walter, F., Bigiel, F., et al. 2009, AJ, 137, 4670
Leroy, A. K., Walter, F., Sandstrom, K., et al. 2013, AJ, 146, 19
Li, Y., Bresolin, F., & Kennicutt, R. C., Jr. 2013, ApJ, 766, 17
Li, Z., Jones, C., Forman, W. R., et al. 2011, ApJ, 730, 84
Madden, S. C. 2000, NewAR, 44, 249
Makarov, D., Prugniel, P., Terekhova, N., Courtois, H., & Vauglin, I. 2014, A&A, 570, A13
Marble, A. R., Engelbracht, C. W., van Zee, L., et al. 2010, ApJ, 715, 506
Martinez-Badenes, V., Lisenfeld, U., Espada, D., et al. 2012, A&A, 540, A96
Mathis, J. S., Mezger, P. G., & Panagia, N. 1983, A&A, 128, 212

Mattsson, L., Andersen, A. C., & Munkhammar, J. D. 2012, MNRAS, 423, 26

McMullin, J. P., Waters, B., Schiebel, D., Young, W., & Golap, K. 2007, in ASP Conf. Ser. 376, CASA Architecture and Applications, ed. R. A. Shaw, F. Hill, & D. J. Bell (San Francisco, CA: ASP), 127

Moustakas, J., Kennicutt, R. C., Tremonti, C. A., et al. 2010, ApJS, 190, 233

Muñoz-Mateos, J. C., Gil de Paz, A., Boissier, S., et al. 2009, ApJ, 701, 1965

Ott, S. 2010, in ASP Conf. Ser. 434, Astronomical Data Analysis Software and Systems XIX, ed. Y. Mizumoto, K.-I. Morita, & M. Ohishi (San Francisco, CA: ASP), 139

Pellegrini, E. W., Smith (PI, J. D., Wolfire, M. G., et al. 2013, ApJL, 779, L19

Pettini, M., & Pagel, B. E. J. 2004, MNRAS, 348, L59

Pilbratt, G. L., Riedinger, J. R., Passvogel, T., et al. 2010, A&A, 518, L1

Pilyugin, L. S., Grebel, E. K., & Kniazev, A. Y. 2014, AJ, 147, 131

Pilyugin, L. S., & Thuan, T. X. 2005, ApJ, 631, 231

Pilyugin, L. S., Thuan, T. X., & Vílchez, J. M. 2006, MNRAS, 367, 1139

Pilyugin, L. S., Thuan, T. X., & Vílchez, J. M. 2007, MNRAS, 376, 353

Planck Collaboration, Ade, P. A. R., Aghanim, N., et al. 2011, A&A, 536, A17

Planck Collaboration, Ade, P. A. R., Aghanim, N., et al. 2016, A&A, 586, A132

Poglitsch, A., Waelkens, C., Geis, N., et al. 2010, A&A, 518, L2

Povich, M. S., Stone, J. M., Churchwell, E., et al. 2007, ApJ, 660, 346

R Core Team 2014, R: A Language and Environment for Statistical Computing, R Foundation for Statistical Computing, Vienna, Austria

Relaño, M., Kennicutt, R., Lisenfeld, U., et al. 2016, A&A, 595, A43

Rémy-Ruyer, A., Madden, S. C., Galliano, F., et al. 2013, A&A, 557, A95

Rémy-Ruyer, A., Madden, S. C., Galliano, F., et al. 2014, A&A, 563, A31

Rieke, G. H., Young, E. T., Engelbracht, C. W., et al. 2004, ApJS, 154, 25

Roche, P. F., Aitken, D. K., Smith, C. H., & Ward, M. J. 1991, MNRAS, 248, 606

Roussel, H. 2013, PASP, 125, 1126

Roussel, H., Helou, G., Smith, J. D., et al. 2006, ApJ, 646, 841

Sandstrom, K. M., Leroy, A. K., Walter, F., et al. 2013, ApJ, 777, 5

Scoville, N., Aussel, H., Sheth, K., et al. 2014, ApJ, 783, 84

Scoville, N., Lee, N., Vanden Bout, P., et al. 2017, ApJ, 837, 150

Scoville, N., Sheth, K., Aussel, H., et al. 2016, ApJ, 820, 83

Skibba, R. A., Engelbracht, C. W., Dale, D., et al. 2011, ApJ, 738, 89

Storchi-Bergmann, T., Calzetti, D., & Kinney, A. L. 1994, ApJ, 429, 572

Strickland, D. K., Heckman, T. M., Colbert, E. J. M., Hoopes, C. G., & Weaver, K. A. 2004, ApJS, 151, 193

Sturm, E., Lutz, D., Tran, D., et al. 2000, A&A, 358, 481

Utomo, D., Chiang, I. D., Leroy, A. K., Sandstrom, K. M., & Chastenet, J. 2019, ApJ, 874, 141

Vagshette, N. D., Pandge, M. B., Pandey, S. K., & Patil, M. K. 2012, NewA, 17, 524

van Zee, L., Haynes, M. P., & Salzer, J. J. 1997, AJ, 114, 2479

Vílchez, J. M., Relaño, M., Kennicutt, R., et al. 2019, MNRAS, 483, 4968

Walter, F., Brinks, E., de Blok, W. J. G., et al. 2008, AJ, 136, 2563

Weingartner, J. C., & Draine, B. T. 1999, ApJ, 517, 292

Weingartner, J. C., & Draine, B. T. 2001a, ApJ, 548, 296

Weingartner, J. C., & Draine, B. T. 2001b, ApJ, 553, 581

Werner, M. W., Roellig, T. L., Low, F. J., et al. 2004, ApJS, 154, 1

Zhukovska, S., Dobbs, C., Jenkins, E. B., & Klessen, R. S. 2016, ApJ, 831, 147